Diss. ETH No. 17323

Intra-Body Communication for Biomedical Sensor Networks

A dissertation submitted to the

ETH ZURICH

for the degree of

Doctor of Sciences

presented by

MARC SIMON WEGMÜLLER

Dipl. El. Ing. ETH

born 20. September 1977

citizen of Switzerland

accepted on the recommendation of

Prof. Dr. Wolfgang Fichtner, examiner

Prof. Dr. Peter Niederer, co-examiner

Prof. Dr. Niels Kuster, co-examiner

2007

Acknowledgments

First of all, I would like to thank my advisor Prof. Dr. Wolfgang Fichtner for his support, for his faith in my work, and for enabling collaboration with all external project partners. I am grateful to Prof. Dr. Peter Niederer for co-examining this thesis.

I wish to express my gratitude to Prof. Dr. Niels Kuster and the Foundation for Research on Information Technologies in Society (IT'IS) for their support during the entire research project.

Very special thanks go to Prof. Dr. med. Otto Hess, Cardiology *Insel* University Hospital, Bern, who offered to conduct the clinical trial. Also from *Insel* University Hospital, I would like to thank my colleague Adrian Lehner for organization and support during the entire clinical study.

My deepest gratefulness belongs to Dr. Michael Oberle. He has accompanied me for several years as a mentor. We began the research on body communication thanks to his initial ideas. The numerous discussions with him and his advice have been an invaluable contribution to my efforts in further developing models and systems for intra-body communication.

I would like to address my special thanks to Dr. Juerg Froehlich. This work would not have been possible without his ideas and input on numerical simulation. Moreover, Juerg offered his help and support much further than only in the technical profundities of numerical models.

For numerous contributions in the field of numerical simulations I would like to thank Joanna Olszewska, former member of IT'IS, and Andreas Kuhn, Automatic Control Laboratory (IfA). The successful and close collaboration with both showed that cooperation in my interdisciplinary research field can be incredibly fruitful.

At the Integrated Systems Laboratory (IIS) I would like to thank Dr. Norbert Felber and, from the Microelectronics Design Center, Dr. Hubert Kaeslin. They both introduced me to the field of digital VLSI design and motivated me to start my PhD work by combining VLSI with complementary applications such as offered by biomedical research.

I am extremely grateful to my colleagues from IIS: I shared not only the office but many interesting and fruitful discussions with Chiara Martelli, Flavio Carbognani, and Felix Buergin during the last 3 years. The exchange inside the digital group was enriching. Many thanks to the entire MIMO group with Dr. Andy Burg, David Perels, Simon Häne, Peter Lüthi, Stefan Eberli, Markus Wenk, and Christoph Studer. The idea exchange with the members of the Bio Electromagnetics and EMC group greatly complemented my work. Special thanks to Dr. Juergen Schuderer, Sven Ebert, Stefan Benkler, Verónica Berdiñas Torres, and Peter Müller. In addition, I would like to mention Frank Gürkaynak and Matthias Braendli who have become very good friends.

Among the many students I supervised over the years, I would especially like to mention the group with Tobias Blaser, Stephan Senn, and Philipp Stadelmann plus the work of Martin Hediger and Thomas Kaufmann. The discussions and work with them have been a great pleasure and resulted in very valuable research contributions.

Hanspeter Mathys and Hansjörg Gisler supported me with their craftsmanship and with their friendliness. I wish to especially thank Dr. Dölf Aemmer and Christine Haller for their administrative efforts on my research project shared between IIS and IT'IS. Furthermore, I want to acknowledge the efforts carried out at IT'IS by Jaqueline Pieper and the proofreading by Michelle Stubbs.

In the end, my deepest thanks go to my parents Ursula and Rolf Wegmüller for all the care and support they gave me in the last years. They are the best parents I can imagine. Thanks also to my brother David who has been a friend and a good listener in many discussions through our entire lives.

Zurich, July 2007 Marc Wegmüller

Abstract

Intra-body communication is a novel data transmission method that uses the human body as an electrical channel. The idea is driven by the vision of a cable-free biomedical monitoring system. On-body and implanted sensors monitor the vital functions and transfer data through the human body to a central monitoring unit. Especially for risk patients and long-term applications, such a technology offers more freedom, comfort, and opportunities in clinical monitoring.

In this thesis, the human body is characterized as a transmission medium for electrical currents by means of the dielectric properties and the developed electrical models of human tissue. Numerical finite-element simulations are compared to *in vivo* measurements. For that purpose, a sophisticated measurement hardware has been developed that applies alternating 1 mA peak current in the promising frequency range of 10 kHz to 1 MHz.

The individual-specific variations of the transmission characteristics have been investigated in a clinical trial. The subjects' extra-cellular and intracellular water distribution and skin condition have been identified as the most significant indicators. Overall, the thorax features reasonable transmission characteristics with an averaged attenuation of 55 dB and a typical SNR of 20 dB, while the extremities and joints cause poorer transmissions.

Finally, this work proposes transmitter and receiver architectures for intra-body communication. Data transfers of up to 64 kbit/s with BPSK modulation have been achieved through the human body. The first VLSI implementation of a modified SPIHT algorithm offers compression ratios of up to 20:1 for ECG signals still containing all significant details for medical diagnosis. The implementations fulfill all biomedical requirements on galvanic coupling into and within the human body.

Zusammenfassung

Intra-body Kommunikation ist eine neuartige Datenübertragungsmethode, die den menschlichen Körper als elektrischen Kanal benutzt. Die Idee basiert auf der Vision eines kabellosen Monitoringsystems. Auf dem Körper getragene und implantierte Sensoren zeichnen die Vitalfunktionen auf und übertragen die Daten durch den Körper zu einer Zentraleinheit. Speziell für Risiko- und Langzeitpatienten offeriert die Technologie mehr Bewegungsfreiheit, Komfort und Möglichkeiten in der klinischen Überwachung.

In dieser Arbeit wird der menschliche Körper als Übertragungsmedium für elektrische Ströme anhand von den dielektrischen Eigenschaften und elektrischen Modellen des Gewebes charakterisiert. Numerische Finite-Elemente Simulationen werden mit *in vivo* Messungen verglichen. Dazu ist eine Messhardware entwickelt worden, welche alternierende Ströme von 1 mA im vielversprechenden Frequenzbereich von 10 kHz bis 1 MHz appliziert.

Die Individuum spezifischen Schwankungen sind in einer klinischen Studie untersucht worden. Die extra-celluläre und intra-celluläre Wasserverteilung und die Hautbedingungen der Versuchspersonen sind als die signifikantesten Indikatoren erkannt worden. Insgesamt weist der Thorax eine gemittelte Dämpfung von 55 dB und ein typisches SNR von 20 dB auf, während die Extremitäten und Gelenke schlechtere Übertragungen verursachen.

Schlussendlich werden in dieser Arbeit Sender- und Empfängerarchitekturen für die Intra-Body Kommunikation vorgeschlagen. Datenübertragungen bis 64 kbit/s werden mit BPSK Modulation erreicht. Die erste VLSI Implementierung des modifizierten SPIHT Algorithmus bietet 20-fache EKG Signalkomprimierung ohne Verlust von relevanten Details für die medizinsche Diagnose. Die Implementierungen erfüllen die biomedizinischen Anforderungen an galvanische Kopplung innerhalb des menschlichen Körpers.

Contents

Chapter 1

Introduction

The health care market has become a four trillion dollar industry worldwide. Predictions estimate a doubling within ten years [Plu06]. With this enormous growth comes the need for new information technologies to achieve two critical goals: cutting costs while improving the quality of care. A long list of factors, including an intensely competitive health care market, strong pressure to prevent medical errors, and the need to comply with regulations, are combining to trigger rapid growth in technology spending.

Interest in mobile monitoring technologies and electronic medical records is exploding as hospitals and clinics of all sizes strive to provide physicians and caregivers with advanced access to clinical information. Diagnosis, surveillance, and treatment are increasingly dependent on monitoring information. Sensors, such as shown in Fig. 1.1, transmit data to monitoring devices of the hospital IT infrastructure. Electrocardiogram (ECG), electroencephalography (EEG), body temperature, pulse oximetry (SpO_2), and blood pressure are emerging as long-term monitoring sensors for emergency and risk patients. Advanced sensors for chemical, physical, and even visual applications will become part of future monitoring platforms to check, for example, insulin or hemoglobin.

So far, most existing sensors are connected by wire to the medical monitors. The trend of future monitoring platforms is to replace the data cables between sensors and monitors by wireless links. Wireless technologies will provide much more freedom and mobility to the patients. The benefit to the

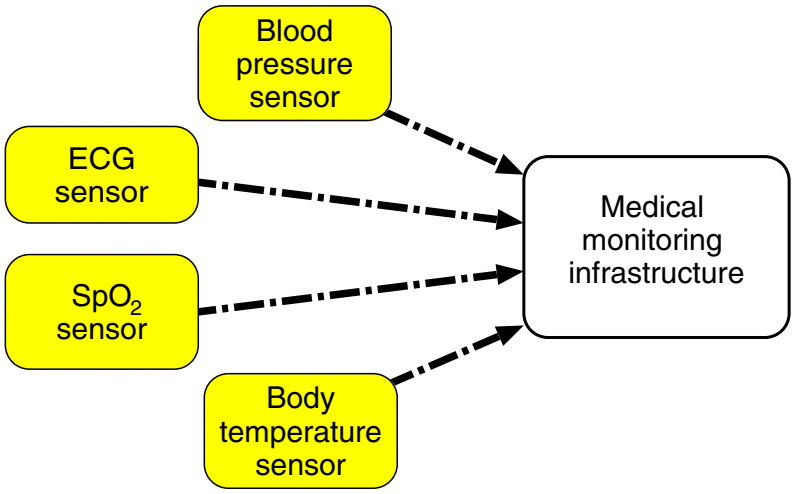

Figure 1.1: Sensor network of biomedical monitoring applications: Sensors transmit their recorded data wired or wireless to monitoring devices of the medical infrastructure.

patient's comfort is obvious, especially for long-term monitoring. In addition, complex monitoring during surgery and medical examination can be intensified, and information can be obtained during the patient's activities and movements.

Table 1.1 shows the data rate depending on the appropriate sampling rate of target biomedical sensor applications. A single sensor for the monitoring

Table 1.1: Biomedical sensor applications for monitoring of vital functions [PSAM05].

Parameter	Sampling Frequency [Hz]	Data rate with 12-bit
Blood pressure	60	1.44 kbit/s
ECG 1-point	250	6 kbit/s
ECG 12-point	250	72 kbit/s
EEG 1-channel	200	4.8 kbit/s
EEG 192-channel	200	921.6 kbit/s
Body temperature	0.1	2.4 bit/s
Pulse oximetry (SpO_2)	300	7.2 kbit/s

of biological signals generates a small data stream of a few kbit/s. The sampling frequencies of biomedical sensors are typical below 300 Hz due to the fact that biological signals oscillate at frequencies of a few Hz, e.g., heart beat, breathing. It takes a large array of sensors, e.g., EEG 192-channel recording, to increase the data rate up to hundreds of kbit/s.

Specific challenges in a wireless sensor network for patient monitoring are:

- The presence of the sensors shall not impede the patient.
- The signal transmission shall not interfere with human body functions. Existing regulations must be strictly met.
- Real-time requirements have to be met to handle emergency situations.
- Every sensor shall function over a long period with a small battery.
- A large number of sensor nodes must be handled without mutual influence.
- A sensor shall be placed on-body (band-aid), subcutaneous, or implanted (pill).

Standard wireless technologies, well-known from wireless communication by portable computers, personal digital assistants (PDAs), and multimedia capable phones have been investigated for medical sensor networks. A link data rate of 64 kbit/s and low-power operation are desired. Low carrier frequency and low transmission power limit the local effects in human tissue, e.g., heating and tissue irritation. Table 1.2 compares WLAN, Bluetooth, Zig-bee, and active RFID. WLAN and Bluetooth offer data rates above the required data rates listed in Tab. 1.1, whereas Zig-bee and active RFID feature low transmission power.

For the interconnection of sensors with a network topology as depicted in Fig. 1.1, standard wireless technologies are conditionally suited. WLAN and Bluetooth modules emit excessive transmission power and dissipate an overly high power level for battery-powered sensors. Zig-bee and active RFID offer insufficient data rates. Only active RFIDs target high miniaturization and an extremely low carrier frequency suitable for biomedical applications.

Table 1.2: Characteristic data of wireless technologies: WLAN, Bluetooth, Zig-bee, RFID, and desired technology for body sensor networks.

Technology	Frequency	Data rate	Transmission power	Size
WLAN	2.4/5.1 GHz	54 Mbit/s	100 mW	PC card
Bluetooth	2.4 GHz	723.1 kbit/s	10 mW	PCB module
Zig-bee	868 MHz	20 kbit/s	1 mW	PCB module
Active RFID	134 kHz	128 bit/s	< 1 mW	pill
Intra-Body COM (desired)	<1 MHz	>64 kbit/s	< 1 mW	band-aid / pill

Therefore, a novel transmission technique is sought which focuses on transmission power below 1 mW, data rates of 64 kbit/s, and the possibility for miniaturization to integrate the transceiver modules into band-aids and implantable pills.

1.1 Intra-Body Communication Technology

Intra-Body Communication is a novel signal transmission using the human body as the transmission medium for electrical signals [Zim95].

Figure 1.2 shows the modified network organization for interconnecting the biomedical sensors. The data is not transfered directly from the biomedical sensors to the hospital infrastructure as in Fig. 1.1; the sensors send their data via a suitable low-power and low-rate intra-body communication link to the central link sensor (located on the body like all other sensors). Any of the sensors may act as a relay sensor between a sensor and the central link sensor if a direct connection is limited.

An external wireless link enables the data exchange between the central link sensor and the external hospital infrastructure. That link may consist of a standard wireless technology, e.g., WLAN, with a high data rate. For this link, the power consumption is not an issue due to the fact that a relatively large power source can be provided for the dedicated central module.

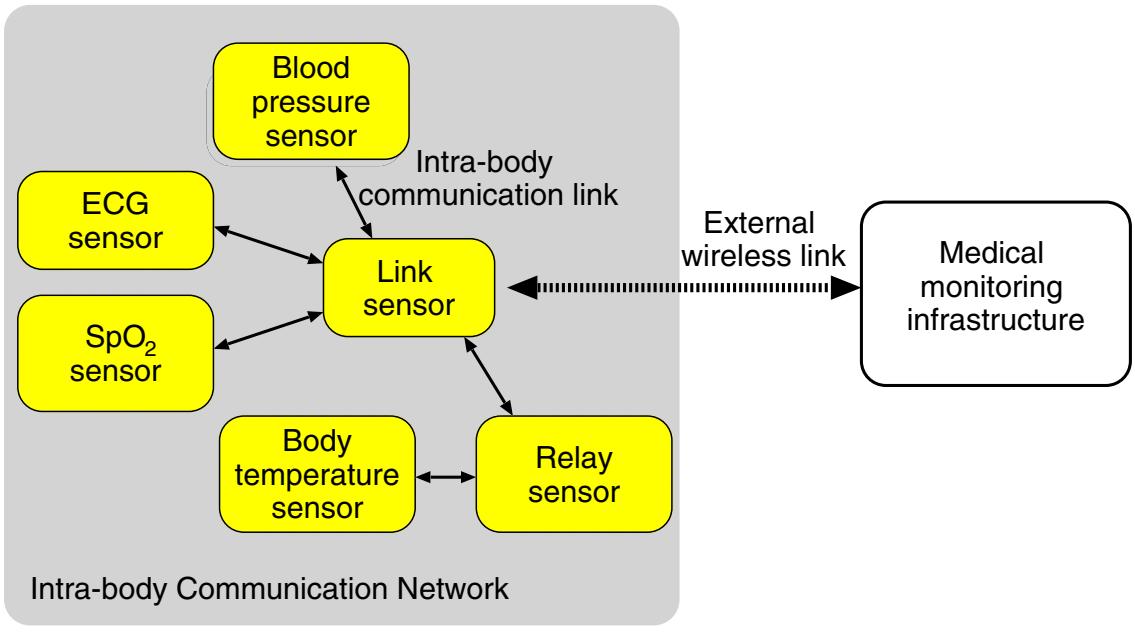

Figure 1.2: Simplified overview of the intra-body communication network: Intra-body communication link between sensor and central link sensor. External wireless link to the remote medical monitoring infrastructure.

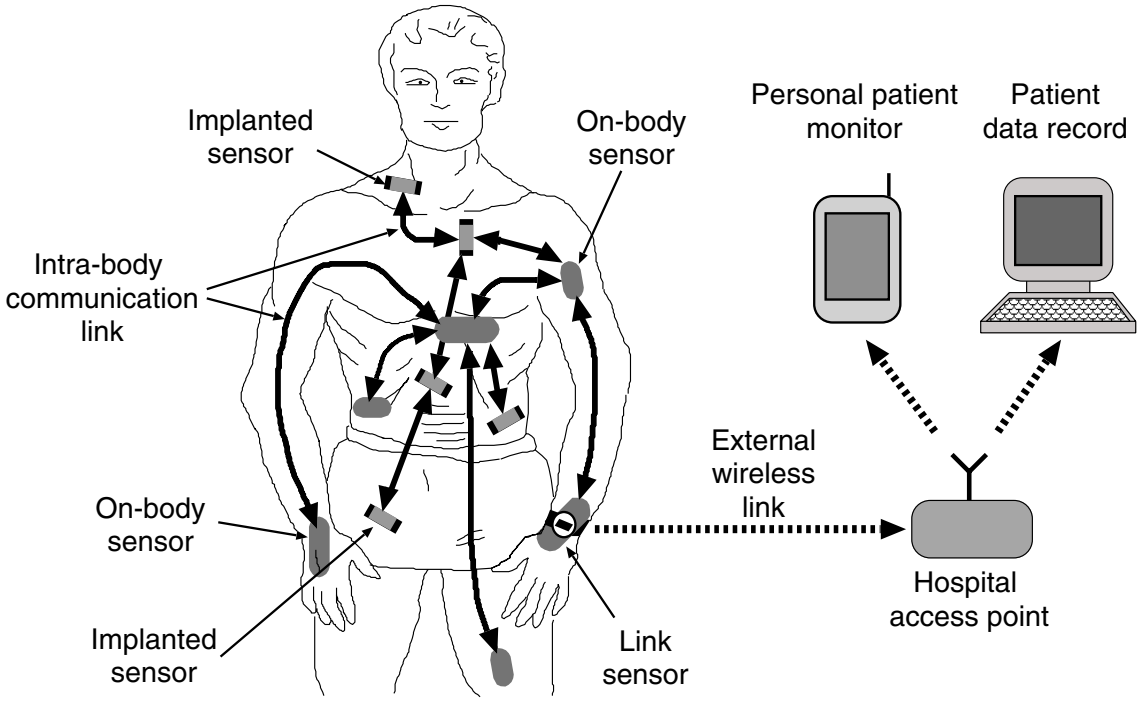

Figure 1.3: Modern hospital monitoring network: Sensors record and transmit their data to monitoring devices. The sensors on or inside the body use intra-body communication techniques for data transmission to other sensors. Eventually, the data is transfered from one central link sensor to a hospital access point and can be analyzed on personal monitoring devices or stored in the patient's electronic record.

The components of the modified network topology are shown in Fig. 1.3. Multiple sensors are distributed over the patient's body to collect and transmit the biomedical data to monitoring units or data storage devices.

The sensors are either attached on-body as band-aids or implanted as pills. Intra-body communication links will allow data exchange between two on-body sensors, two implanted sensors and even between on-body and implanted sensors. All sensor data are transmitted to and collected by the link sensors.

The central link sensor is integrated into a wrist watch or other portable device and communicates to a hospital access point via a high-bandwidth wireless link. The patient's data is monitored on personal patient monitors or stored in the patient's electronic data record. Therefore, the monitoring

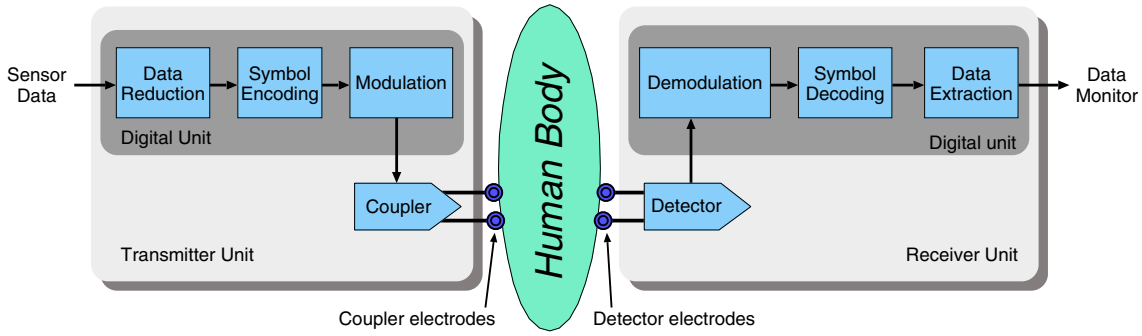

Figure 1.4: Intra-body communication for data transmission between sensors enabled by transmitter and receiver units: The human body acts as the transmission medium.

data is available anytime, online, and in real-time.

The main components of an intra-body communication link are shown in Fig. 1.4. A transmitter unit allows sensor data to be compressed and encoded and transmits the data by a current-controlled coupler unit. The human body serves as the transmission channel. Electrical signals are coupled into the human tissue and distributed over multiple body regions. The receiver unit consists of an analog detector unit that amplifies the induced signal and digital entities for data demodulation, decoding, and data extraction.

State-of-the-Art

The novelty of intra-body communication is the usage of the human body as the transmission medium. The body becomes an integral component of the transmission system. Sophisticated transceivers enable electrical current induction into the human tissue and provide smart data transmission by advanced encoding and compression.

Emerging body transmission systems[1] have shown the feasibility of transmitting electrical signals through the human body. However, detailed characteristics of the human body are lacking so far. Unfortunately, not a lot is known about the influences of human tissue on electrical signal transmission. For advanced transceiver designs, the effects and limits of the tissue have to be carefully taken into consideration.

[1] The most advanced body transmission systems are presented and compared in Chapter 2

Regulations

Safety requirements for limiting exposure to time-varying electric, magnetic, and electromagnetic fields are enforced by national commissions, e.g., EU directives [Eur96, Eur99] and FCC [Fed85].

These regulations are based on international guidelines by the *International Commission on Non-Ionizing Radiation Protection (ICNIRP)* [Int97] and *IEEE Standard for Safety Levels* [C9506] combined with national considerations, e.g., [NRP04, PA02]. Table 1.3 summarizes threshold currents for indirect effects[2]. In general, it has been shown that threshold currents, which produce perception and pain, vary little over the frequency range of 100 kHz and 1 MHz. Below 100 kHz the primary effect of alternating current is nerve and muscle stimulation perceived as a primary sensation of nerve tingling. At increased frequencies from 100 kHz to 10 MHz, the dominant effect changes towards heating, while above 10 MHz the limits are defined in terms of the specific absorption rate (SAR). Temperature rises of less than 1 degrees are considered to be safe, i.e., not resulting in any adverse heating effects.

Table 1.3: Ranges for threshold currents for indirect effects, including children, women and men [Int97].

Indirect Effect	Threshold current [mA]			
	50/60 Hz	1 kHz	100 kHz	1 MHz
Touch Perception	0.2-0.4	0.4-0.8	25-40	24-40
Pain on finger contact	0.9-1.8	1.6-3.3	33-55	28-50
Painful shock	8-16	12-24	112-224	n/a
Severe shock difficulty	12-23	21-41	160-320	n/a

Derived from the guidelines, intra-body communication is restricted by the limits of contact currents [Int03]. Depending on the frequency range, the allowed contact current increases up to 20 mA at 100 kHz and remains constant above according to Tab. 1.4. The occupationally exposed population

[2]Threshold currents for indirect effects is a term used in the standard to express current limits triggering particular physical sensations of the subjects

Table 1.4: Reference levels for time varying contact currents from conductive objects [Int97].

Exposure Characteristics	Frequency Range	Max. Contact Current [mA]
Occupational Exposure	2.5 kHz - 100 kHz	$0.4 \cdot f[kHz]$
	100 kHz - 110 MHz	40
General Public Exposure	2.5 kHz - 100 kHz	$0.2 \cdot f[kHz]$
	100 kHz - 110 MHz	20

consists of professionals who are exposed under known conditions. These people are trained to be aware of potential risks and to take appropriate precautions.

In contrast, the general public comprises individuals of all ages and of varying health status, and may include particularly susceptible groups or individuals. Since the threshold currents that elicit biological responses in children and adult women are approximately one-half and two-thirds, respectively, of those in adult men, the reference levels for contact currents for the general public are set to half the values for occupational exposure.

For the purposes of the clinical trial and type approval, this project followed the Swiss regulations [Sch00, Ber01, Bun94]. All irritation, heating, and destruction of human tissue has to be limited in compliance with these regulations.

1.2 Contributions

The goal of this thesis is to explore the human body as a transmission medium of electrical signals. For this purpose, the dielectric properties of human tissue have been analyzed, models of the body as a transmission channel have been developed, and suitable transceiver architectures have been proposed. Specifically, the contributions to the intra-body communication architecture are as follows:

- Based on cell models and reports on conductivity and permittivity of dedicated tissue, layered tissue models of discrete components and numerical finite-element models have been developed, simulated, and compared with specific tissue components and extended geometries. The results allow the electrical characterization of the body and give explanations of the transmission behavior of the body parts [WLF+05a, WOKF06].

- A dedicated measurement setup has been developed for *in vivo* verification of the simulation results [WLF+05b]. The measurement system allows the coupling of alternating current by differential electrodes in human tissue and measurement of the potential differences at other body locations [WOF+06a]. The feasibility of intra-body communication has been demonstrated and the technology has been explored in a clinical trial among a group of 20 subjects.

- Advanced transceiver architectures have been implemented for coupling signal current into and inside the human body. The implementation of the digital units for on-body transceivers [WFOK06] and a test system for implant communication including four transmitters and one receiver are presented [WHK+07].

- The first silicon implementation of the modified SPIHT algorithm achieves compression ratios of up to 20:1 for ECG signals. The compressed data still contains all significant details for medical diagnosis [WPB+06].

In summary, this thesis attempts for the first time to model and simulate the human body as a communication channel and proposes suitable on-body and implantable transceiver architectures for intra-body communication.

1.3 Outline of the Thesis

Chapter 2 explores the existing intra-body communication approaches. Capacitive and galvanic coupling are presented as the two most advanced body transmission principles.

Chapter 3 introduces models for the intra-body communication channel. Based on the relative permittivity and conductivity of the different tissue layers, electrically equivalent circuits and simulation models are developed in order to simulate the human body as a signal transmission medium.

Chapter 4 presents a dedicated measurement setup for *in vivo* verification of the simulation results. Initial feasibility measurements are conducted and different electrodes are compared.

Chapter 5 summarizes the results of a clinical trial. With the developed measurement system, galvanic coupling is explored and the relations between individual-specific body parameters and electrical signal transmission are concluded.

Chapter 6 presents the implementation of an intra-body communication system for sensor applications. The proposed architecture describes all building blocks of the digital transceiver and the analog front-end. The implementation focuses on future integration into a mixed signal full custom ASIC.

Chapters 7 and 8 give application examples of the novel technology. Chapter 7 shows the adaption of the technology to wireless implants while Chapter 8 reports on an on-body ECG monitoring application that makes use of data compression.

Finally, a summary is presented and conclusions are drawn in Chapter 9.

The acronyms used are summarized in an appended glossary.

Chapter 2

Body Transmission Systems

The fact that electricity can interact with biological processes has been known for more than 2,000 years. The electrical discharge of the torpedo fish was reported to have been used as early as 46 A.D. to treat pain [Rei98]. The beginnings of quantitative bioelectrical science can arguably be ascribed to the investigations of Galvani (around 1790) and later of Volta and Faraday (around 1831). Galvani observed motion in frogs' legs when he touched them with metallic wires. That encouraged further investigations of electrical stimulation. Biological investigations by Faraday demonstrated that interrupted electric current was an effective means of electrical stimulation of nerves. The term *Voltaic* stimulation is used to indicate direct current stimulation, and *Faradaic* to indicate pulsed or interrupted stimulation.

Nowadays, the most rapidly growing area of electrical stimulation is in biomedical technology. Electrical stimulation has increasingly been used as a tool for medical diagnosis, therapy, and prosthesis [LOW$^+$03]. Furthermore, electrical stimulation is investigated by attempts to detect the provoked potential differences in other body parts. The signal transmission is deliberately based on the possibility to detect these signals. In conclusion, body transmission networks deploy sensor communication that is uniquely based on the body proximity. In contrast to standard wireless technologies, body transmission systems benefit directly from the presence of the human body.

Table 2.1: Body transmission systems based on capacitive and galvanic coupling comparing the coupling amplitude, carrier frequency, modulation method, and the achieved data rate.

	Coupling method	Coupling amplitude	Carrier frequency	Encoding	Data rate [bit/s]
Fukumoto [FT97]	capacitive	21 V	90 kHz	FM	0.1 k
Zimmerman [Zim95]	capacitive	30 V	330 kHz	OOK	2.4 k
Reynolds [PRG+97]	capacitive	10 V	70 kHz	FSK	9.6 k
Partridge [PDV+01]	capacitive	22 V	160 kHz	FSK	38.4 k
Fujii/Ito [FIT02]	capacitive	3 V	10 MHz	OOK	n/a
Hachisuka [HNT+03]	capacitive	1V	10.7 MHz	FSK	9.6 k
NTT/Docomo [FSS03]	capacitive	25 V	10 MHz	OOK	10 M
Lindsey [LMHH98]	galvanic	3 mA	37 kHz	FM	n/a
Handa [HSI+97]	galvanic	20 µA	70 kHz	PWM	0.9 k
Oberle [Obe02]	galvanic	4 mA	60 kHz	CPFSK	4.8 k

Several attempts were made to send and receive electrical signals over the human body. Two general methods have been developed:

- Capacitive coupling
- Galvanic coupling

The human body is used as a signal transmission medium through both of these body transmission principles. The differences between the two methods lie in the signal coupling. The induced electrical signal is either controlled by an electrical potential or by a current flow.

In the following, the most important findings on body transmission are introduced by the developed systems indicated in Tab 2.1. The differences can be related to the coupling method, the coupling amplitude, the chosen frequency range, the signal modulation method, and the application-specific data rates.

2.1 Capacitive Coupling Body Transmission

The first successful system was reported by Thomas G. Zimmerman [Zim95] and was known as the *Personal Area Network (PAN)*. The researchers at MIT's media lab discovered that capacitive coupling of the human body to its environment and certain parts of the near field could be exploited to make the human body act as a medium for data transmission. Figure 2.1 depicts a model of the electric near-field produced by a PAN transmitter in body proximity. The PAN transceiver is composed of a transmitter and a receiver unit, each with two electrode plates. The electric field E_a, induced by a signal electrode of the *PAN* transmitter, passes through the body and flows toward ground. The goal is for the receiver unit to detect the electric field E_s. The field E_s is extremely small because a significant part of the electric field E_a is canceled by the electric field E_b established toward the ground electrode

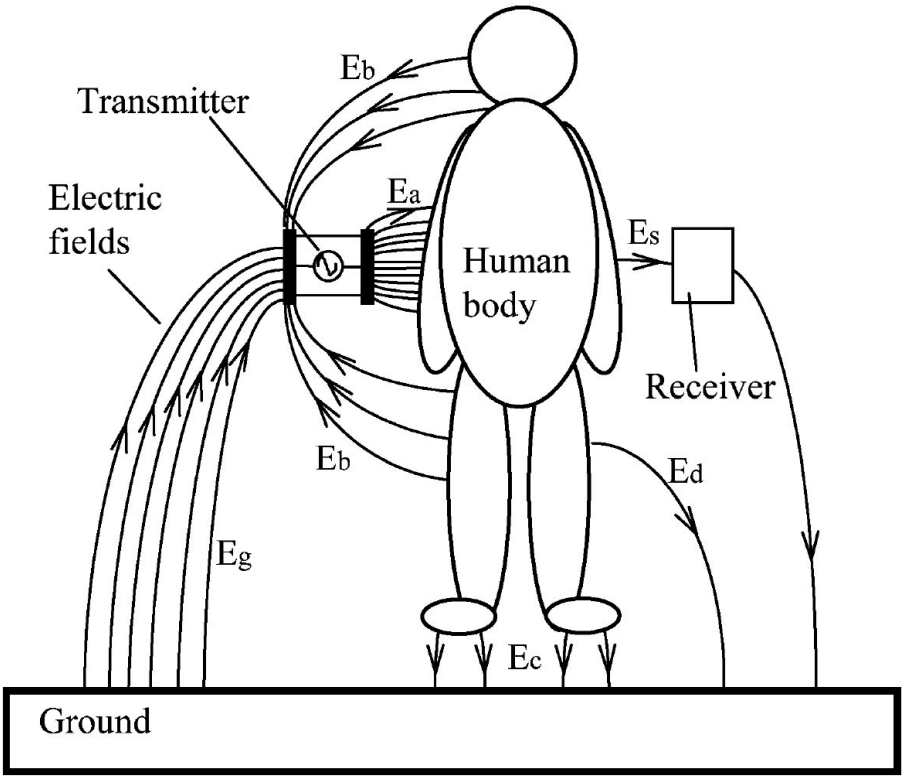

Figure 2.1: Electrical fields produced by PAN transmitter [Zim95]: A small portion of the electric field induced by the transmitter reaches the receiver.

of the transmitter. In addition, a major part of the electric field E_c escapes through the feet, which are in direct contact with the ground. The return transmission path is established by the second plate of each unit via ground. According to Zimmerman [Zim96], near-field communication can operate at very low frequencies and low transmission power. The prototype of the PAN transmitter operates at 330 kHz, 30 V, with a transmission power consumption of 1.5 mW for charging the electrode capacitance. The PAN technology was proposed for integration into a custom CMOS chip to achieve lower size and cost. A demonstrator system allowed the modest transmission of 2.4 kbit/s. Digital information has been encoded using on-off keying with quadrature detection to reduce stray interference and increase the receiver sensitivity. Several interesting applications have been proposed [ZSP+95]. The potential of this technology lies in identification and biomedical applications.

The principle of Zimmerman's PAN system has served as a reference for further capacitive coupling body transmission. The main components and the application to the body can be identified as depicted in Fig. 2.2: a transmitter unit consists of an encoder for data modulation and a coupler unit. One of the two coupler electrodes connects to the body, while the other conducts ground. At the receiver side, the detector records the signal as a potential difference between the two detector electrodes; one is connected to the body and the other to ground. A subsequent decoder demodulates the transmitted signal.

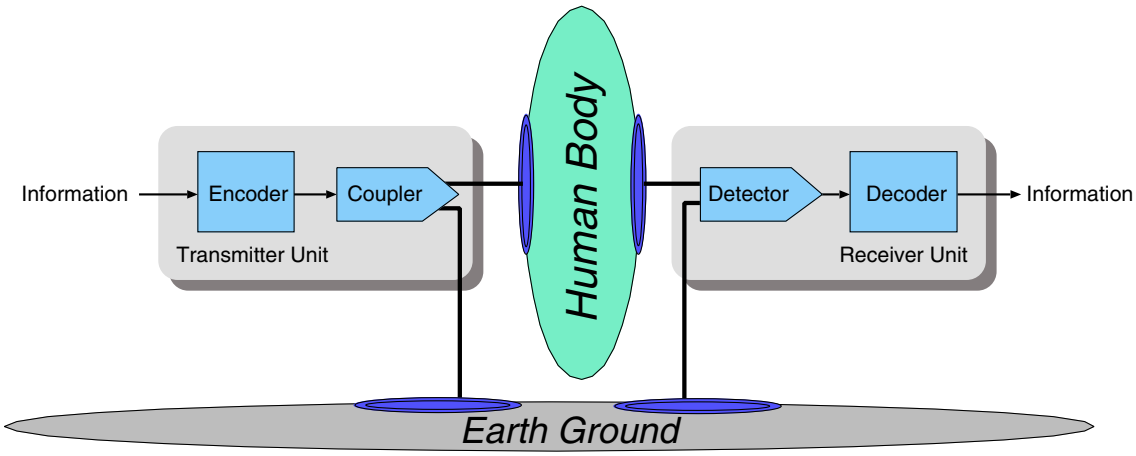

Figure 2.2: Capacitive coupling for data transmission between transmitter and receiver units: One signal path is established through the human body while the return path has to be connected by earth ground.

Further systems have been developed with different coding schemes and coupling parameters.

The physical limits of intra-body signaling was explored by Gray [Gra97]. The channel capacity analysis revealed that the noise present in PAN devices is dominated by amplifier noise and external interference. Furthermore, it was attempted to increment the baud rate from 300 to several kbaud. The prototype uses on-off keying (OOK) as well as differential binary phase shift keying (BPSK). A final hardware design, led by Matthew Reynolds [PRG+97], reached a speed of 9600 baud employing a phase-locked- loop (PLL) for analog demodulation and implemented frequency shift keying (FSK).

K. Partridge *et al.* [PDV+01] presented an improved system operating up to 38.4 kbit/s. The carrier frequencies were chosen at 180 kHz and 140 kHz for FSK modulation. In addition, a tunable amplitude level of up to 22 V was implemented. Experiments show that the plate size and shape have only minor effects, but that the distance of the body to the transceiver plate significantly effects the signal strength. Furthermore, the signal attenuation of devices with poor ground coupling particularly suffer.

Direct coupling by Masaaki Fukumoto *et al.* [FS94, FT97] is a modified version of the basic capacitive method. Ring-shaped *FingeRing* transmitters are worn on each finger and used for command and data input by finger-tip typing action. The receiver unit is worn on the human arm. Thus, the return path is not coupled through ground but the air only. The system operates by analog frequency modulation at frequencies within 50 kHz to 90 kHz for transmitting a simple protocol of ID numbers.

Katsuyaki Fujii and Koichi Ito [FIT02] presented a wearable ID key that allows users to personalize a receiver device by simple touch. Data is transferred via the body by a network module called *TouchNet*. They studied the receiving level in relation with the electrode locations of their wearable devices [FIT03]. Little is known about the transmission mechanisms of such devices in the physical layer. Therefore, a simulation model of the transmitter and the receiver attached to the arm has been proposed using the Finite-Difference Time-Domain (FDTD) method. Based on this model, the difference in the received signal levels was estimated under various conditions of the transmitter and receiver electrode structure. The size of the electrodes is detected as one of the key issues. It has been discovered in these simulations that a ground electrode close to the transmit electrode strengthens the

generated electric field, while the presence of a ground electrode close to the receiver electrode reduces the received signal level [FI04].

The intra-body communication devices proposed by Keisuke Hachisuka *et al.* [HNT+03] realized digital data transmission at 9.6 kbit/s using an FSK transmitter and receiver devices. The carrier frequency of 10.7 MHz is the intermediate frequency of FM radio receivers, meaning that the proposed system can make use of a wide selection of inexpensive commercial radio frequency devices [HTK+05, HTT+05].

Two Japanese telecommunication companies, Nippon Telegraph & Telephone Corp. and its subsidiary NTT DoCoMo Inc., have developed a technology that turns the human body into a broadband link. The technology uses the body's conductivity and allows the exchange of data between personal digital assistants (PDA) by human touch [FSS03]. The intra-body communication system is enabled by electro-optic probes [SFOK04]. The electric field passed through the electro-optic crystal is detected as changes in the polarization of a laser beam [FSS03]. The electro-optic sensor features a high input impedance, high-sensitivity and high-speed operation capability. A data rate up to 10 Mbit/s is claimed.

The method of capacitive coupling has several weak points:

- The return path of the signal has to be guided. In the presented systems, the conduction with ground is a must for whole-body transmission.
- The dominant signal transmission channel is not inside the body but on the surface of the arm, because the signal is distributed as a surface wave.
- The capacitive plates themselves are likely to emit stray fields.
- Transmission by radiation through air becomes increasingly relevant the higher the carrier frequency is increased.

In conclusion, capacitive coupling is highly dependent on the environment. Galvanic coupling, as presented in the next section, reduces this dependency.

2.2 Galvanic Coupling Body Transmission

Galvanic coupling follows the approach of coupling alternating current into the human body. A simplified presentation of the method is shown in Fig. 2.3. The two electrodes of the coupler and the two electrodes of the detector are coupled to the human body. Therefore, ground is not required for reference as in the method of capacitive coupling (Fig. 2.1).

The signal is applied differentially over the two coupler electrodes. A primary current flow between the coupler electrodes is established and a small secondary current propagates further into the conductive body parts. The induced current results in an alternating potential difference between the detector electrodes. In this case, ionic fluid within the human body, rather than electro-magnetic waves in free space, is the carrier of the information.

In comparison with capacitive coupling (Fig. 2.2), galvanic coupling feeds alternating current into the human tissue as shown in Fig 2.4 with the aid of two electrodes. The functional blocks of the transmitter unit, encoder and coupler, are adapted to the current-controlled signal transmission. The same applies to the receiver unit, consisting of detector and decoder.

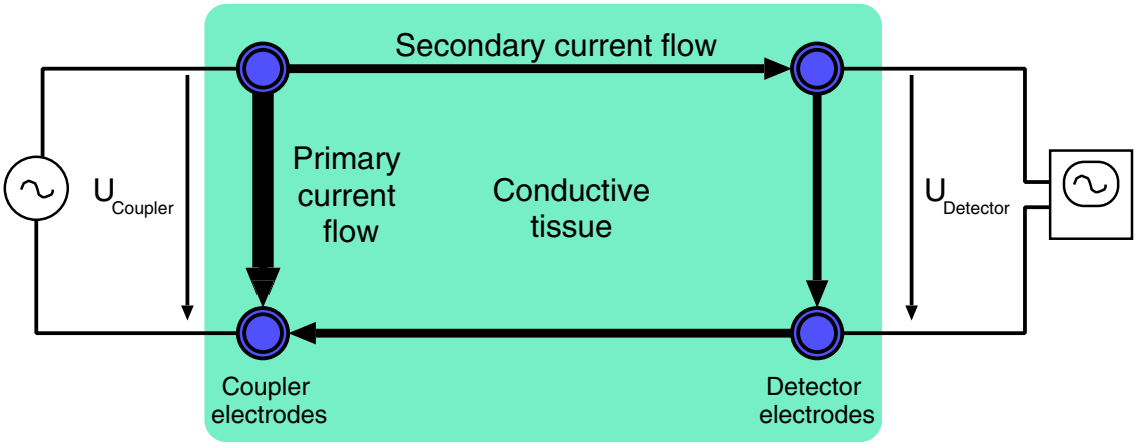

Figure 2.3: Concept of galvanic coupling: The applied alternating current establishes a current flow between the coupler electrodes; a secondary current flow propagates further into the conductive body parts and can be detected as a potential difference between the detector electrodes.

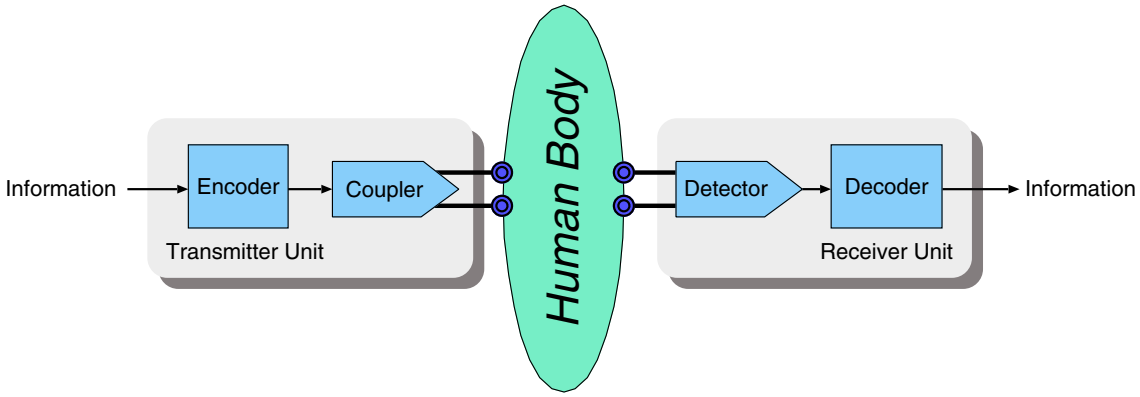

Figure 2.4: Data transmission by galvanic coupling between transmitter and receiver units: Differential current is coupled into the human body by the pair of coupler electrodes and sensed by the pair of detector electrodes.

A small number of prototypes have been developed using this galvanic coupling method for signal transmission through human tissue.

A low-power consumption wireless system for ECG monitoring has been proposed by Takashi Handa *et al.* [HSI+97]. It consists of an ECG detector located on the chest and a relay transmitter placed at the wrist. Between the detector unit and relay transmitter, the signal is sent as an alternating 20 µA current flow through the body tissue. The system can be driven by a very small power source, since this implementation achieves a very low-power signal transmission of 8 µW. The pulse-width modulator frequency is 900 Hz, and the carrier frequency is 70 kHz.

The goal of Derek P. Lindsey *et al.* [LMHH98] was to reduce the space requirements for implant electronics in *in vivo* telemetry applications. A new data transmission method was developed and tested that utilizes the ionic properties of body fluids as the transmission medium. Motivated by an application using the new method to transmit information from a sensor which measures tension in anterior cruciate ligament grafts, a sine wave was injected into a cadaver leg using platinum electrodes implanted into the lateral femoral epicondyle. The signal was detected by electromyogram (EMG) surface electrodes. For the proposed applications, a current of 3 mA was injected at a frequency of 37 kHz.

Joe Schulmann [SMW+06] describes the BION, a broadly applicable platform technology for minimally-invasive neural stimulation. The prototype is designed to send bi-directional messages on a 5 MHz wide radio channel with a transmission current of 3 mA. The injectable stimulator, in the form

of a BION implant, enables a multi-channel battery-powered communication sensor.

Michael Oberle [Obe02] presented a design and the implementation of a low-power biomedical communication approach. The system describes a signal transmission based on the dielectric characteristics of human tissue. This galvanic coupling approach implements continuous phase frequency shift keying (CPFSK). By preventing abrupt changes at the bit transition instants, this leads to improved spectral efficiency and rapid spectral roll-off. The symbols are encoded at the frequencies of 51.2 kHz and 61.4 kHz.

2.3 Discussion

In conclusion, the survey of existing solutions using the conductivity of human tissue shows a broad range of approaches. Even if some attempts may sound like science fiction, it is possible to propagate electrical signals through the human body.

- Capacitive coupling has been implemented in several approaches. The data rate has been increased up to 10 Mbit/s. However, the drawback of a reference ground has always remained.
- Galvanic coupling omits the weak points of capacitive coupling. The transmission is no longer dependent on a return path by earth grounding due to the fact that the current propagation takes place only within human tissue. The presented galvanic approaches feature only low data rates that have not reached the desired transmission speed of the proposed sensor network. Therefore, more sophisticated transceivers shall enable higher data rates using the human body channel more efficiently.

So far, none of the presented works has investigated human body properties nor carried out a model of the human body as a transmission medium. The method of galvanic coupling has been proposed without detailed studies on the signal transmission and the biological processes occurring in the human tissue. However, it is of particular interest which human tissue layers are involved the most and what the biological limitations of the transmission method are.

Therefore, tissue models are required and appropriate simulations shall investigate the signal propagation through the human body.

Chapter 3

Channel Models of the Human Body

Intra-body communication denotes the technology of signal transmission through the body for on-body and implanted sensor communication. Electrical signals are transmitted by the galvanic coupling of alternating currents in the milliampere range. Thus, the human body becomes the transmission channel of the communication system. A profound understanding of its channel characteristics and a simulation model are required for defining the channel constraints and the subsequent system constraints of a transceiver design.

The most crucial questions are:

- Which tissue layers contribute to the current flow most?
- How large are the differences in transmission characteristics among the different parts of the body?
- What body constitution and fat/muscle/fluid combination best supports the signal transmission?
- To what extent do electrode type and size variations influence transmission?

These points shall be targeted through the investigation of equivalent circuit models based on the dielectric properties of human tissue.

Figure 3.1 schematically depicts the human arm and the setup of galvanic coupling. The three tissue layers, skin, muscle and bone, build a highly simplified model. In order to investigate the tissue parameters and equivalent electrical impedances, an alternating current generated in the coupler unit is injected between the two coupler electrodes. The detector unit senses the transmitted signal through the two detector electrodes. The attenuation factor between the coupler and the detector electrodes was calculated using

$$Attenuation[\text{dB}] = 20 \cdot \log_{10} \left(\frac{U_{Detector}}{U_{Coupler}} \right) \tag{3.1}$$

where $U_{Coupler}$ denotes the voltage between the coupler electrodes and $U_{Detector}$ the voltage at the detector electrodes.

In this chapter, the channel models of intra-body communication are introduced. Transmission based on galvanic coupling is compared to the electrical stimulation of human tissue in Sec. 3.1. Section 3.2 shows an analytical model of the transmission channel. In Sec. 3.3, the modular models of the human body are developed, based on cell behavior when exposed to electrical stimulation and on the dielectric properties of different tissue layers. Section 3.4 combines the human body and the coupling method in a simple body model, leading to the layered structure of human tissue in Sec. 3.5. In Sec. 3.6, finite-element models allow the simulation of more advanced body geometries starting with the human arm.

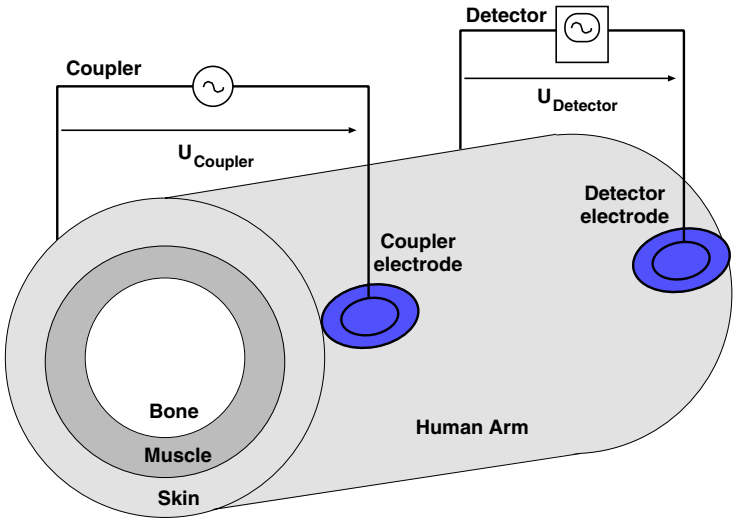

Figure 3.1: Simplified view of a human arm with the three tissue-layers skin, muscle, and bone.

3.1 Existing Electrical Stimulation of Tissue

The setup shown in Fig. 3.1 is quite similar to the approach of electrical impedance tomography (EIT) and comparable to functional electrical stimulation (FES). These methods make use of the electrical conductivity of human tissue for diagnostics and treatments. According to Tab. 3.1, DC and low alternating currents of a few mA are applied.

Electrical Control of Biological Mechanisms

In functional electrical stimulation (FES), biological mechanisms are influenced or explicitly triggered by externally applied currents. The study of electrical body signals produced by biological processes shows that their power spectrum mainly covers the low frequency range. For example, currents generated by the heart have a power density spectrum that lies mainly below 1 kHz, while most other electro-physiologic sources (e.g. those underlying the EEG, EMG, EOG) are of even lower frequencies. Models were used to find the parameters that have the highest influence on nerve activation during stimulation [KK06].

Resistivity Visualization for Medical Diagnosis

Electrical impedance tomography (EIT) attempts to image the internal organs and structure of the body by measuring tissue resistivity [HJ78]. A typical EIT system places multiple electrode pairs around the body (e.g. 24 electrodes), applies a constant current to one electrode pair (coupler), and records the potential at the remaining electrodes (detectors). The potential arises from the tissue impedance between two electrodes. Sets of impedance measurements are collected for every single electrode pair. These impedance

Table 3.1: Biomedical applications coupling electrical currents to the body.

Type / Purpose	Frequency	Current
Electrical stimulation	below 1 kHz	µA up to 0.9 A
Impedance tomography	DC	4 mA
Impedance analysis	DC - 500 kHz	0.5 - 4 mA
Intra-body communication	10 kHz - 1 MHz	1 mA

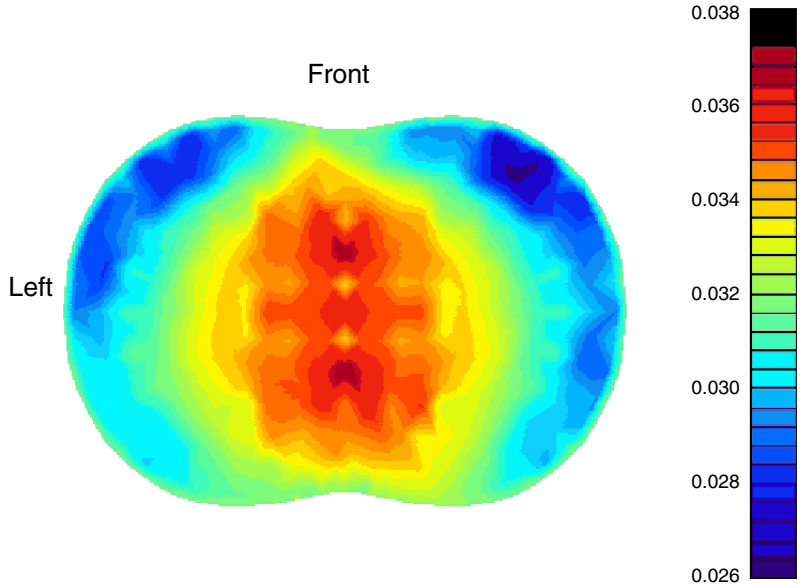

Figure 3.2: A time averaged EIT image of a cross section of a human chest [KML01].

data are used to reconstruct the tissue impedance distribution in the volume between the electrodes. This allows a low-resolution image of the body organs and tissue to be derived as shown in Fig. 3.2. The cross-sectional image of the distribution of conductivity shows the body structure by assuming differences in conductivities of human tissue in the range from 1.54 S/m for cerebrospinal fluid to 6 mS/m for bone.

Despite the fact that the goal of intra-body communication is quite different, there are several analogies between these approaches. In electrical impedance tomography (EIT) currents are injected with the goal to detect the impedance distribution of human tissues [BB84, PL02, SBN+01, SGS95]. In functional electrical stimulation (FES) models were used to find the parameters that have the largest influence on nerve activation during stimulation [KK05]. In order to investigate the body parameters, several dielectric models have been developed. While EIT targets higher resolution and FES explores the effects on the human nerves, intra-body communication primarily searches for a low attenuation of the transmitted signals.

Furthermore, intra-body communication not only focuses on the tissue impedances at constant currents but also for time-varying currents. The desired body models shall give explanations at the frequency range up to 1 MHz. Therefore, the parametric models of the dielectric properties of human tissue have to be extended over the dedicated range.

3.2 Analytical Channel Model

In order to identify the major influences to the transmission channel, an analytical model is drawn in Fig. 3.3. The coupling behavior, the body conditions, and external noise sources are modeled.

- Both the coupler and the detector electrodes attenuate the transmitted signal.
- The dielectric tissue parameters define the attenuation behavior of the human body. The tissue models shall provide better explanations on the attenuation dependency of the tissue properties and the general geometry setup, e.g., distance and structure. The clinical trial will investigate the subject-specific body properties, e.g., defined by extra-cellular and intra-cellular water content.
- Additive in-band noise is caused by external devices, especially other wireless communication units, e.g., RFID.
- Human body noise is approximated by additive white noise.

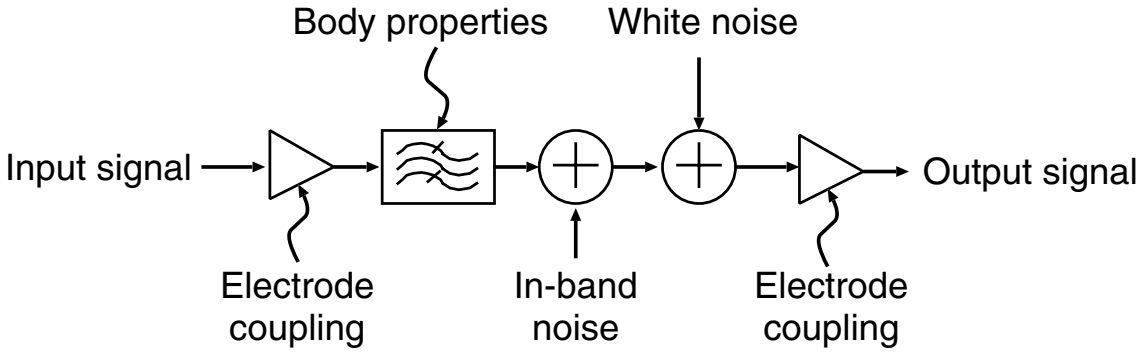

Figure 3.3: Analytical model of the body communication channel: The transmitted signal is attenuated by the coupling electrodes, filtered based on inter-cellular and extra-cellular water distribution and added with noise caused by body effects and other in-band noise sources.

3.3 Dielectric Properties of the Human Tissue

In order to understand the pathway of electrical current flow through the human body, the tissue has to be characterized in terms of its dielectric constants. The findings from measurements shall serve as the basis for a parametric model of the dielectric properties. Derived equivalent circuits shall build the starting point for layered tissue models.

Experimental Findings on the Dielectric Properties

The conductivity of human tissue is based on the cell properties. Cells are membrane bounded compartments filled with a solution of certain chemicals and salt concentration. Groups of cells perform specialized functions and are linked by an intricate communication system. The cell membrane maintains an ion concentration gradient between the intra-cellular and extracellular spaces. This gradient creates an electrical potential difference across the membrane which is essential to cell survival. Electrical gradients are necessary to support the transport of oxygen, carbon, dioxide, and nutrients. Therefore, the cell membrane has electrically insulating qualities to maintain the electrical gradient. Biologically, the cell membrane functions as a permeable barrier separating the intra-cellular (cytoplasm) and extracellular components [Bro06].

The specific resistances of various body tissues have been measured by Schwan [Sch57]. The results showed that the resistivity decreases slowly as the frequency increases up to 10 kHz. Foster *et al.* [FS89] review the dielectric phenomena in biological materials and their interpretation in terms of interactions at the cellular level. Barber & Brown [BB84] presented a survey on the conductivity values of mammalian tissues comparing results at 100 kHz. The human arm showed a conductivity of 0.42 S/m longitudinal, 0.15 S/m transverse. Lung tissue ranges from 0.14 S/m to 42 mS/m during expiration and inspiration, respectively. Blood is reported to have a conductivity of 0.66 S/m, and the conductivity of fat is 40 mS/m. The lowest conductivity is reported for wet bovine bone with 6.02 mS/m. Although the reported conductivity values for any tissue might vary considerably, it is expected that the bulk resistivity of the human tissue is in the order of ten Ωm.

The most profound overview of the relative permittivity and conductivity

of tissue was published by Gabriel *et al.*. In [GLG96b], the current state of knowledge in terms of dielectric tissue properties over ten frequency decades was assessed. Measurements in the frequency range from 10 Hz to 20 GHz provide the basis for the evaluation and analysis of the mammalian tissues. Nevertheless, the results are based on homogenized animal tissue. Differences between living and dead human tissues are to be expected. In [GLG96a], the measured values of the relative permittivity and conductivity were presented. The relative permittivity decreases from values in the range of 10^5 at a few hundred Hz to less than 100 in the GHz range, whereas the conductivity increases starting around 10^{-4} S/m to above 1 S/m in the same frequency range.

The electrical properties of tissue and cell suspensions change with frequency in three distinct steps termed as α, β and γ dispersions:

- α dispersion in the frequency region below 1 kHz is associated with ionic diffusion processes on both sides of the cellular membrane and with the polarization of ions near charged surfaces in the tissue. The relative permittivity reaches values of more than 10^5.
- β dispersion, in the range of 100 kHz to 10 MHz, is due mainly to the polarization of cell membranes which act as barriers to the flow of ions between the intra- and extra-cellular media.
- γ dispersion in the gigahertz region is due to the polarization of water molecules.

The conditions and the physics of the tissue material vary over time. Nonetheless, as a first approximation, the involved tissue layers can be parameterized by their dielectric constants, which are material- and frequency-dependent.

Parametric Model of the Dielectric Tissue Properties

As seen in the section above, the dielectric tissue, represented by the relative permittivity ε_r and the conductivity σ, is characterized by the three main relaxation regions α, β and γ at low, medium and high frequencies.

In their simplest forms, each of these relaxation regions is caused by a polarization mechanism characterized by a single time constant τ. The Cole-Cole

equation [CC41] formulates this as a first approximation with

$$\varepsilon^*(\omega) = \varepsilon_\infty + \frac{\Delta\varepsilon_n}{1 + (j\omega\tau_n)^{(1-\alpha_n)}}. \tag{3.2}$$

It contains a frequency independent part, which is due to ionic conduction, and a frequency-dependent part based on dielectric relaxation. Each dispersion region is broadened depending on the composition of the biological material by introducing the distribution parameter α. In addition, the decrease in the three distinct dispersion regions is described by the summation of multiple Cole-Cole equations. For multiple contributions, the frequency-dependent permittivity then is

$$\varepsilon^*(\omega) = \varepsilon_\infty + \sum_n \frac{\Delta\varepsilon_n}{1 + (j\omega\tau_n)^{(1-\alpha_n)}} + \frac{\sigma_i}{j\omega\varepsilon_0}. \tag{3.3}$$

$\varepsilon^*(\omega)$	complex relative permittivity
α_n	distribution parameter
τ	relaxation time constant
ε_0	permittivity of free space
ε_∞	permittivity at frequencies $\omega\tau \gg 1$
ε_s	permittivity at frequencies $\omega\tau \ll 1$
$\Delta\varepsilon = \varepsilon_s - \varepsilon_\infty$	magnitude of the dispersion
σ_i	static ionic conductivity

The relaxation time constant τ depends on physical processes: τ in the range of

- picoseconds indicates a reorientation of molecular dipoles
- seconds is due to ion effects

Equation 3.3 can be used to predict the dielectric behavior over the desired frequency range. The corresponding equation for the tissue conductivity can be derived from the general relation between conductivity and permittivity

$$\frac{[\varepsilon_s - \varepsilon_\infty] \cdot \varepsilon_0}{\tau} = \sigma_\infty - \sigma_s \tag{3.4}$$

σ_∞	conductivity at frequencies $\omega\tau \gg 1$
σ_s	static conductivity

The complex conductivity σ^* and the complex specific impedance z^* of the tissue are

$$\sigma^* = j\omega\varepsilon_0\varepsilon^* = \sigma_\infty + \omega\varepsilon_0\varepsilon_\infty + \frac{\sigma_s - \sigma_\infty}{1 + j\omega\tau} \tag{3.5}$$

$$z* = \frac{1}{\sigma^*} \tag{3.6}$$

The dielectric properties are defined based on Eq. 3.3 and parameter estimations for α_n, τ_n, $\Delta\varepsilon_n$, σ_i, and ε_∞ by [GLG96c].

The simulation results in Fig. 3.4 show:

- Up to a frequency of 10 MHz, the conductivity of muscle tissue is between 10 and 10^3 times higher than the conductivity of skin.
- The conductivities of dry and wet skin differ by more than a factor of 100. This will have some influence on the expected change of attenuation by the human tissue.
- The relative permittivity of muscle tissue is 10^3 times higher than the relative permittivity of dry skin up to 100 kHz, and the frequency behavior is similar to wet skin. For the common case of dry skin it

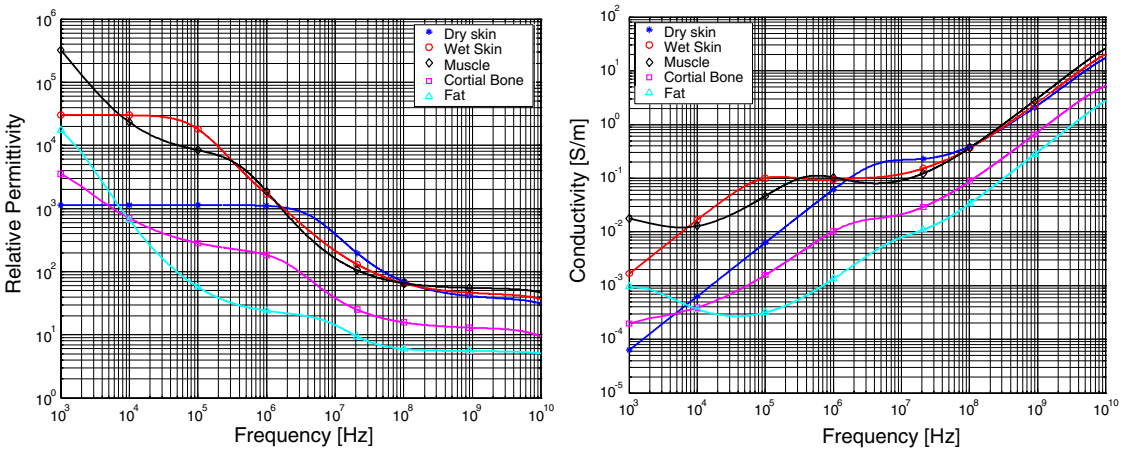

Figure 3.4: Simulated relative permittivity and conductivity of wet skin, dry skin, muscle, bone and fat tissue calculated with the Cole-Cole equation Eq. 3.3 and the dielectric parameters from Gabriel [GLG96c].

can be assumed that the muscle tissue will play the dominant role for signal transmission.

- The conductivity increases rapidly above 10 MHz. Low impedances mean an increase in power consumption, since higher output currents will be necessary to drive the output signals between the electrodes.

- The almost constant conductivities and permittivities for skin and muscle suggest good signal transmission between 100 kHz and 1 MHz.

Equivalent Tissue Models

Dielectric properties are usually represented as a combination of capacitive and conductive elements. An equivalent circuit model can be derived knowing the dielectric parameters of a dedicated tissue. Figure 3.5 shows the equivalent circuit of Eq. 3.3 for a single time constant and $\alpha = 0$.

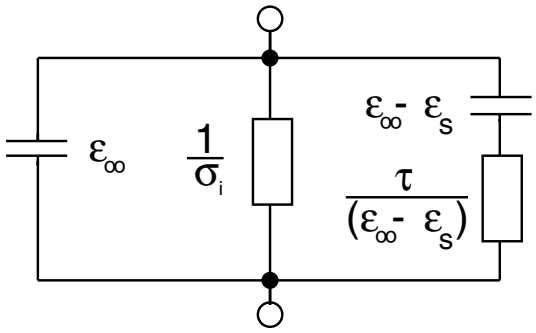

Figure 3.5: Equivalent circuit that models the Cole-Cole equation for a single time constant τ and the distribution parameter $\alpha = 0$.

Figure 3.6a illustrates cell behavior under exposure to an alternating current. Applying a low-frequency voltage to the tissue will create a current, which flows mainly through the extra-cellular fluid since the impedance of the membrane is very large at low frequencies. At higher frequencies, current flows through the extra- and intra-cellular fluids.

The equivalent circuit for a cell embedded in extra-cellular fluid is shown in Fig. 3.6b. R_e models the extra-cellular fluid resistance, C_e models the current flow of the extra-cellular fluid as a function of the frequency. The

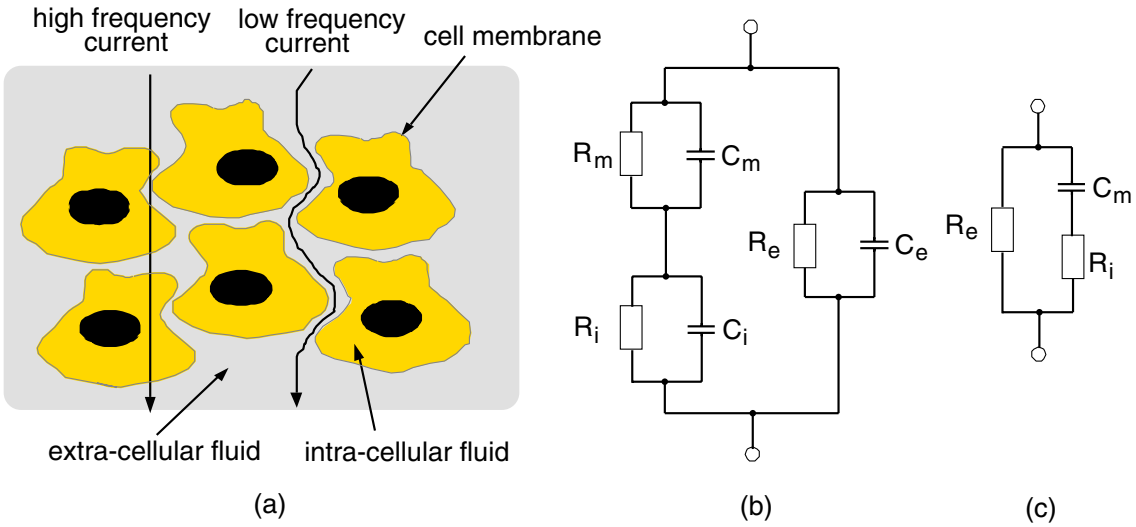

Figure 3.6: (a) Tissues and current flow, (b) schematic diagram of the equivalent circuit of a cell, (c) simplified circuit.

components of the cell membrane are represented by R_m and C_m, and those of the intra-cellular fluid by R_i and C_i.

The equivalent circuit can be simplified in the frequency range of 1 kHz to 500 kHz. Figure 3.6c shows the simplified circuit, consisting of an extra-cellular resistive part R_e in parallel with the capacitive C_m and resistive R_i components, representing the intra-cellular and the cell membrane contributions, respectively.

In order to represent the significant tissue components, a body model will be assembled modularly composed of the corresponding electrical equivalent components.

3.4 Simple Discrete Body Model

The goal of a simple discrete body model is the modeling of the main dependencies on the skin layer condition and the coupling electrodes. The simple model shall reduce the body complexity to its minimum and shall be compared later with more detailed approaches.

Intra-body transmission can be described by a four-terminal circuit model with 10 impedances, as shown in Fig. 3.7

$$H = \frac{Z_o(Z_b - Z_t)}{2Z_tZ_b + Z_oZ_b + Z_oZ_t}. \tag{3.7}$$

This simple body model takes into account longitudinal transmit (Z_t), input (Z_i), and output impedances (Z_o) as well as cross impedances (Z_b) between the coupler and detector electrodes. The body impedances can be described in analogy to Fig. 3.6c as an equivalent circuit of the resistances R_e and R_i and a capacitance C_m.

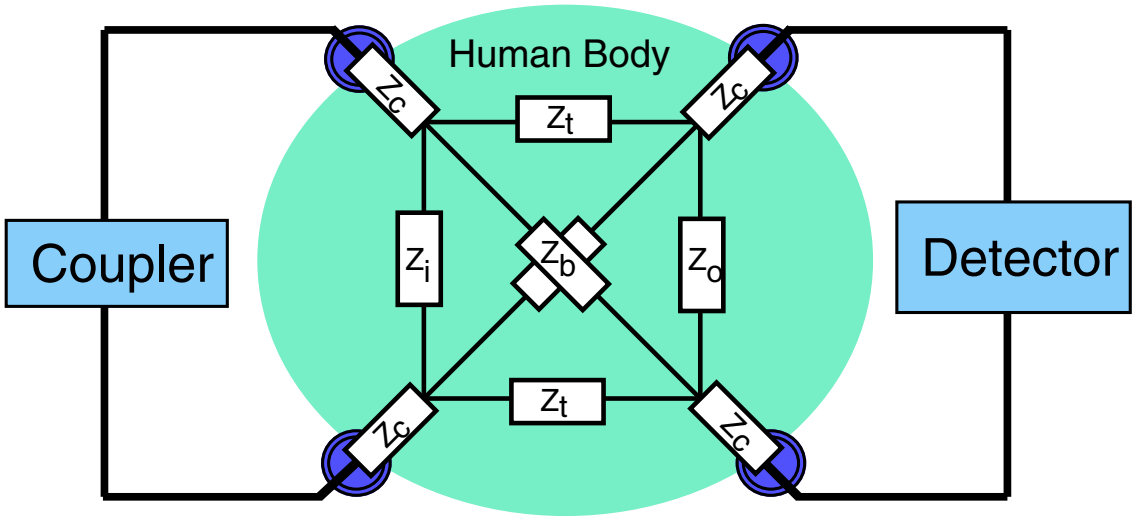

Figure 3.7: Simplified circuit model of the human body modeling the coupling electrode (Z_c), input (Z_i), and output (Z_o) impedances as well as longitudinal transmit impedances (Z_t) and butterfly cross impedances (Z_b).

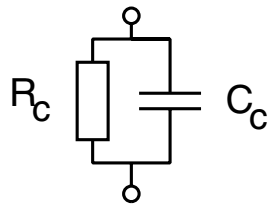

Figure 3.8: Equivalent circuit for electrode-skin contact: Coupling impedances Z_c composed of R_c and C_c in a parallel circuit.

The entire transfer function includes the coupling electrode impedances (Z_c as a parallel circuit of R_c and C_c as shown in Fig. 3.8)

$$G = 20\,log_{10}\left\{\frac{H}{1+Z_c\left[\frac{1}{Z_t}+\frac{1}{Z_b}+H\cdot\left(\frac{1}{Z_b}+\frac{1}{Z_i}-\frac{2}{Z_t}\right)\right]}\right\}. \tag{3.8}$$

In conclusion, the simple body model covers the main parameters for modeling the human transfer characteristics in the frequency range from 10 kHz up to 1 MHz. It offers a very effective means to characterize the transmission channel. Furthermore, it gives hope for parameterizing the few discrete elements by subject-specific anatomical parameters. Basic parameters, e.g., equivalent channel length, width and depth, can be varied.

However, it only takes an abstracted geometry of the human body into account. A more complex layered tissue model will allow more appropriate specification of the significant geometry and tissue layers.

3.5 Layered Tissue Model

The human body is a complex structure of different tissues, organs, and bone structures of variable geometries. In a first approximation the major contribution of the skin was modeled with the simple, discrete body model. In order to model the geometrical and physical properties of simple anatomical structures like the extremities, arms and legs were approximated by three types of tissue: skin, muscle and bone.

Figure 3.9 shows a schematic representation of the layered structure of human tissue with the setup of galvanic coupling. The skin is the most im-

portant tissue due to its contact with the attached coupler and detector electrodes and due to its wide variability modeled with different dielectric properties for dry and wet skin. Furthermore, muscle is important due to its high conductivity. The bone layer, as the deepest tissue layer, is of less importance. Its significance will increase for more complex structures such as joints.

Human tissue can be transformed into an equivalent simulation circuit as represented in Fig. 3.9. The three main layers, identified as skin, muscle and bone, are constructed by a mesh of complex impedances, each representing an equivalent circuit according to the simplified circuit of Fig. 3.6c. The impedances Z have two indices: the first index defines the layers of skin s, muscle m or bone b, whereas the second index indicates the geometrical orientation. Each layer is composed of transversal t and longitudinal l cell components; longitudinal and transversal impedances build the uniform layers. Those layers are interconnected by impedances between skin-muscle Z_{sm} and muscle-bone Z_{mb}. The impedances Z_c model the coupling impedances between the electrodes and the skin. The physical and the di-

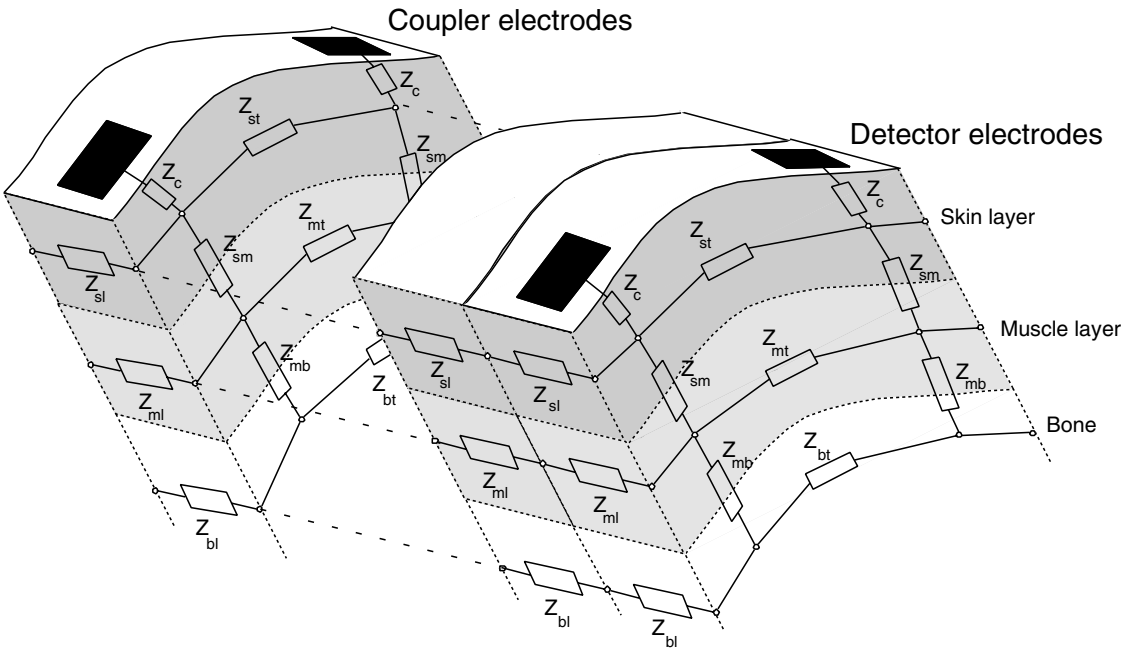

Figure 3.9: Model of multi-layered tissue with the galvanic coupling setup: Skin, muscle and bone are constructed of equivalent Cole-Cole circuits and connected in a mesh.

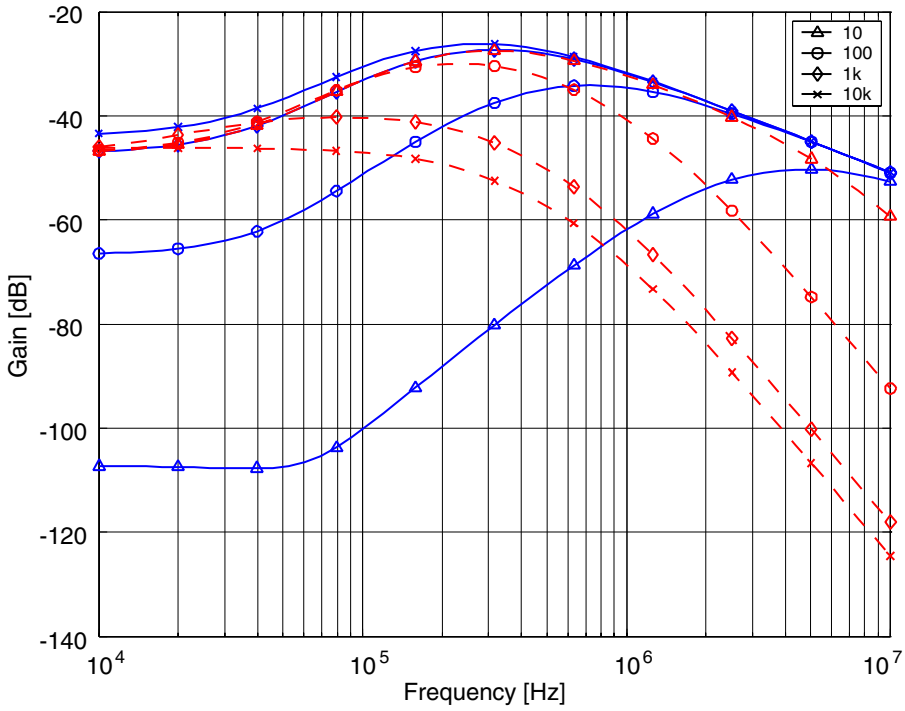

Figure 3.10: Simulation results of the layered tissue model with increased resistance R_e of 1, 10, 100, 1k and 10 kΩ on the skin layer for the longitudinal Z_{sl} (solid) and transversal Z_{st} impedance (dashed).

electric properties can be applied to skin, muscle and bone layers according to the parameter defined by the complex impedance of Eq. 3.6.

Galvanic coupling is simulated with the setup of coupler and detector units as depicted in Fig. 3.9. The coupler drives an alternating current through the two electrodes and the tissue in between. A smaller portion of this current will flow through the skin layer between the electrodes, whereas the majority will be conducted by the deeper muscle tissue. This changes if the outermost layer of the skin is wet. The muscle layer will conduct a small part of the current longitudinally along the muscle layer to the receiving electrode pair. At the detector side, the current in the muscle layer will generate a voltage potential across the transversal muscle and skin impedance, which can be detected on the electrodes.

Figure 3.10 presents the simulation results for variable skin impedances. To account for dry and wet skin, the longitudinal resistances Z_{sl} in the model of Fig. 3.9 are varied. In a second simulation setup, the transversal resistances Z_{st} are increased, such that the respective resistances between the two coupler and between the two detector electrodes increase. The sim-

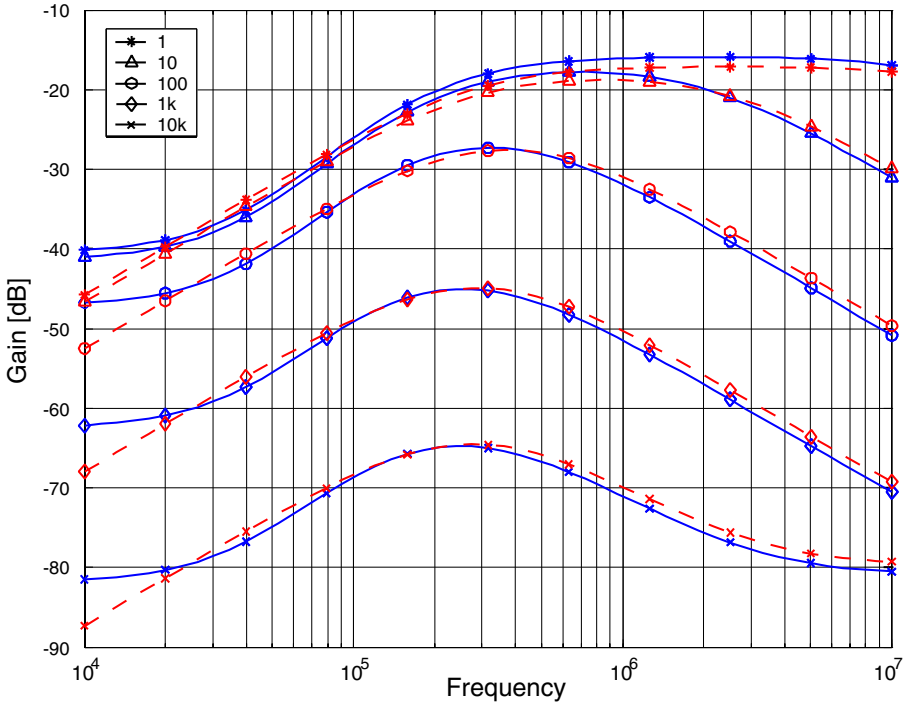

Figure 3.11: Simulation results of layered (solid) and simplified (dashed) tissue model with variance of the coupling resistances Z_c.

ulation results show that a larger longitudinal resistance shifts the corner frequency of a high pass pole to higher frequencies. However, an increase of the transversal resistances emphasizes the low-pass characteristics.

The influence of the coupling resistance is shown in Fig. 3.11. A smaller coupling resistance results in lower attenuation. Minimal attenuation is achieved at 200 kHz. A coupling resistance R_c of 1 kΩ results in an additional attenuation of 25 dB. Furthermore, Fig. 3.11 compares the simulation results of the simple body model (Fig 3.7) with the layered tissue model (Fig. 3.9). The simple model is accurate in the investigated frequency range from 100 kHz to 500 kHz. The layered model shows significantly different behavior in the lower frequency range.

The model developed allows investigation of the most crucial parameters of layered tissue. Nevertheless, the layered model approximates the body as a finite grid of impedances. The complexity will increase with more detailed body structures, e.g., modeling organs and detailed body geometries.

Therefore, numerical simulation models shall be developed to simulate more precise body models.

3.6 Numerical Simulation Models

Injected currents entail a certain potential distribution in the human tissue. This effect has been investigated by finite element (FE) models. FE modeling was successfully used in other applications where currents are injected into the human body, e.g., FES [KK05].

The finite-element method is applied to solve the quasi-static volume conducting boundary problem by the numerical solution of partial differential equations. The mesh of 3D elements and the simulations of the potential distributions were produced with the commercial package EMAG from ANSYS[1].

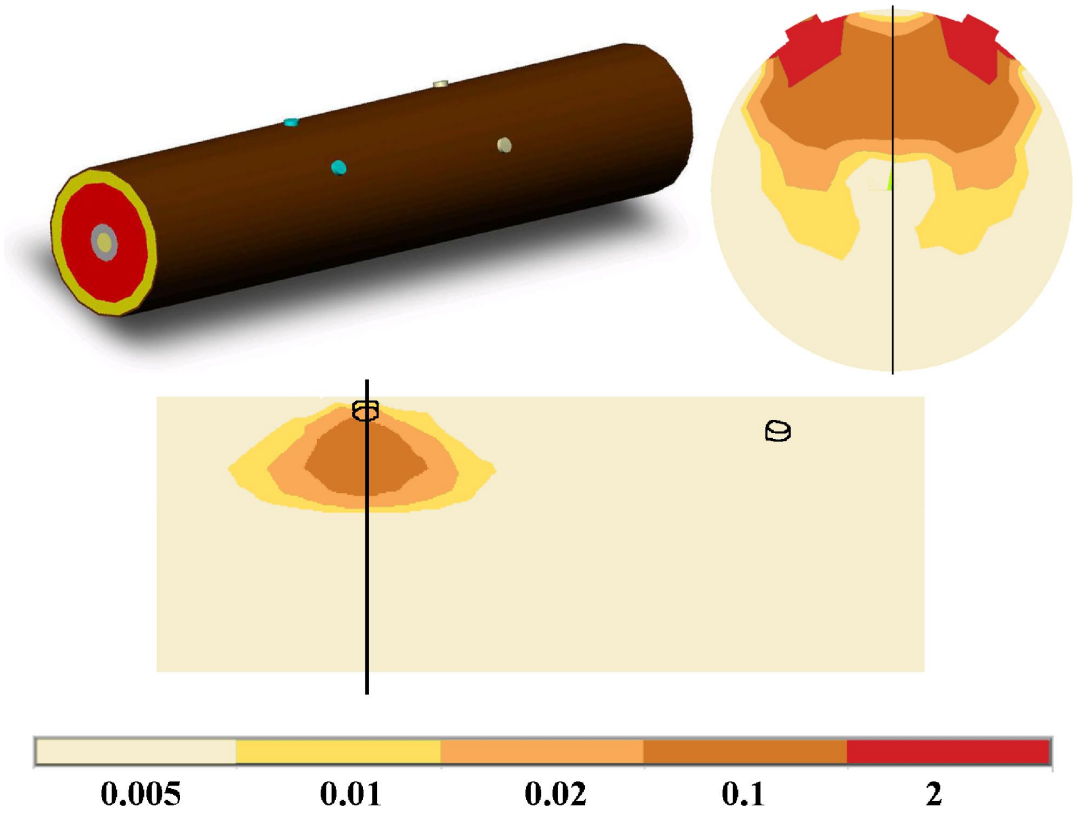

Figure 3.12: The top left picture shows the arm model consisting of multiple layers with the coupler and the detector electrodes. The other two pictures show the current distribution in an axial and a longitudinal cut during data transmission. The black lines indicate the position of the cut.

[1] Electromagnetics Solution EMAG from ANSYS: www.ansys.com

The main interest in developing numerical simulation models was to assess the dependence of the attenuation factor on

- different tissue layer properties,
- joints in between the coupler and detector,
- distance between the coupler and detector,
- size of the coupler and detector electrodes.

3.6.1 Models and Simulation Parameters

Geometry and tissue properties

In order to learn more about the influence of human anatomy on signal propagation, the 3D finite-element model shown in Fig. 3.12 was developed. The geometry of the human upper arm was modeled by concentric cylinders representing the thickness of skin (1.5 mm), fat (8.5 mm), muscle (27.5 mm), cortical bone (6 mm) and bone marrow (6.5 mm; radius) layers. The circular electrodes were modeled by a variable diameter adapted to the area of the electrodes used in the experimental measurements. The spacing was 5 cm for the coupler electrodes and 7 cm for the detector electrodes as shown

Table 3.2: Conductivities of the different tissues at the corresponding frequencies used for the simulations.

Tissue type	Conductivity σ [S/m] 10kHz	100kHz	500kHz	1000kHz
skin dry	2.0E-04	3.5E-04	1.5E-03	7.0E-03
skin wet	3.5E-03	4.0E-02	1.3E-01	2.0E-01
fat	2.7E-02	2.8E-02	4.5E-02	4.5E-02
muscle	3.4E-01	3.9E-01	5.0E-01	6.0E-01
cortical bone	2.0E-02	2.0E-02	2.5E-02	2.5E-02
bone marrow	8.0E-02	8.5E-02	9.0E-02	1.0E-01
electrode	6.0E+07	6.0E+07	6.0E+07	6.0E+07

Table 3.3: Relative permittivities of the different tissues at the corresponding frequencies used for the simulations.

Tissue type	Relative permittivity ε_r 10kHz	100kHz	500kHz	1000kHz
skin dry	1.0E+03	1.0E+03	9.0E+02	8.0E+02
skin wet	3.0E+04	2.0E+04	1.0E+04	3.0E+03
fat	1.0E+03	1.0E+02	4.0E+01	3.0E+01
muscle	3.0E+04	8.0E+03	6.0E+03	2.7E+03
cortical bone	5.5E+02	2.5E+02	2.0E+02	1.6E+02
bone marrow	1.7E+03	5.0E+02	3.5E+02	2.5E+02
electrode	1	1	1	1

in Fig. 2.3. Each tissue layer was described by a conductivity σ and a relative permittivity ε_r. The anisotropy of the muscle conductivity in the longitudinal compared to the transversal direction was assumed to be a factor of three. All other longitudinal tissues were modeled isotropically. The properties used for the different layers are shown in Tab. 3.2 and Tab. 3.3 [GLG96c].

Equation and Stimulus

According to [PH67], inductive effects and wave propagation can be neglected in biological tissues (quasi-static solution). Therefore, the electric and magnetic fields are decoupled. For our application only the electric field is of interest. Maxwell's equations can be simplified using the continuity equation and the constitutive relations, leading to the equation for the quasi-static electric field

$$-\nabla \cdot ([\varepsilon]\nabla V) + \frac{i}{\omega}\nabla \cdot ([\sigma]\nabla V) = 0. \tag{3.9}$$

A current-controlled harmonic waveform stimulus at four frequencies (10 kHz, 100 kHz, 500 kHz, 1 MHz) was used. It was applied between the two coupler electrodes. One of the coupler electrodes acts as a reference with zero potential.

FE Mesh

Mesh sizes were between 150,000 and 200,000 elements. At the boundary between skin and air the normal component of the electric field was set equal to zero, isolating the arm against air. Influences of secondary fields (outer fields) and direct coupling between the electrodes were neglected. The human arm was modeled as a cylinder of finite length. It is known that if the cylinder was too short, errors would be introduced in the simulation. Thus the model was elongated until no significant change of the electrical scalar potential could be found.

3.6.2 Simulation Results

In the following, simulation results are presented showing the influence of the distance between the coupler and detector, the influence of joints, the sensitivity to resistivity changes of the tissue layers, and different coupling by wet, dry and a combined electrode interface. An example of the resulting current density distribution in the arm model is shown in Fig. 3.12. The majority of the current flows between the coupler electrodes in the fat and muscles without penetrating into the bone structure.

Influence of the distance between coupler and detector

Figure 3.13 shows the simulated attenuation of the FE arm model. Three distances of 5, 10 and 15 cm between the coupler and detector electrodes are compared at 10 kHz, 100 kHz, 500 kHz, 1 MHz. Larger attenuation can be expected for increased distances between the coupler and the detector. On the arm model an increase of 5 cm in distance between the coupler and detector leads to an increase of the attenuation by 6 to 9 dB.

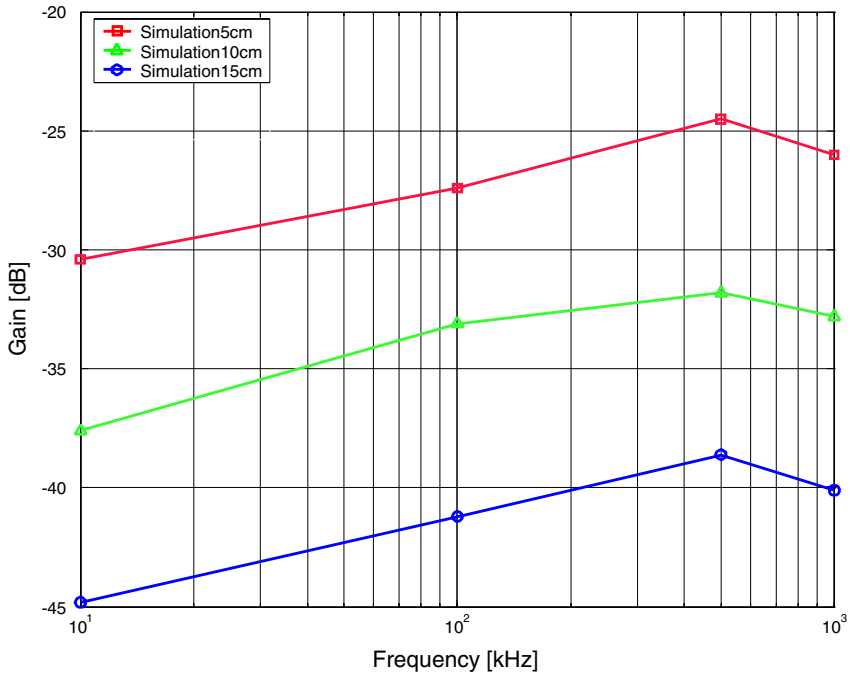

Figure 3.13: Simulated attenuation of the arm model with coupler and detector separated at distances of 5, 10 and 15 cm.

Influence of joints

The influence of joints of different sizes was investigated with the rotationally symmetric model shown in Fig. 3.14. The model was developed such that no re-meshing was needed to investigate different joint sizes. Errors introduced by different meshes would be crucial due to very small potential differences at the detector electrodes. Only the material properties of the volumes in the FE software had to be modified in order to accommodate joints of different sizes. Using the presented model, the influence of the finite element mesh was the same for all configurations tested. Three configurations are shown at the bottom of Fig. 3.14.

Larger joints resulted in higher attenuation factors. The largest joint gave an attenuation of an additional 8 dB compared to the model without a joint.

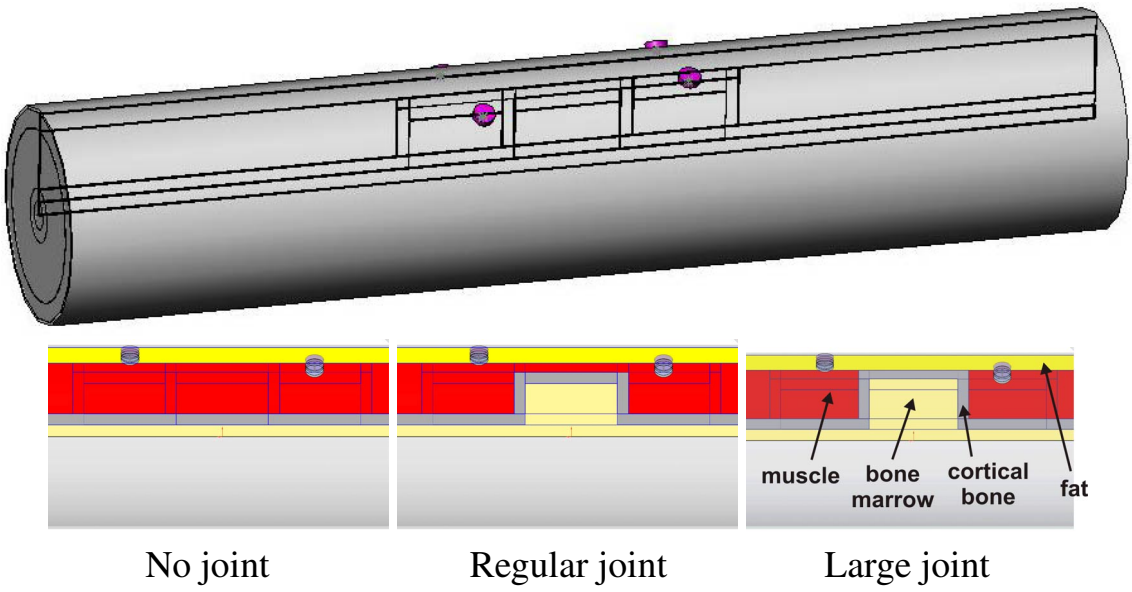

Figure 3.14: Rotationally symmetric model showing different sizes of joints; at the bottom of the picture, cuts through the center of the cylinder are shown, indicating the locations of the different material properties. The largest joint (right) gave an attenuation of an additional 8 dB compared to no joint (left).

Sensitivity to resistivity changes of selected tissues

The sensitivity of the tissue resistivity was investigated by decreasing the resistivity of every tissue layer by a factor of three. Changing the resistivity of the bone and the skin layers (excluding the patch of skin under the electrode) did not influence the attenuation. However, changes in the resistivity of muscle and fat showed an effect on the attenuation between coupler and detector as shown in Fig. 3.15. A decrease of the muscle resistance by a factor of three results in an increase of the attenuation of about 10 dB. This clearly indicates that the muscle tissue short-circuits the current in a way that the current flow is more localized between the two coupler electrodes. Therefore, the potential lines are more concentrated at the coupler and extend less to the detector. A decrease of the fat resistance leads to lower attenuation because a larger fraction of the current is kept in the fat layer and does not penetrate into the muscle layer.

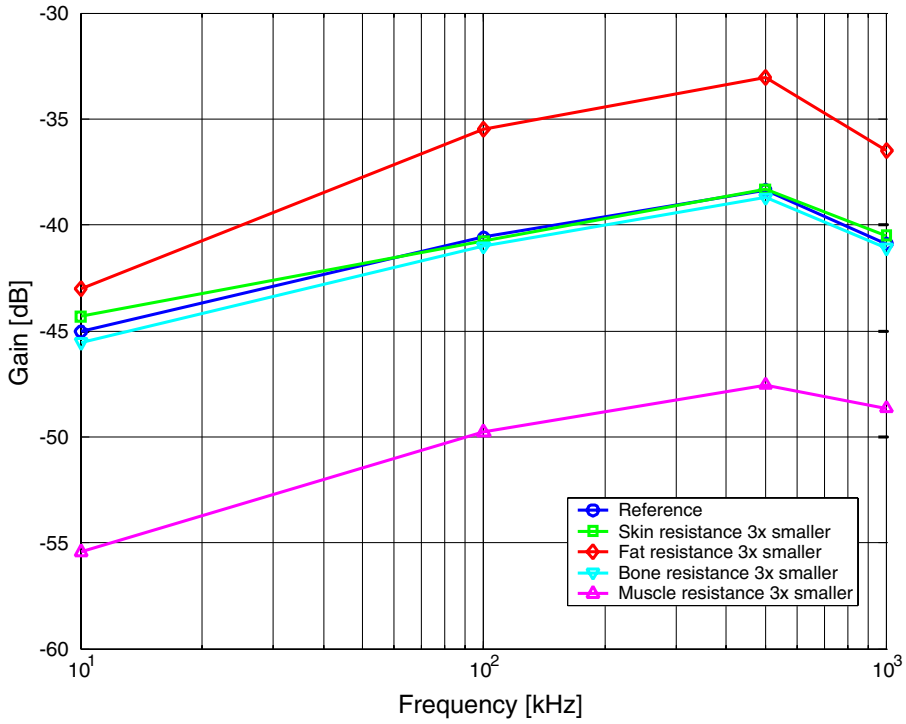

Figure 3.15: The simulation results were obtained by changing the resistance of the different tissue types. It was found that the muscle short-circuits the current and concentrates it at the coupler electrodes due to its low resistance compared with the other tissues.

Wet and dry skin

If a current is applied to the pair of coupler electrodes, the highest voltage drop will be present across the skin compared to the other tissues (muscle, fat, bone). Therefore, the condition of the skin is crucial in respect to transmission performance.

Two simulations were performed assigning the tissue properties of the skin layer with either wet or dry skin. In a third approach, a combined skin layer was used that includes an area underneath the electrodes with the tissue properties of wet skin and the properties of dry skin for the rest of the skin layer. This enabled the simulation of different contact resistances.

The results from the different skin models showed that the attenuation is the lowest for the combined approach (wet and dry skin), because the current induces a smaller voltage for coupling into the arm compared to dry skin.

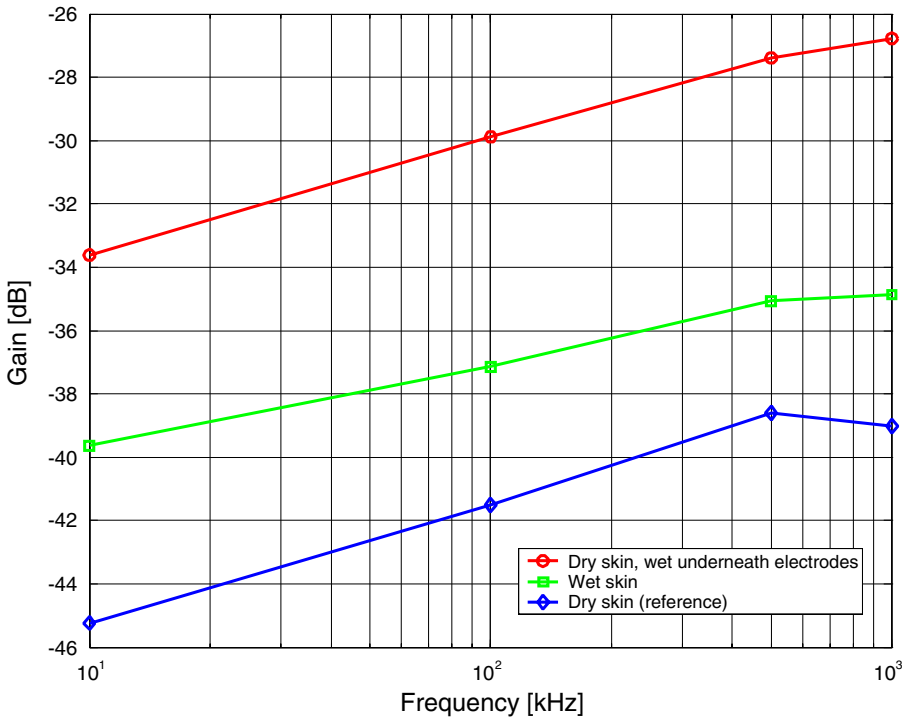

Figure 3.16: Simulation results of different skin conditions: Dry skin, wet skin and combined dry-wet skin layer (with areas underneath the electrodes as wet tissue), allowing comparisons of different contact resistances.

3.7 Results

Models of human tissue have been developed for investigation of the electrical signal transmission characteristics of the body. The signal transmission is based on galvanic coupling which feeds alternating currents into human tissue and detects the resulting potential differences in other body locations. The dielectric properties of several tissues have been collected from the literature. Distinct frequency dependent equations for the relative permittivity and the conductivity were used to develop the equivalent models of cell structures.

- The simple body model developed is a very effective means of understanding and simulating the process of tissue-based coupling. It reduces the complexity down to six body-dependent impedances and four coupling impedances.
- A model of layered tissue is derived by combining discrete elements of dedicated tissue compounds. The most significant layers, e.g., skin, muscle, bone, are represented in the model. Minimal attenuation of the discrete network is detected in the range of 100 kHz to 500 kHz by simulations. Large differences in attenuation have been observed caused by the variation of the coupling electrode impedances.
- Moreover, the finite-element models allow the solution of the potential distributions caused by induced current into the human body. Reasonable results have been presented for an arm model and compared to the previous discrete models. The sensitivity analysis of the different tissue properties indicated that a decrease of the muscle resistance results in an increase of the attenuation. A decrease of the fat resistance leads to a lower attenuation because a larger fraction of the current is kept in the fat layer and does not penetrate the muscle layer.

Attempts to model more complex anatomical structures like joints have been proposed. More detailed tissue structures like internal organs have not been simulated. To investigate the behavior of the entire body, full anatomical models are required. However, the calculation complexity will grow significantly.

The simulations and the simplifications of the presented body models shall be confirmed using *in vivo* measurements.

Chapter 4

Measurement Setup

Investigations with *in vivo* measurements shall confirm the simulation results regarding electrical signal transmission through the human body. The feasibility and the limits of the novel technology can be explored only with a dedicated hardware setup fulfilling the safety guidelines of ICNIRP [Int97]. Enabled by the measurement system developed, the concept of galvanic coupling will be evaluated by measurements and investigations of the coupling variations, and a survey of the specific properties of human body parts will be conducted.

In this chapter, the developed measurement system is presented and used for a feasibility study of galvanic coupling. Section 4.1 defines the system requirements and the main design parameters. The measurement hardware is explained in Sec. 4.2. The results of the initial body measurements and hardware evaluations are presented in Sec. 4.3. Different electrodes are compared at body positions identified as characteristic.

4.1 System Requirements

A measurement system is required for *in vivo* measurements as applied in Fig. 4.1. A coupler unit will generate electrical signals for coupling alternating current by two differential coupler electrodes into the human body. A

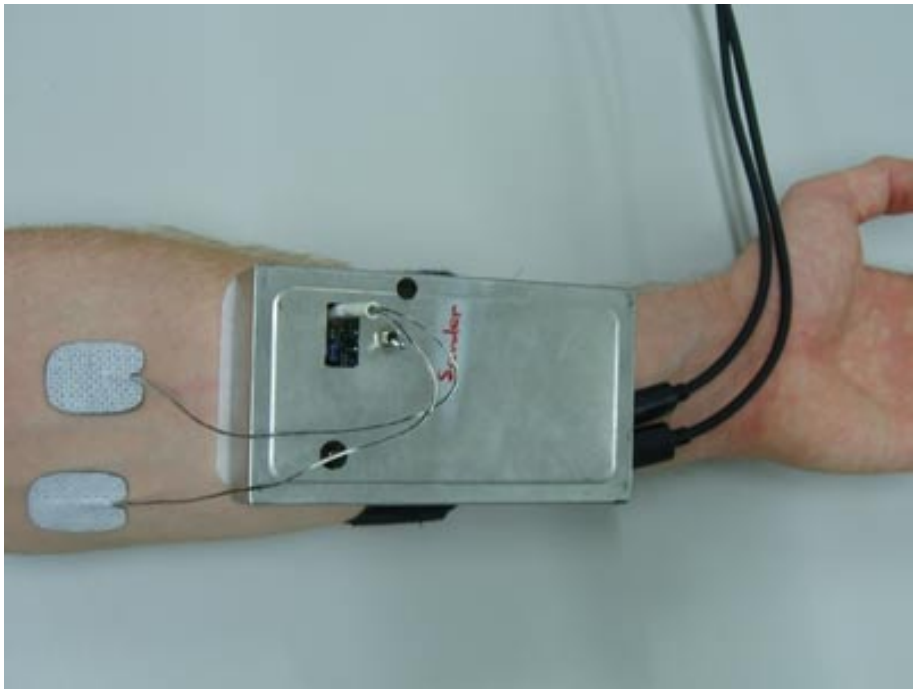

Figure 4.1: Coupler unit attached to the lower arm using fix gel electrodes.

detector unit shall offer amplification and filter circuits for signal detection and recording.

The measurement system shall:

- sweep sinus wave signals of frequencies below 1 MHz,
- measure the channel attenuation between the coupler and detector units,
- transmit and record modulated bit patterns.

The system specifications are listed in Tab. 4.1. In order to fulfill the safety guidelines, a controlled current source with a peak amplitude of 1 mA is specified as the coupler. The models in Chap. 3 have shown minimal body attenuation in the frequency range from 100 kHz to 500 kHz. Therefore, experimental investigation shall be conducted over a range from 10 kHz to 1 MHz. The input dynamic of the detector has to cover channel attenuations between 20 and 90 dB; the detector must therefore sense potentials down to µV. Thus, an amplifier with high input impedance and an adaptive signal attenuation of more than 70 dB is required. The measurement units have to be battery-powered and optically decoupled from other power sources.

4.2 Measurement System Design

Strict medical regulations have to be fulfilled for any system application on a human subject. In order to explore the concept of galvanic coupling, a sophisticated measurement system has been developed and approved by the Swiss National Advisory Commission on Biomedical Ethics NEK-CNE[1].

4.2.1 System Architecture

Figure 4.2 shows the system overview of the measurement setup. The system is composed of two measurement units (coupler and detector board) and an interface board (see Fig. 4.3). The interface board offers a serial optical connection to each of the two measurement units and USB interfaces to standard computers.

The coupler and detector units allow modulated electrical signals to be transmitted and received. Both units have the same digital entities. A Xilinx SPARTAN IIE FPGA provides the signal processing unit and interfaces between the configuration PROM, SRAM for data storage, the analog front end, and the serial links with the interface board.

Table 4.1: Technical specification of the measurement system.

Parameter	Specification
Controlled peak output current	1 mA
Carrier frequency	10 kHz - 1 MHz
Signal waveform	sinus
Demo pattern	OOK, FSK, BPSK modulated
Sampling frequency	8 MHz
Detector gain	20-90 dB
Supply	3.3 V, accumulator
Decoupling	optical (galvanic isolation)

[1] Swiss ethics commission, http://www.nek-cne.ch

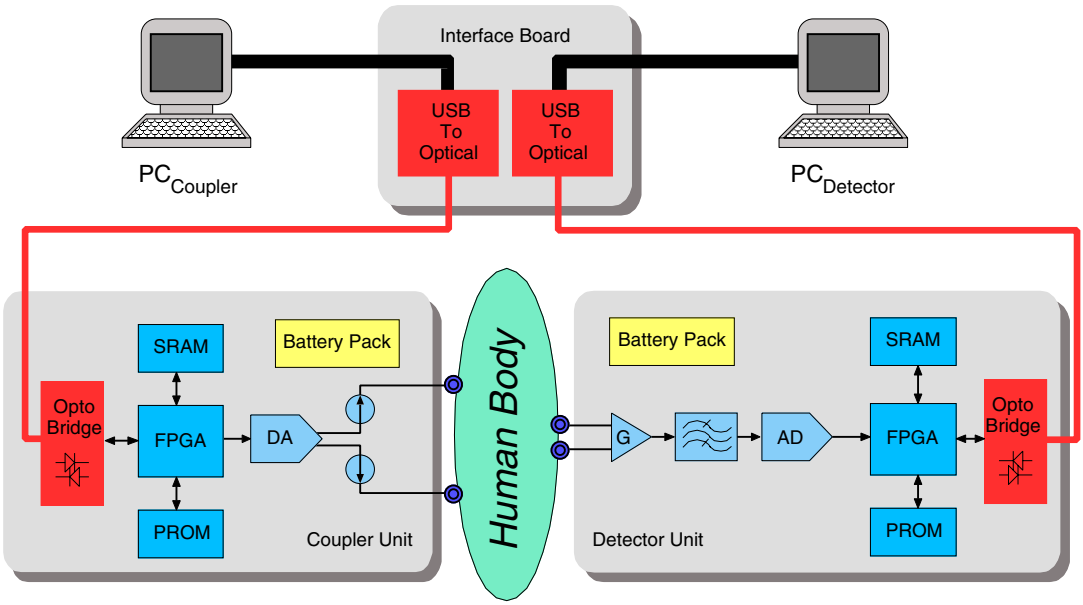

Figure 4.2: Measurement system overview: coupler and detector units are optically connected by the USB interface board to the remote computers.

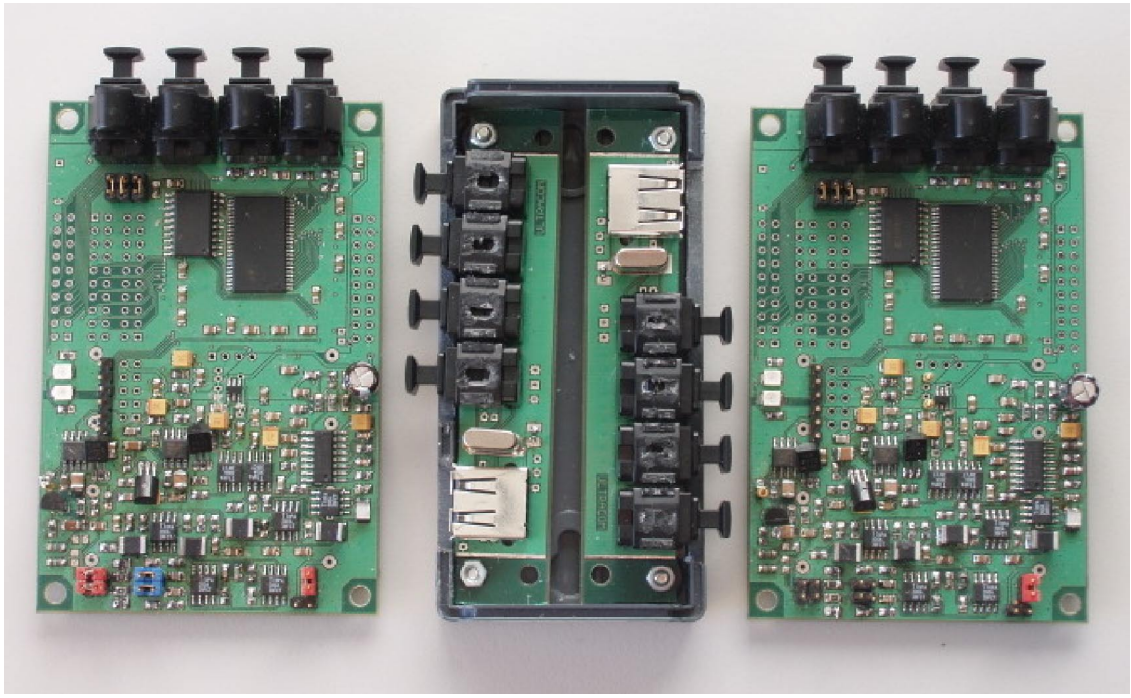

Figure 4.3: Measurement system consisting of coupler, interface and detector PCB (from left to right).

The coupler unit modulates the electrical current-output signals. The signal form is generated by the FPGA and fed through a 12-bit digital-to-analog converter into a differential current-output stage capable of driving a peak amplitude of 1 mA. The coupling of the signal currents into human tissue is performed through two electrodes attached to the skin. The two coupler electrodes operate differentially with opposite peak currents. Two modes have been implemented in the signal generation unit of the FPGA:

- The sweep mode generates sinus signals in the frequency range from 10 kHz to 1 MHz.
- The pattern mode composes bit patterns that are modulated with On-Off-keying (OOK), frequency-shift- keying (FSK) and phase-shift-keying (PSK).

The detector unit amplifies and records the transmitted data. The transmitted signals are differentially picked up by the detector electrodes and amplified up to 72 dB. After band-pass filtering, the signal is digitized by a 14-bit analog-to-digital converter at a sampling rate of 8 MHz. The received data is stored in the SRAM.

The interface board converts the serial data between the optical link to the coupler and the detector units as well as the USB link connected to the remote computers $PC_{Coupler}$ and $PC_{Detector}$. Over these serial data links, the measurement units are configured and the recorded data is transfered from the SRAM to the remote computers. The remote computers initialize the measurement units, the $PC_{Coupler}$ starts the measurement and the $PC_{Detector}$ collects the data for post processing. The basic functionality on the remote computers is implemented in *Perl* using *win32api* libraries.

Both the coupler and detector units are battery powered and fully isolated by the serial optical links. Therefore, the units are electrically decoupled from any power lines and they operate far below safety limits.

4.2.2 Electrode Types

The envisioned application requires flat and self-adhesive electrodes with low contact resistance. The electrodes shall be easy to use, comfortable to wear, and not trigger any skin reaction. These requirements are of tremendous importance in long-term and neonatology monitoring applications. Electrodes for ECG recording were found to be most suitable.

Based on a survey of available medical electrodes and electrode technologies, the following products were selected for further investigation (Table 4.2, Fig. 4.4):

1. *Swaromed REF1008* ECG electrodes are pre-gelled (liquid gel), single-use, and have a silver/silver-chloride contact. These are the most commonly used ECG electrodes.

2. *Neuroline 715* electrodes feature a high-quality silver/silver chloride contact. The electrode is coated with a skin-friendly solid gel that allows repositioning several times without losing adhesive power. The transparent electrode area enables very precise location of the application position.

3. *Blue Sensor BR* electrodes feature a skin-friendly solid gel that allows the electrode to be repositioned if necessary. Due to the cloth backing material, the skin is able to breathe, such that the electrode remains comfortable to wear over long periods.

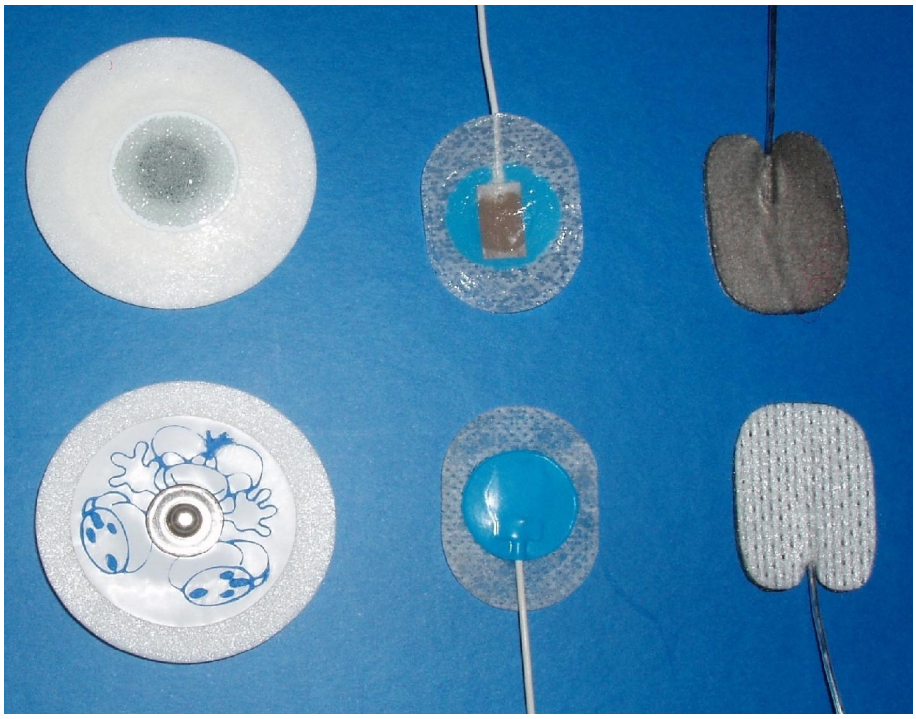

Figure 4.4: *Swaromed REF1008* (1), *Neuroline 715* (2), *Blue Sensor BR* (3).

Table 4.2: Electrode properties comparing size and type of *Swaromed, Neuroline* and *Blue Sensor* electrodes.

Type	Active Area	Contact
Swaromed REF1008	80 mm^2	pre-gelled
Neuroline 715	54 mm^2	solid-gel
Blue Sensor BR	560 mm^2	solid-gel

4.3 Feasibility Measurements

The measurement system was used for investigation of the transmission and coupling characteristics among a small group of subjects in a feasibility study.

The study investigated

- the feasibility of the novel transmission technology,
- the characterization of different electrode types and the influences of size variations,
- the development of a test procedure for a clinical trial with a larger number of subjects.

4.3.1 Test Strategy

In the feasibility study various differences between measurements on the extremity and thorax were identified. Based on these results, the two setups

Table 4.3: Preliminary evaluation on 1 subject: Characteristic body points for coupling comparison.

Session	Coupler	Detector
Upper arm	B1 (elbow)	B2 (axillary)
Thorax	C1 (right)	E1 (left)

shown in Fig. 4.5 on the upper arm (from elbow *B1* to axillary *B2*) and on the thorax (from right *C1* to left body side *E1*) were chosen for comparison of the various coupling strategies (Table 4.3). The measurement units were attached to the human body as shown in Fig. 4.1. Both coupler electrodes were attached with 5 cm spacing while the detector electrodes were separated by 7 cm or less, depending on the body geometry.

The following test strategy has been defined in order to investigate the coupling characteristics of the different electrodes at significant locations:

- Three variations of the electrode size and three different electrode types for both the coupler and detector units
- Measurement of the coupling impedance of the channel (induced signal current of 1 mA)
- Assessment of signal attenuation over frequency by sweeping a sinusoidal signal from 10 kHz to 1 MHz

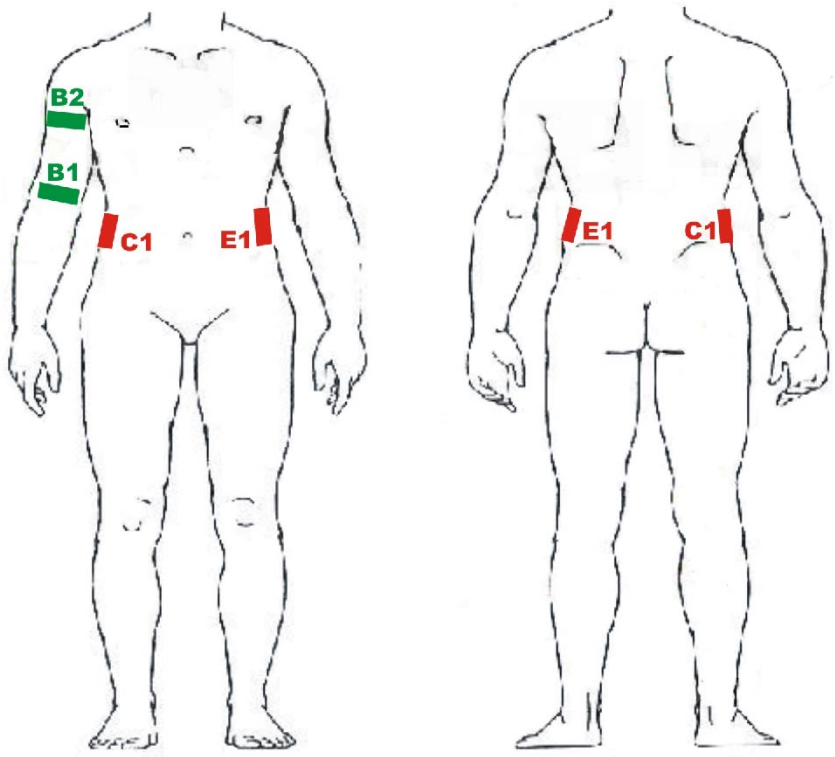

Figure 4.5: Measurement point distribution in the feasibility study.

4.3.2 Electrode Comparison

Figure 4.6 shows the measured results of all three electrode types. The *Blue Sensor* and *Swaromed* electrodes show rather similar attenuation in both setups. *Swaromed* electrodes on the upper arm result in the absolute lowest attenuation. The *Neuroline* electrodes exhibit the highest attenuation. When taking the much smaller contact areas into account, however, the *Neuroline* electrode is competitive with the *Blue Sensor*.

In Tables 4.4 and 4.5, the measured impedances (mean and standard deviations of five samples) of the three electrode types are compared for three locations. *Direct* indicates measurements with two electrodes pasted together. *B1* and *C1* give the impedance measurements at the locations on the upper arm and on the thorax. The measurements were performed at 100 kHz and 1 MHz.

As expected, the body input impedance is in the range of a few hundred Ohms. In the case of the *Neuroline* at 1 MHz, the electrode resistance is in

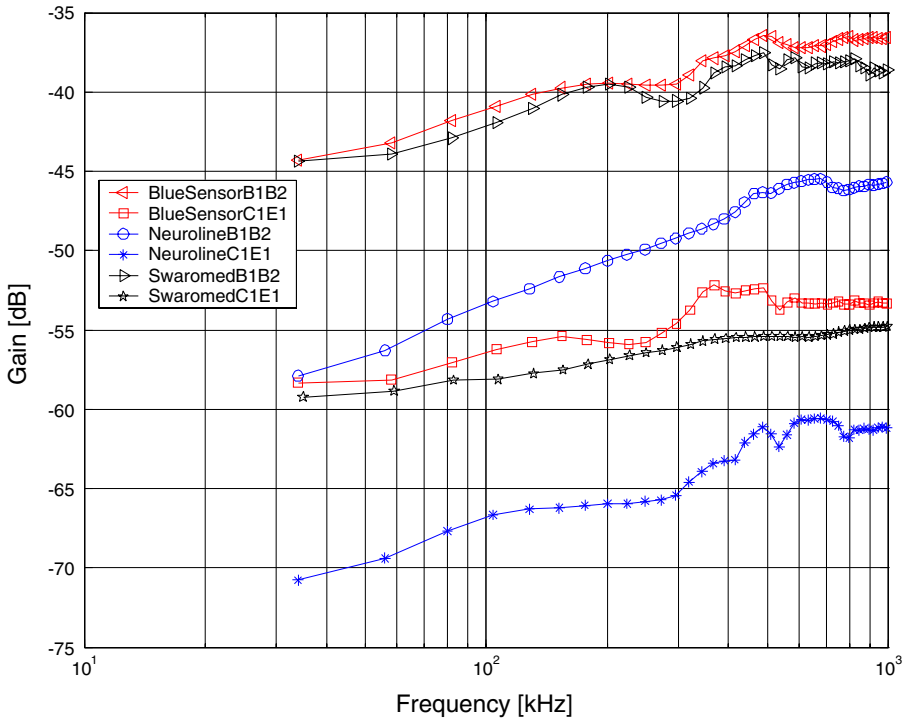

Figure 4.6: Attenuation of different electrodes compared at body points on the upper arm *B1* to *B2* and on the thorax *C1* to *E1*.

Table 4.4: Measured electrode characteristics of 5 samples: *Swaromed, Neuroline* and *Blue Sensor* electrodes at 100 kHz based on the equivalent circuit of Fig. 3.8 with R_c and C_c measured directly connected and at body locations on the upper arm *B1* and on the thorax *C1*.

Location	Type	Mean		Standard Deviation	
		R_c	C_c	R_c	C_c
Direct	Swaromed	21Ω	2.85nF	5.4Ω	1.1nF
	Neuroline	359Ω	418pF	7.1Ω	66pF
	Blue Sensor	203Ω	28pF	16.1Ω	6pF
B1	Swaromed	279 Ω	2.5nF	16Ω	0.3nF
	Neuroline	1.2 kΩ	852pF	90Ω	79pF
	Blue Sensor	340Ω	1.85nF	10Ω	0.4nF
C1	Swaromed	363 Ω	1.7nF	36Ω	0.4nF
	Neuroline	1.71 kΩ	600pF	190Ω	29pF
	Blue Sensor	447Ω	2.4nF	40Ω	0.7nF

Table 4.5: Measured electrode characteristics of 5 samples: *Swaromed, Neuroline* and *Blue Sensor* electrodes at 1 MHz based on the equivalent circuit of Fig. 3.8 with R_c and C_c measured directly connected and at body locations on the upper arm *B1* and on the thorax *C1*.

Location	Type	Mean		Standard Deviation	
		R_c	C_c	R_c	C_c
Direct	Swaromed	19Ω	10pF	3.6Ω	9pF
	Neuroline	370Ω	60pF	9Ω	15pF
	Blue Sensor	195Ω	21pF	15Ω	5pF
B1	Swaromed	201Ω	73pF	55Ω	20pF
	Neuroline	559Ω	88pF	39Ω	4pF
	Blue Sensor	247Ω	34pF	21Ω	14pF
C1	Swaromed	245Ω	31pF	39Ω	4pF
	Neuroline	768Ω	63pF	39Ω	4pF
	Blue Sensor	263Ω	40pF	32Ω	19pF

Table 4.6: *Blue Sensor* electrode characteristics based on the equivalent circuit of Fig. 3.8 with R_c and C_c depending on the size of their active area at frequencies of 100 kHz and 1 MHz applied directly connected and at body locations on the upper arm *B1* and on the thorax *C1*.

Location	Frequency	Size 1		Size $\frac{1}{2}$		Size $\frac{1}{4}$	
		R_c	C_c	R_c	C_c	R_c	C_c
Direct	100k	203 Ω	28 pF	700 Ω	11 pF	850 Ω	8 pF
Direct	1M	195 Ω	21 pF	600 Ω	8 pF	700 Ω	6 pF
B1	100k	340 Ω	1.85 nF	1.1 kΩ	400 pF	1.5 kΩ	320 pF
B1	1M	247 Ω	34 pF	900 Ω	6 pF	1.1 kΩ	2 pF
C1	100k	447 Ω	2.4 nF	1.05 kΩ	500 pF	1.8 kΩ	530 pF
C1	1M	263 Ω	40 pF	910 Ω	8 pF	1.3 kΩ	2 pF

the range of the body resistance of approximately 200 Ω. *Swaromed* electrodes feature a significantly lower impedance. At 100 kHz the body resistance is significantly higher with more than 300 Ω.

Both the electrode impedance and the electrode-skin impedance can increase up to the kΩ range. This causes a huge undesired loss as seen in Fig. 4.6. Therefore, the electrode impedances have to be minimized.

In addition, different sizes of *Blue Sensor* electrodes have been compared. The active area was cut into one half and one quarter of the original size. The measured impedance values are shown in Table 4.6. The smaller the size of the electrode, the larger is the resistance and the smaller is the capacitance of the electrode. Thus, larger electrodes improve the transmission characteristics. However, for the envisioned application and a further miniaturization, a trade-off has to be found.

4.4 Results

The measurement platform presented here offers versatile possibilities for signal application and data transmission experiments through the human body. In the feasibility measurements, alternating current was coupled by an electrode pair in the frequency range from 10 kHz to 1 MHz.

Data patterns modulated by FSK and BPSK have been transmitted with a carrier frequency of 600 kHz. The demodulation was carried out off-line on the remote computer. An error-free transmission of 32 bit patterns with FSK modulation was realized down to a frequency shift of 16 kHz and up to a bit rate of 128 kbit/s. The BPSK modulated data allowed a bit rate of 256 kbit/s.

The attenuation was calculated according to Eq.3.1. The channel performance is characterized by the signal-to-noise ratio (SNR) as defined in accordance with Shannon [Sha48] as the ratio between the total transmitted power and the noise power according to

$$SNR = \frac{P_{signal}}{P_{noise}}. \tag{4.1}$$

The channel capacity is defined according to Shannon by the signal bandwidth (BW) and the SNR as

$$C = BW \cdot \log_2 (1 + SNR). \tag{4.2}$$

The parameters for the measurements on the upper arm and the thorax are indicated in Tab. 4.7. The feasibility measurements have shown that the

Table 4.7: Measured attenuation at 200 kHz and achieved SNR for the estimation of the channel capacity on the upper arm and through the thorax with a signal bandwidth of 100 kHz.

	Attenuation [dB]	SNR [dB]	Channel capacity [Mbit/s]
Upper arm (B1B2)	40	37.0	1.23
Thorax (C1E1)	56	26.3	0.87

novel technology has the potential to transmit data through the human body by galvanic coupling. The signal attenuation is highly dependent on the coupling electrodes and the application location.

- The upper arm has been identified as the body part with the best performance. This short-range transmission features a low attenuation of 40 dB, high SNR of 37 dB, and a high resulting channel capacity of 1.23 Mbit/s. The upper arm will serve as the starting point for the comparison of measurements with numerical models due to its simple structure with a central bone and cylindrical tissue structures.
- The thorax showed stable attenuation independent of the location. Compared with the upper arm, higher attenuation and lower SNR was measured. However, the larger geometry of the thorax will allow advanced experiments, e.g., the orientation and the separation of the coupler and detector electrodes.

Using Swaromed REF1008, Neuroline 715, and Blue Sensor BR, different electrodes were compared.

- Electrodes with lower resistance led to lower attenuation and therefore feature longer transmission.
- Pre-gelled *Swaromed* electrodes feature lower coupling resistance compared to solid-gel electrodes, e.g., *Neuroline*.
- Solid-gel electrodes with lower capacitive values are superior to the pre-gelled electrodes.

Due to the fact that the *Swaromed* electrodes are prevalent ECG electrodes, they were accepted for the clinical trial. The *Blue Sensor* electrodes have almost the same performance but have not previously been not used in medical applications.

The findings shall be confirmed and extended further among a set of subjects by applying the system in a clinical trial to investigate individual variations and additional body regions.

Chapter 5

Clinical Trial

The feasibility measurements have shown the possibility of using the human body as a transmission medium of electrical current. Investigations on the dielectric properties of the human tissue layers and equivalent circuit models have given an initial understanding of the coupling principles and approximated the flow of electrical current through the human body.

In vivo measurements allow investigations on individual specific variations among subjects, the characterization of dedicated body parts, and verification of the developed simulation models. The methods of the clinical trial consist of medical, physiological, and electrical examinations. A significant range of subjects will be explored in order to obtain results for a meaningful characterization. Direct comparisons with the numerical simulations of the finite-element models will strengthen the understanding of the channel properties, the current distribution, the sensitivity of the tissue properties, and the influences of the electrode size and contact condition in respect to signal attenuation and distortion. Derived from the measurement results, conclusions for the development of intra-body communication transceivers shall be drawn.

The experimental methods used in the clinical trial are presented in 5.1. The measurements results are presented in Sec. 5.2. Comparisons with FE models are discussed in Sec. 5.3

5.1 Experimental Methods

In the clinical trial, the subjects have been examined using:

- regular medical examinations
- bioelectrical impedance analysis
- the measurement setup for investigations on galvanic coupling

5.1.1 Medical Examinations

The study has been conducted with 20 subjects. The average age was 47.2 years and the standard deviation 22.1 years. Half of the group was composed of male respectively female subjects. The trial was approved by the *Swiss National Advisory Commission on Biomedical Ethics NEK-CNE*. The study is defined as a security and efficiency discussion. Twenty people were chosen as the subjects of the trial. Ten subjects were termed to be healthy, while the other ten subjects have been patients with a recent heart attack incidence. The subjects were under medical observation during the entire investigation [LH04].

The subjects were examined and several of their physiological parameter were recorded. Table 5.1 lists the physical characteristics of the subjects.

The *body mass index (BMI)* is a variable based on weight in relation to body height

$$BMI[\mathrm{kg/m^2}] = \frac{Weight\ [\mathrm{kg}]}{(Body\ height\ [\mathrm{m}])^2} \tag{5.1}$$

The *waist-to-hip ratio (WHR)* is a medical indicator of the fat distribution in the torso

$$WHR = \frac{Waist\ circumference}{Hip\ circumference} \tag{5.2}$$

The *subscapular skin fold thickness* is a measurement quantity for the subcutaneous fat layer at the torso, while the *triceps skin fold thickness* denominates the thickness of the fat layer at the extremities.

Table 5.1 summarizes the physical parameters of the subjects included in the study. The variations in the BMI, the WHR, and the skin properties indicate

Table 5.1: Physical characteristics of all subjects.

	Min	Max	Average	Deviation
Body height [cm]	146	194	168.44	12.28
Weight [kg]	45.5	103	69.20	14.69
Body mass index BMI	19.29	29.69	24.21	3.31
Hip circumference [cm]	87.5	110	99.30	5.85
Waist [cm]	63	105.5	85.40	14.66
Waist-to-Hip Ratio	0.66	1.00	0.85	0.11
Body temperature while resting	34.9	37.1	36.03	0.57
ΔT body/room	9.9	16.3	13.21	1.67
ΔT rest/activity	-0.7	1.5	0.39	0.50
Chest measurement [cm]	79	112	95.68	10.13
Upper arm [cm]	25	39	29.38	3.78
Lower arm [cm]	19	31	25.28	3.07
Acromion - wrist	49	63	56.23	4.02
Thigh [cm]	47	63	54.63	3.96
Lower leg [cm]	33	41.5	36.68	2.30
Trochanter major - Malleolus	75	91.5	82.58	5.15
Skin fold thickness				
Subscapular [mm]	7	29.5	16.22	6.35
Triceps [mm]	2	13.5	4.93	2.86

that a reasonable range of different subjects was chosen. In a later section, these data will serve for the analysis of the physical impacts on the signal transmission.

The medical records of cardiovascular activity and body activity confirm that no abnormality was discovered among the subjects as shown in Tab. 5.2. The parameters of blood pressure, body temperature and environmental conditions were monitored and kept within a regular range across all measurements with subjects at rest, on the treadmill and during control measurements.

For comparable results, it was our goal to keep the variations of temperature, humidity, and exercise condition as constant as possible over all the entire period of the study.

Table 5.2: Dynamic medical characteristics of all subjects.

	Min	Max	Average	Deviation
Cardiovascular rest				
systolic [mmHg]	100	183	130.55	21.32
diastolic [mmHg]	50	90	74.20	10.99
Puls [ppm]	47	92	64.40	10.18
Cardiovascular activity				
systolic [mmHg]	125	185	156.58	17.39
diastolic [mmHg]	40	92	69.26	15.74
Puls [ppm]	60	148	89.47	19.19
Body temperature [T]	34.2	36.9	35.77	0.80
Treadmill activity [W]	35.0	225.0	99.74	53.73
Rounds per minute [rpm]	54	100	72.32	11.65
Duration [sec]	120	600	518.95	144.76
Room temperature	20.1	25.6	22.90	1.39
Humidity [%]	20	27	22.35	1.73
Air pressure [hPa]	1076	1095	1088.15	5.72

5.1.2 Bioelectrical Impedance Analysis

The dielectric properties of human tissue have been analyzed and parameterized based on the experimental findings in Chap. 3. To compare the numerical simulations and the measurements in the clinical trial, it is essential to accurately determine the biological constitution of the subjects' whole-body tissue properties. A method widely used in medicine for measuring whole-body parameters is the bioelectrical impedance analysis BIA.

Thomasset [Tho62, Tho63] conducted the original studies using electrical impedance measurements over two subcutaneous-inserted needles as an index of total body water (TBW). Hoffer *et al.* [HMS69] and Nyboer [Nyb70] first introduced the four-electrode bioelectrical impedance measurements (BIA) technique. This bioelectrical impedance spectroscopy measures the total body impedance Z at frequencies from 5 kHz to 1,000 kHz. This technique has enabled the measurement of the extra-cellular water (ECW) and intra-cellular water (ICW) distributions.

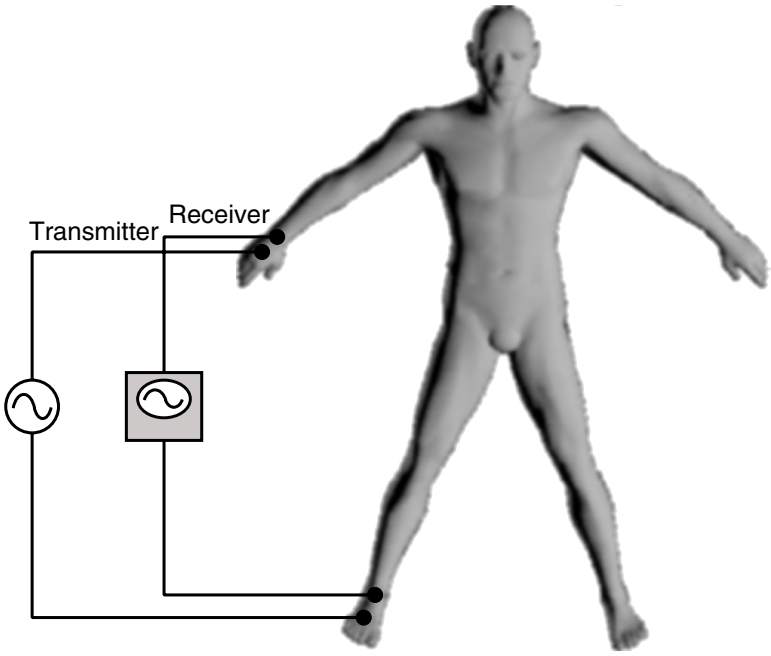

Figure 5.1: Standard placement of electrodes on hand/wrist and foot/ankle for tetrapolar bioelectrical impedance analysis BIA.

Modern BIA involves total body measurements from hand to foot with a setup as depicted in Fig 5.1. The source electrodes introduce an alternating current at the base of the toes and fingers. The applied frequency range is between 50 kHz and 100 kHz. The RMS current value is between 0.5 mA and 4 mA. The detecting electrodes measure the voltage drop at ankle and wrist.

Figure 5.2 shows the most frequently used model for total body impedance.

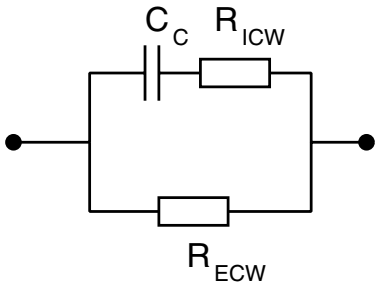

Figure 5.2: Human body representation in BIA: The human body is simplified into inter-cellular water and extra-cellular water separated by cell membranes in order to represent the total body impedance with an inter-cellular resistance R_{ICW}, extra-cellular resistance R_{ECW}, and cell capacitance C_C.

The circuit represents the biological tissues as extra-cellular fluid R_{ECW} in parallel to the branch of intra-cellular fluid R_{ICW} and the cell membrane component C_c.

Figure 5.3 illustrates the variation of the total body impedance over the frequency:

- At zero (or low) frequency, the current does not penetrate the cell membrane, which acts as an insulator, and therefore the current passes through the extra-cellular water (ECW), which is responsible for the measured resistance of the body $Z_{f=0}$.
- At infinite frequency (or very high frequency) the capacitor behaves as a perfect (or near perfect) capacitance, and therefore the total body resistance $Z_{f=\infty}$ reflects the combined intra-cellular (ICW) and extra-cellular water (ECW), together representing the total body water (TBW).

Medicine uses bioelectrical impedance measurement (BIA) for estimating the body composition. Of particular interest is the estimation of the body fat distribution [Kyl04]. Actually BIA determines the electrical impedance of body tissues, which provides an estimate of the total body water TBW. This amount can be used to estimate the fat-free body mass and body fat. Further goals seek additional properties of human tissue through measurable parameters.

In order to characterize the subject's body condition, the BIA results of each subject were recorded and compared with the results of the attenuation measurements (see Tab. 5.5 on page 77).

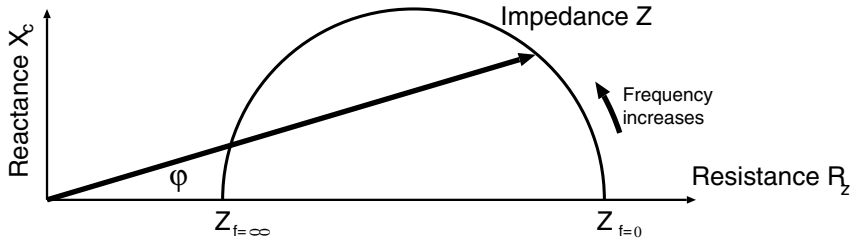

Figure 5.3: Diagram of the graphical derivation of the phase angle; its relationship with resistance (R_z), reactance (X_c), impedance (Z) and the frequency of the applied current.

5.1.3 Measurements with the Dedicated Measurement Setup

In order to assess the characteristics of different paths (extremities, thorax, joints), the following test protocol has been defined:

- Coupler and detector locations according to Tab. 5.3
- Assessment of the signal attenuation over the frequency by sweeping a sinusoidal signal
- Measurements under body activity and during ECG recording

The coupler electrodes were attached at a distance of 5 cm, while the detector electrodes were separated by 7 cm, or closer, depending on the body geometry. Since the measurements were restricted to 3 hours per patient, it was necessary to limit the number of different locations for transmission measurements. Figure 5.4 shows the locations and Table 5.3 indicates the combinations of coupler and detector points. The measurements were grouped into the four sessions along the arm, through the thorax, along the leg, and through the entire body. The index *geometrical* indicates a wider

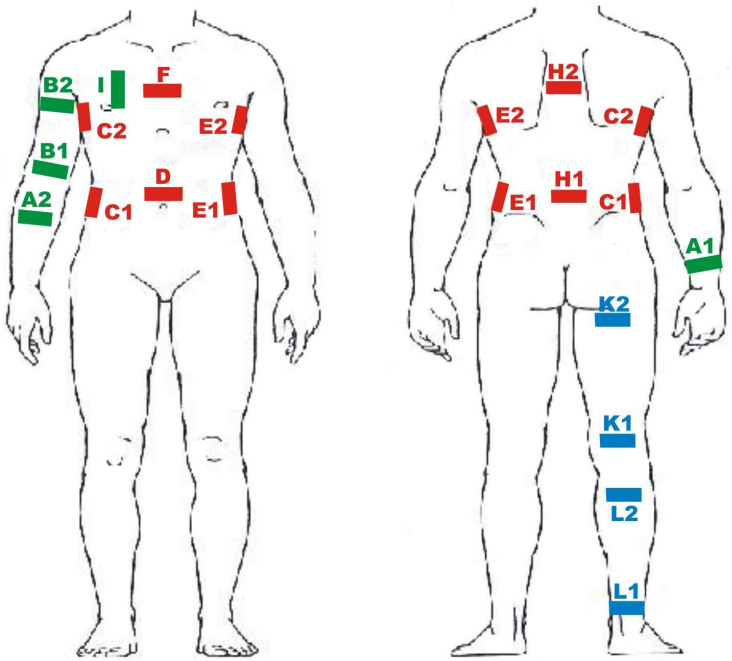

Figure 5.4: Measurement point distribution over the entire body.

Table 5.3: Body points and session configurations.

Session	Coupler	Detector
Arm	A1	A2, B1, $A2_{Ergo}$
	A2	B1, B2
	B1	B2, I
	B2	I
Thorax	C1	E1
	C2	E2
	D	H1
	F	D, D_v, H1, H2
	F	$H2_{ecg}$, $H2_{Ergo}$
Leg	L1	L2, K1
	L2	K1, K2
	K1	K2, H1
	K2	H1
Path	F	L1, K2, A1
	H2	F, D_v
	A1, H2, L1, K2	$D_{geometrical}$

separation of the detector electrodes. In this case, the electrodes were placed at diametric sides of the thorax. Furthermore, index v implies a rotation of the two electrodes by 90 degrees.

In separate sessions, measurements during treadmill exposure (index *Ergo*) and during ECG measurement (index *ecg*) were processed.

For the *Ergo* meter measurements the subject was asked to warm up for 5 minutes on a treadmill and to exercise during the measurement recording. Results of the treadmill exposure are presented in Fig. 5.11.

During ECG recordings the measurement system was active and no visual effects on the subjects' ECG were observable.

5.2 Measurement Results

The measurements obtained in the clinical trial have been compared with the numerical simulations. The upper arm allows direct comparison with the cylindrical simulation model. The dependencies have been explored based on distance, skin condition, electrode size, and joints. Furthermore, relations between the body parameters of each subject and the signal transmission have been analyzed. The measurement results show the behavior of further body regions.

5.2.1 Comparison on the Upper and Lower Arm

The recorded signals in the coupler and detector units are used for attenuation calculation according to Eq. 3.1.

Along the arm the attenuation and characteristics of transmitted signals change depending on location as shown in Fig. 5.5. The lower arm *A1A2*

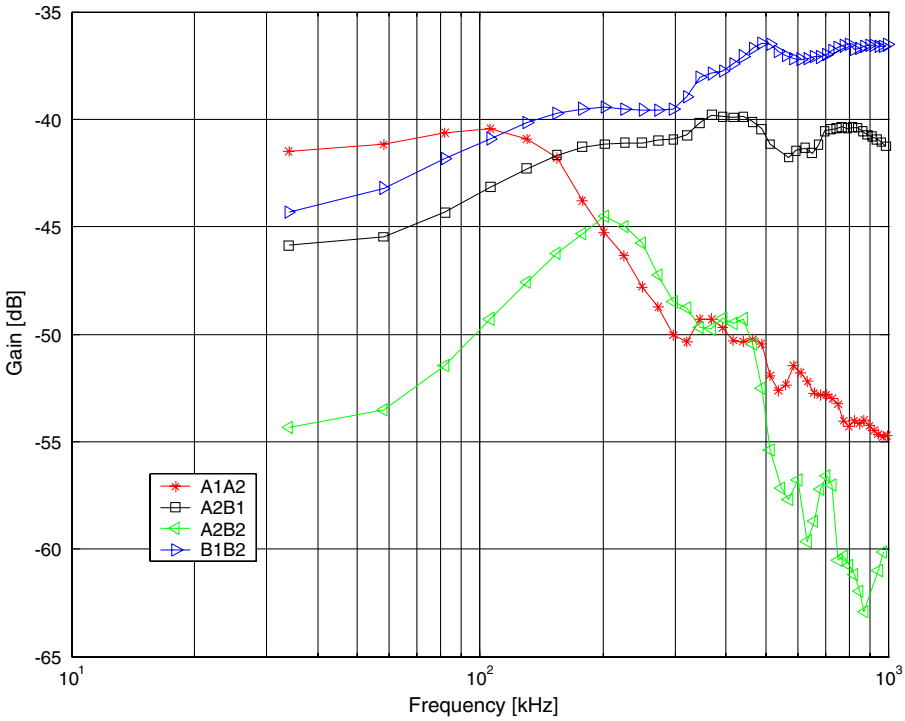

Figure 5.5: Attenuation in arm measurements: Lower arm (*A1A2*), through elbow joint (*A2B1*), upper arm (*B1B2*), and from lower arm to axillary (*A2B2*).

acts as a stronger low pass filter than the upper arm *B1B2*. The attenuation over joints *A2B1* increases by an additional 3 dB. The low-pass characteristic between *A1A2* differs from all other locations. Although this setup is comparable in distance and coupling with several other locations, the lower arm requires a fully different reference model. This effect has not been confirmed by simulations.

Figure 5.6 shows the average attenuation and standard deviation among all patients with coupler location *B1* and detector *B2*. This configuration represents a short-range communication path along the extremities. The measurements confirm the wide range of measured attenuation. Such variations are caused by various factors such as the patient's muscle, fat and bone distribution. In addition, the variations are increased by temporal and local effects. A small displacement of the electrodes causes significant differences due to inhomogeneity and temporal alteration of the human body and the skin condition.

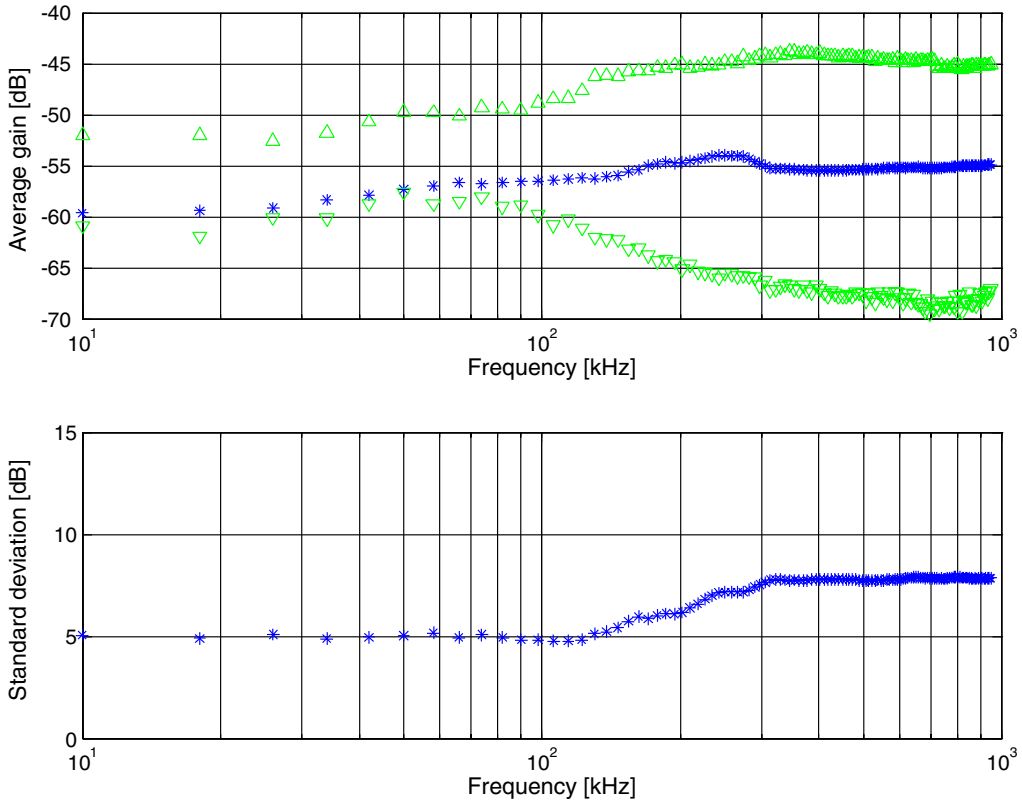

Figure 5.6: Attenuation between arm locations *B1* and *B2*, averaged over all patients, and range with minimum ▽ and maximum △ measurements

5.2.2 Dependency on Distance and Electrode Parameters

Figures 5.7 and 5.8 show the measured attenuation between the coupler to the detector depending on distance and electrode size. The measurements are compared with the numerical simulation results of Sec.3.6.

Influence of the distance between coupler and detector

Figure 5.7 shows the measured and simulated attenuation for distances between the coupler and detector electrodes of 5 cm, 10 cm, and 15 cm. With increasing distance, attenuation grows. With the arm model an increase of 5 cm in distance between coupler and detector leads to an extra attenuation of 6 to 9 dB.

For this setup, the numerical simulations compare well with the experiments. Therefore, the approximation using a cylindrical model with mul-

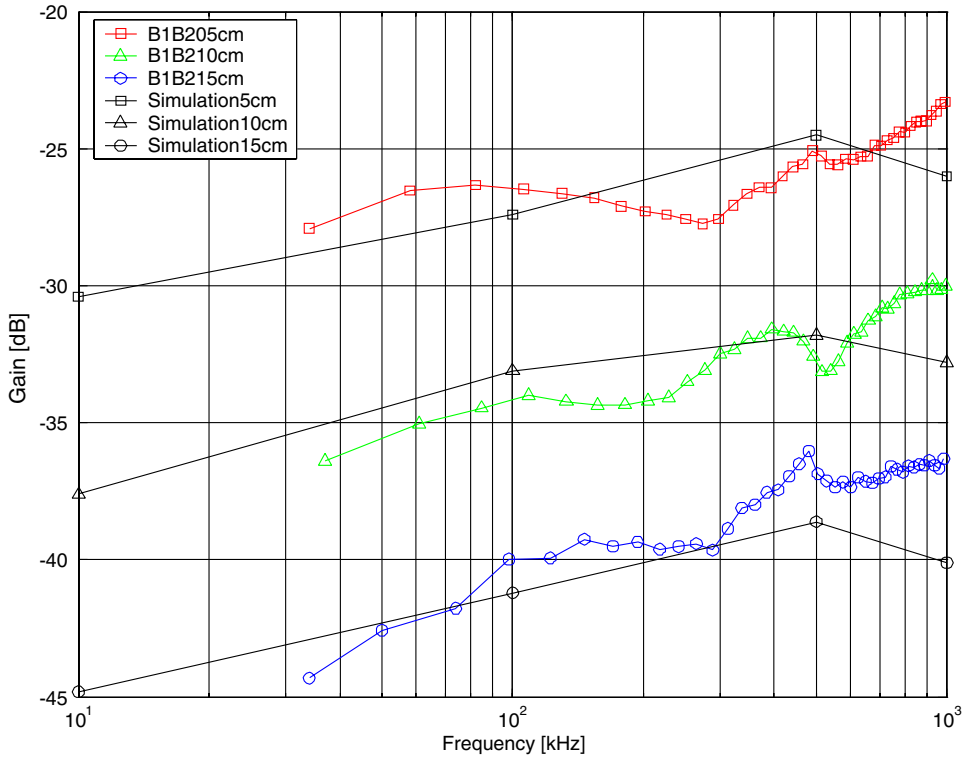

Figure 5.7: Attenuation at upper arm in measurements and simulations with coupler and detector separated at distances of 5, 10 and 15 cm.

tiple layers is indeed adequate. A more detailed geometry with complex layer structures would not significantly improve the results.

Influence of the electrode size

In Fig. 5.8, the attenuation measurements with combinations of different coupler and detector electrode sizes are shown. The size of the detector electrodes has a negligible impact (results with index *44* compared to *41*) whereas the attenuation decreases with an increase in size of the coupler electrodes (*41*, *21* down to *11*).

The influence of the coupler electrodes has been confirmed in the finite-element model simulations as shown in Fig. 5.8. A doubling in size of the coupler electrodes caused a lower attenuation of 6 dB in the simulations.

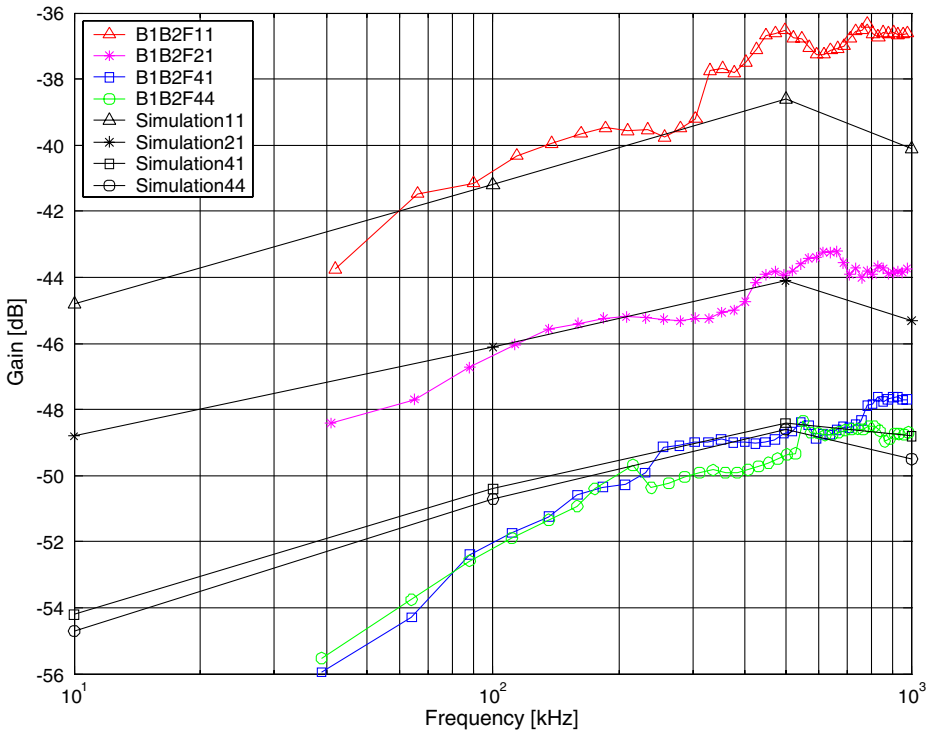

Figure 5.8: Measurement and simulation results with different electrode sizes: Attenuation on the upper arm *B1* to *B2* using *Blue Sensor* electrodes (11: Coupler and Detector 560 mm^2; 21: Coupler 280 mm^2 and Detector 560 mm^2; 41: Coupler 140 mm^2 and Detector 560 mm^2; 44: Coupler and Detector 140 mm^2)

5.2.3 Body Parameters versus Signal Transmission

From a communication point of view, there should ideally be a clear indication in which condition the human body acts as a good and in which as a poor channel medium. Thus, use of the well known body mass index (BMI) gives a general indication of whether the subject is over-weight or in the other extreme suffers a too low BMI. Regarding nutrition, the BMI is a clear indicator. Figure 5.9 shows the attenuation measurements between body points D and H1 of 6 subjects with BMI ranging from 19.7 up to 27.4. The BMI of 27.4 once results in the lowest (subject 1) and once in one of the highest attenuation (subject 6). The BMI therefore does not properly classify the subjects.

Nevertheless, the goal is to identify further indicators based on body characteristics for classifying good and poor transmission possibilities. Table 5.4 lists in detail some of the recorded bio-physiological characteristics of the 6 representative subjects. These characteristics have been recorded and calculated based on the soft tissue analyzer STA[1].

Table 5.4: BMI, skin fold, fat, muscle and body water characteristics from a set of subjects.

	Subject					
	1	2	3	4	5	6
BMI	27.4	19.7	21.4	25.6	25.4	27.4
Skin fold subscapular	17.5	11	7	21	13	29.5
Fat tissue mass[%]	22.5	23.7	24.4	26.0	40.0	31.6
Fat free mass [%]	77.5	76.3	75.6	74.0	60.0	68.4
Muscle mass [%]	49.1	51.5	57.2	44.5	40.5	38.7
Cell compound [%]	52.2	55.3	62.5	49.1	54.5	44.7
TBW[%]	56.7	55.8	55.3	54.1	48.0	54.7
ECW[%]	36.8	42.2	41.7	39.6	45.9	47.8
ICW [%]	63.2	57.8	58.3	60.4	54.1	52.2

[1] Soft Tissue Analyzer (STA) by Akern Bioresearch www.akern.com

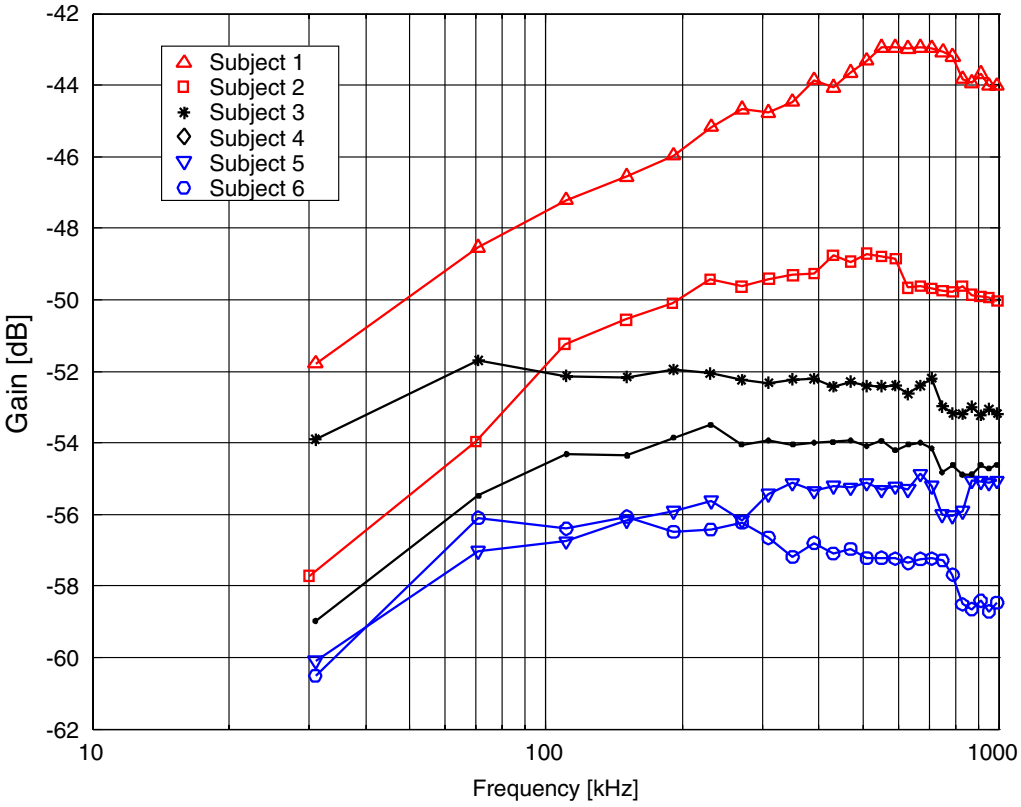

Figure 5.9: Signal attenuation of subjects 1 to 6 with fat and muscle distributions as shown in Tab. 5.4. The coupler is attached at body location *D* at the waist and the detector at *H1* at the back.

Comparing with the percentage of fat tissue mass, the attenuation characteristics presents a correlation. Figure 5.9 shows that subjects 1 and 2 both feature a low fat tissue mass and low attenuation; subjects 5 and 6 have the highest attenuation and a high fat tissue mass. Below 30% fat tissue mass, the attenuation is much lower compared to subjects with higher fat tissue mass percentage. Furthermore, a muscle mass toward 50% clearly indicates low attenuation.

The indications of skin fold thickness are not as obvious as expected. As an initial hypothesis, it can be stated that a large skin fold results in a high attenuation. This complies with the poor conductivity of skin tissue in general. However, the measurement results are ambiguous with respect to that finding.

Finally, the body transmission behavior is compared with the BIA results analyzing the total body water (TBW), the inter-cellular body water (ICW), and the extra-cellular body water (ECW). In general, a high total body water

Table 5.5: Bio-physiological characteristics of all subjects in the clinical trial calculated based on STA.

	Min	Max	Average	Deviation
R_z	436	714	567.55	86.07
X_c	47	86	69.10	11.29
Phase angle	5.2	8.1	6.74	0.93
Total body water [lt]	26.1	58.4	37.67	9.09
Extra-cellular water [lt]	11.8	21.8	15.63	3.39
Intra-cellular water [lt]	14.2	36.9	22.05	6.09
Total body water [%]	46.0	64.9	54.38	5.31
Extra-cellular water [%]	26.8	47.8	41.35	4.75
Intra-cellular water [%]	52.2	63.2	58.16	3.50
Fat tissue mass [kg]	9.3	32.1	19.68	6.77
Fat-free mass [kg]	32.6	79.8	49.53	12.34
Muscle mass [kg]	23.4	50.6	33.98	7.71
minimal energy [kcal]	951.0	2083.5	1386.80	324.32
Fat tissue mass [%]	13.6	42.5	28.49	8.19
Fat-free mass [%]	57.5	86.4	71.52	8.19
Muscle mass [%]	37.8	61.2	49.54	7.40

value indicates low attenuation. A value below 50% is a strong indicator of high attenuation. A more detailed observation of the cellular water distribution gives an interesting alignment with the attenuation behavior: the higher the percentage of inter-cellular body water, the better is the transmission in general and particularly in the higher frequency range above 200 kHz. The extra-cellular body water value influences that behavior over the entire frequency range. A percentage value above 45% corresponds with poor attenuation.

In Tab. 5.5 the bioelectrical impedance measurement results of all subjects are summarized. In accordance with the statistical distribution of TBW (54.38%$\pm$5.31), ECW (41.35%$\pm$4.75) and ICW (58.16%$\pm$3.50), it can be stated that the technology remains within a promising range for a typical subject.

5.2.4 Measurement Results of Further Body Regions

The feasibility of the technology was evaluated on further body regions within the clinical trial. Figure 5.10 shows the measured attenuation on the arm, thorax, leg, and longer path measurements with coupler and detector pairs listed in Tab. 5.3 on page 70.

Measurements on the thorax suggest that the attenuation is relatively independent of the location. In general, reasonable transmission strength in the range of 50 dB to 60 dB is observed. The attenuation on arms and legs increases exponentially with distance. Thus, transmission over large distances becomes rather difficult using the low amplitude of maximum 1 mA injected current. Especially joints (axillary *A2B1*) and large bones (pelvic bone *K2D*) act as significant attenuators.

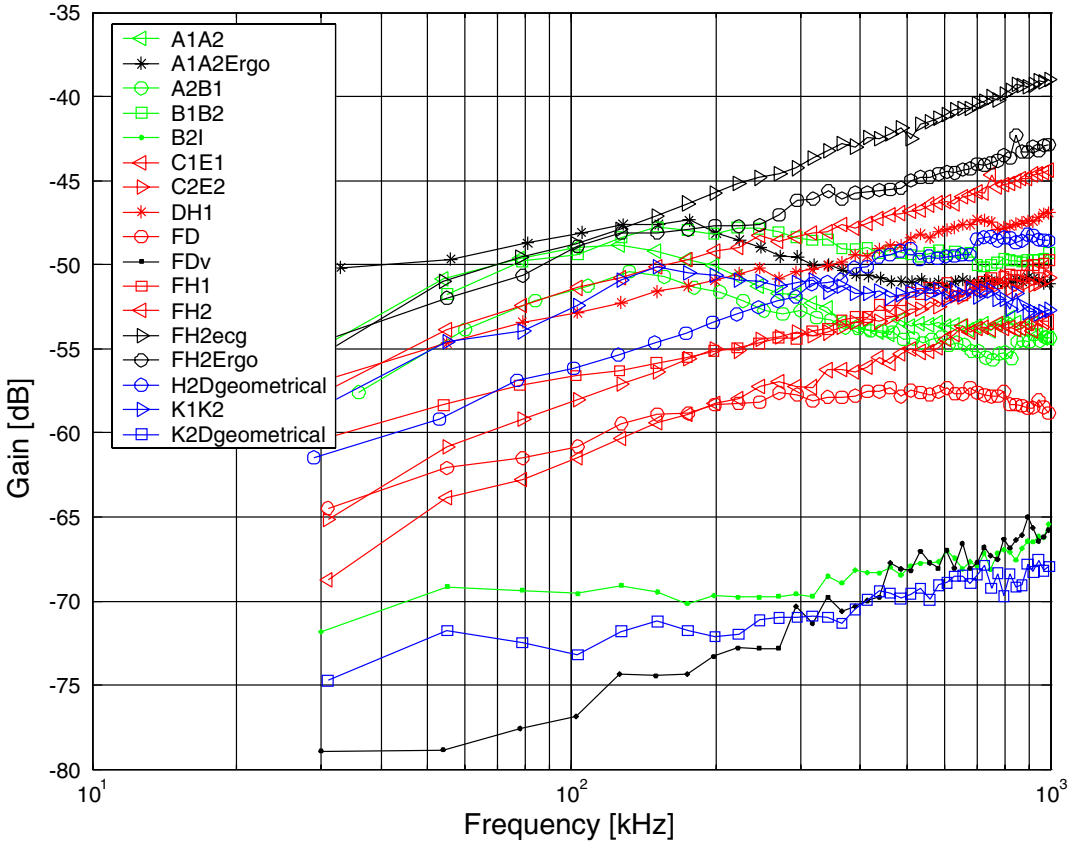

Figure 5.10: Attenuation of different body locations indexed with the coupler followed by the detector location.

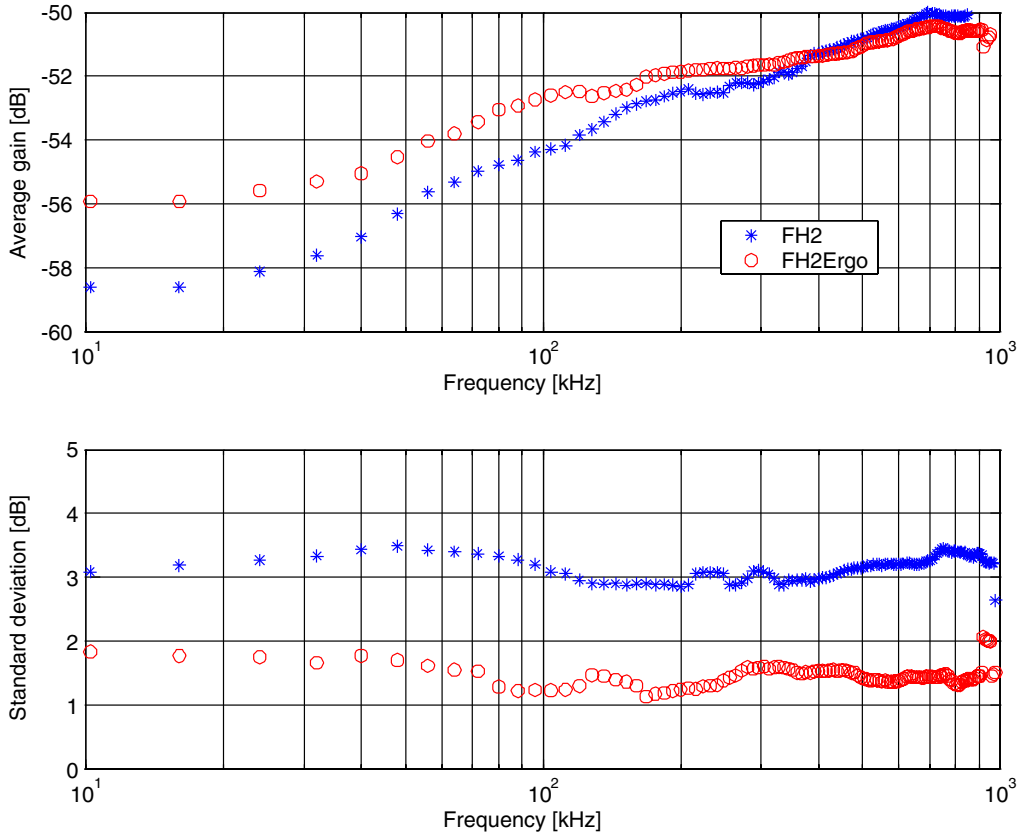

Figure 5.11: Attenuation from chest *F* to back *H2* averaged over all patients at rest and during treadmill exposure.

While attenuation in the thorax is rather independent of the location, geometrical orientation is more relevant. 90 degrees of rotation deteriorates the signal detection and results in an attenuation difference of greater than 20 dB. The recorded signals at the body point *FD* can be compared with the setup of rotated electrodes at FD_v.

Interestingly, measurements under the impact of body activity on a treadmill have not shown any degradation. In fact, the greater the level of activity, the better the coupling and the more stable the signal transmission. This behavior can be explained by the change of the skin layer consistency due to humidity brought forth through transpiration. This effect has also been indicated by the numerical simulations using the combined wet-dry skin layer model shown in Sec. 3.6.2 on page 46. Figure 5.11 shows an average attenuation of 52 dB when applying the signal between chest *F* and back *H2*. The standard deviation is lower than the results obtained on the extremities (Fig. 5.6).

5.3 Results

The clinical trial showed the feasibility of the new technology to transmit data through the human body among 20 subjects. With the proposed measurement system dedicated body parts are characterized.

- Large differences in attenuation have been observed at different body locations. Especially the thorax showed excellent transmission characteristics with typical attenuation between 50 dB and 60 dB, while the extremities and joints limited the transmission over greater distances.
- Only slight electrode displacement resulted in significant differences due to inhomogeneity and temporal altering of the human body.
- Improvements have been seen during body activity. The lower attenuation has been explained by the change of the skin layer condition due to transpiration.

Comparison with the FE simulations enabled investigations on the influence of geometry, tissue parameters, and electrodes.

- An increase in distance of 5 cm between the coupler and detector at the arm increased the attenuation up to 9 dB.
- Axillary joints have increased the attenuation up to 8 dB. Larger joints resulted in even higher attenuation.
- The size of the detector electrodes does not have an influence on the attenuation. However, larger coupler electrodes have shown lower attenuation by 6 dB with a doubling of size.

The analysis of the medical and physiological data of the subjects has indicated that

- a total body water value below 50% indicates high attenuation for signal transmission through the thorax,
- a small skin fold thickness influences the attenuation positively, and
- the ideal subject for signal transmission in the frequency range of 100 kHz to 500 kHz features a high muscle mass above 45% and a high inter-cellular body water value above 60%.

In conclusion, intra-body communication clearly has potential sensor applications on the thorax and for short distances on the extremities. Based on the existing system, a transceiver design will be miniaturized with the goal of realizing a data transmission based on galvanic coupling. Application-specific electrodes could further enhance the coupling efficiency of the technology.

Chapter 6

Intra-Body Communication Transmitter and Receiver

Galvanic coupling has been introduced as a promising coupling scheme for on-body monitoring sensors. The feasibility to transmit electrical currents of 1 mA through the human body has been shown by *in vivo* measurements. Further investigations on galvanic coupling by extended simulations have been confirmed in a clinical trial. Over all subjects, a stable transfer characteristic was found in the range of 100 kHz up to 500 kHz.

All findings have been incorporated in the implementation of transmitter and receiver units for data communication through the human body by means of modulated electrical currents. The intra-body communication transceiver shall feature

- simplicity and full integration aptitude
- low transmission power and low power consumption
- application-specific data rate

In this chapter, the entire intra-body communication transceiver design is presented. Section 6.1 explains the transceiver architecture, Sec. 6.2 shows the implementation of the transmitter and receiver units, and Sec. 6.3 presents the integration of the digital units into an application-specific integrated circuit (ASIC).

6.1 Transceiver Architecture

The transmission concept of galvanic coupling as implemented in the measurement system presented in Chapter 4 is extended by signal processing units for digital data modulation.

6.1.1 System Overview

Figure 6.1 gives the system overview of two intra-body communication transceiver units, each consisting of a transmitter and a receiver part. The digital transmitter unit encodes and modulates the data, and the coupler unit applies the signal as an alternating current to the human body. The electrode pair serves as coupler and detector electrodes for bidirectional data communication. The detector unit amplifies and filters the received signal. The digital units of the receiver demodulate and decode the data.

This architecture provides the physical and link layers according to the OSI model [Zim80]. At the physical layer, the modulated electric signal is processed and, at the data-link layer, a data symbol transmission is established

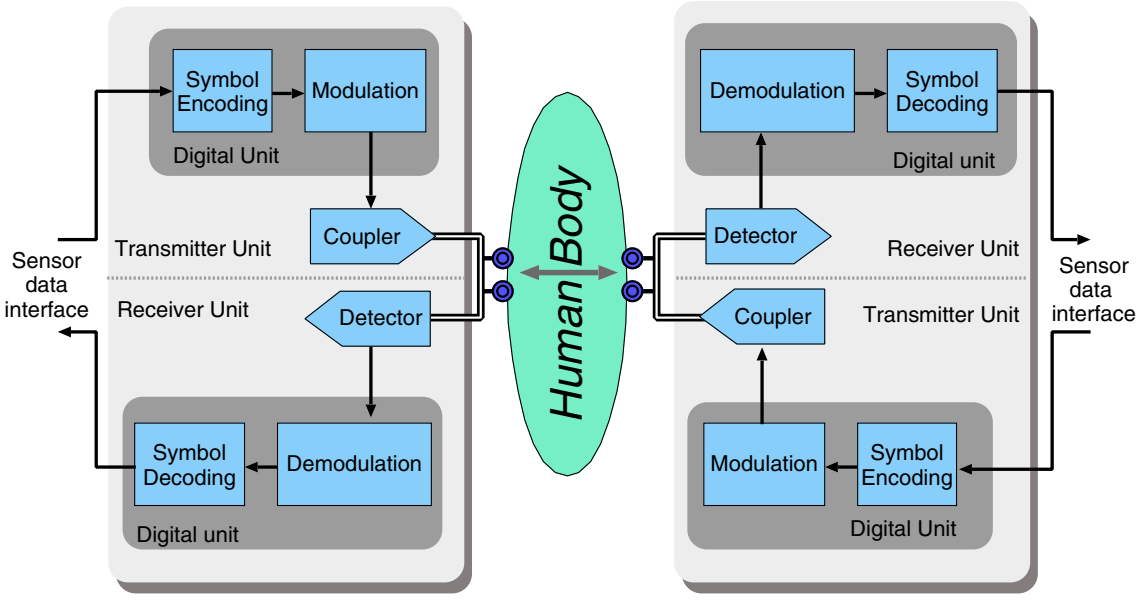

Figure 6.1: System overview of intra-body communication transceiver: A transmitter and a receiver unit are combined featuring the system blocks of the digital signal processing units, the coupler, and the detector entities.

between the transceiver units. The layered approach allows the integration of intra-body communication devices into applications in accordance with the ISO network standard [Int94] by developing a third layer of configuration and data interface to operate intra-body communication devices.

In order to enable intra-body communication for sensor networks, the hardware complexity of the transmitter and receiver units must be minimized in terms of size and power. Only then will use of the transceivers be feasible for on-body or implanted sensors with long-term monitoring. The applications require a data link with a reliable information capacity and a channel-adaptive signal transmission.

Compared to existing systems, the developed architecture will shift most of the signal processing into the digital units of the transceiver. Only the coupler and detector units are realized with discrete analog components. The digital signal processing entities perform modulation, demodulation, encoding, and decoding.

6.1.2 Modulation Methods

With narrow-band transmission techniques, the signal carrier is modulated by shifting the amplitude (on-off keying: OOK), frequency (frequency shift keying: FSK) or phase of the carrier (phase shift keying: PSK).

Table 6.1 presents a comparison of several narrow-band transmission techniques revealing their symbol content, energy efficiency, and processing complexity [Oet79]. The energy efficiency of a modulation technique can be measured as the signal-to-noise ratio required to achieve a theoretical error probability of, e.g., 10^{-4}; the lower the signal-to-noise ratio, the more efficient the modulation technique is.

According to Tab. 6.1, the PSK techniques are more energy efficient than simple OOK and FSK methods. More advanced modulation schemes, e.g., 16-QAM and 64-QAM, increase the processing complexity. Eventually, amplitude modulations are no longer suitable due to the high variations of the channel attenuation.

Phase shift keying is a commonly used modulation type for low bit-rate applications. The level of complexity required for the modulator and demodulator units is low, and the units can be implemented as purely digital entities. Therefore, BPSK and QPSK seem most suitable for intra-body

Table 6.1: Comparison of digital modulation methods with BER of 10^{-4}: data detection (N.D. = Non-coherent Detection, C.B. = Coherent Binary detection, C.Q. = Coherent Quadrature detection), symbol content, SNR, and hardware complexity [Oet79].

Modulation	Detection type	Symbol content	required SNR	HW complexity
OOK	Envelope	1	11.9	very low
FSK	N.D.	1	12.5	low
BPSK	C.B.	1	8.4	low
DBPSK	C.B.	1	9.3	low
QPSK	C.Q.	2	8.4	medium
DQPSK	C.Q.	2	10.7	medium
16-QAM	C.Q.	4	12.4	high
64-QAM	C.Q.	6	19.6	very high

communication, where simplicity, miniaturization, and energy efficiency are most important. PSK modulated signals can be generated through switching between a number of n discrete phases. Binary phase-shift keying (BPSK) switches between a 0° and 180° phase shifts. Four phase angles are available in quadrature phase shift keying (QPSK). This more complex symbol representation encodes two data bits within one data symbol and thus doubles the data rate. However, the complexity, in particular on the receiver side, is almost doubled. The PSK demodulation consists of matched bandpass filters tuned to the carrier and the phase shift. The baseband signal is decoded by a simple decision circuit.

The chosen BPSK and QPSK solutions offer low complexity and reasonable data rates. The modulation and the demodulation are both designed to be completely digital, with the aim of a mainly digital implementation and in view of future digital ASIC integration.

DBPSK and DQPSK are two modulation schemes using differential encoded data. DBPSK is used in a second prototype system presented in Chapter 7.

6.1.3 Access Methods

The intra-body network is based on a point-to-multi-point architecture with relay functionality as shown in Fig. 1.2 on page 5. The transceiver units share the human body as a common communication medium. Thus, the different signal transmissions have to be separated by access methods, in particular to allow the receiver unit to demodulate data obtained from multiple transmitters simultaneously. With respect to the protocol complexity, there are two suitable methods: time-division and frequency-division multiple access.

Time-division multiple access (TDMA) requires

- bidirectional data transmission to synchronize the devices and to control the data transfer
- a defined number of time slots, each with a distinct sensor identification

This method is used in the demonstrator design to implement time-slot-based half-duplex communication between two sensors. The sensors operate in a master-slave relation; one sensor initiates transmission, and the other sensor synchronizes to the time slots and is thus able to use its data slot. Further data slots are transmitted relative to the initial time slot. Sensor slot negotiations and retransmission are handled by the superior OSI layers. These tasks are not part of this transceiver implementation.

Frequency-division multiple access (FDMA) requires

- a unidirectional data link only; bidirectional transmission is obtained by allocating two channels
- a given number of channels and a defined channel bandwidth

The intra-body transceiver uses the method of FDMA for the separation of multiple sensors that communicate simultaneously with a dedicated sensor, e.g., the link sensor. The carrier frequency of each sensor is configurable, such that its transmission is confined to the allocated channel frequency band. In the receiver, a demodulator unit is sensitive to the allocated carrier frequency and retrieves the data.

6.1.4 Power Consumption

Intra-body communication needs to be power efficient. The energy consumed by intra-body communication devices can be divided into three major categories:

- Power consumption of the sensor signal conditioning and storage units
- Power consumption of the baseband signal processing
- Power dissipation of the analog front-end

A system analysis shows that the power consumption is mainly dominated by the system clock frequency of the digital units and the output power of the coupler units. The characteristics of the human body favor operation at carrier frequencies between 100 kHz and 500 kHz, a much lower carrier frequency than in other wireless technologies (e.g. Bluetooth or WLAN in the GHz range). The lower carrier frequency, the lower data bit rate, and the low complexity modulation offer a basis for very-low-power designs.

6.1.5 Transmission Power Budget

The channel attenuation and the signal power required at the receiver input to guarantee a certain BER define the required output power. Since the receiver front-end is equipped with high-gain, low-noise amplifiers, the contribution of the input resistor of the receiver to the noise is dominant. The corresponding input noise voltage density is $e_n = \sqrt{4kTR_{input}}$ $[\frac{V}{\sqrt{Hz}}]$. The electrode-body-electrode contact resistance R_{input} is lower than 1 kΩ, and the required SNR at the receiver input for reliable detection is at least 9 dB. To compensate for 50 dB of channel attenuation $A_{channel}$, according to

$$P_{transmitter} = 4kTR_{input} \cdot \Delta f \cdot SNR \cdot A_{channel} \tag{6.1}$$

a minimal output power of -18 dBm is required. This is well below the maximum output power of 23 dBm limited by the ICNIRP guidelines.

6.2 Demonstrator Design

The design of the demonstrator is an optimization using low-complexity modulation and a low carrier frequency to achieve reasonable data rate.

Figure 6.2 shows a simplified block diagram of an intra-body communication device. The transceiver consists of the digital modulator and demodulator units, the analog front-end, and a transceiver interface unit which samples, processes the digitized signals of the biomedical application sensor and stores the data in the local memory. The control unit configures the transceiver units in order to customize the carrier frequency, the slot length, the sensor identification, and gain settings. Initial values are configured by the data interface.

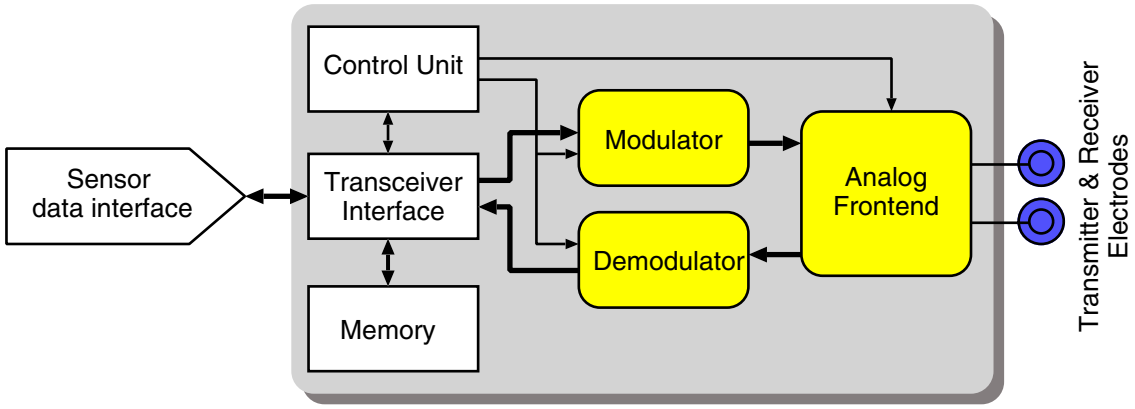

Figure 6.2: Simplified block diagram of the intra-body communication transceiver for modulation and demodulation of sensor data and transmission using a differential electrode pair.

The following subsections will describe the main building blocks of the transmitter and receiver units. The functionality will be illustrated in the example of a unidirectional link between a transmitter and a receiver unit.

6.2.1 Transmitter Unit

Figure 6.3 shows a block diagram of the transmitter. The digital transmitter unit includes the symbol encoding entity and the digital phase shift modulator, while the analog front-end provides the driver for coupling the alternating currents. In the digital symbol encoding unit, the data symbols are

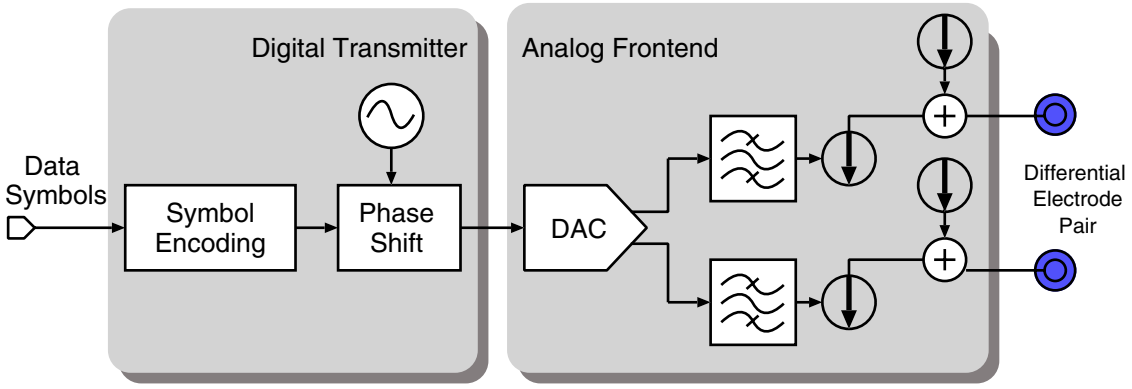

Figure 6.3: Simplified block diagram of the transmitter with digital unit (performing symbol encoding and phase shift modulation) and analog front-end (DA-conversion, filtering and current output stage).

arranged according to the time slot structure given in Fig. 6.4. A transmission frame consists of maximal 1024 data bytes plus two words of 16 bits for synchronization. The preamble synchronization words *Sync* are used in the demodulator for carrier and frame synchronization. The first data byte can be defined as the sensor identifier. This simple communication protocol allows the exchange of data between a dedicated sensor unit and the link sensor in either direction.

Depending on the modulation mode (BPSK or QPSK) of the phase shift unit in Fig. 6.3, the data bits define the phase shift of the carrier wave. BPSK uses only two states for one bit while QPSK modulates with four phases

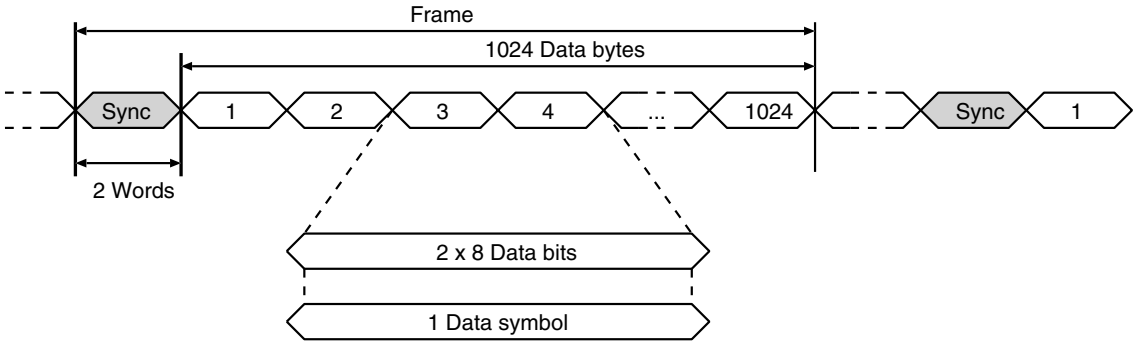

Figure 6.4: Communication protocol for unidirectional communication between the sensor device and receiving link sensor.

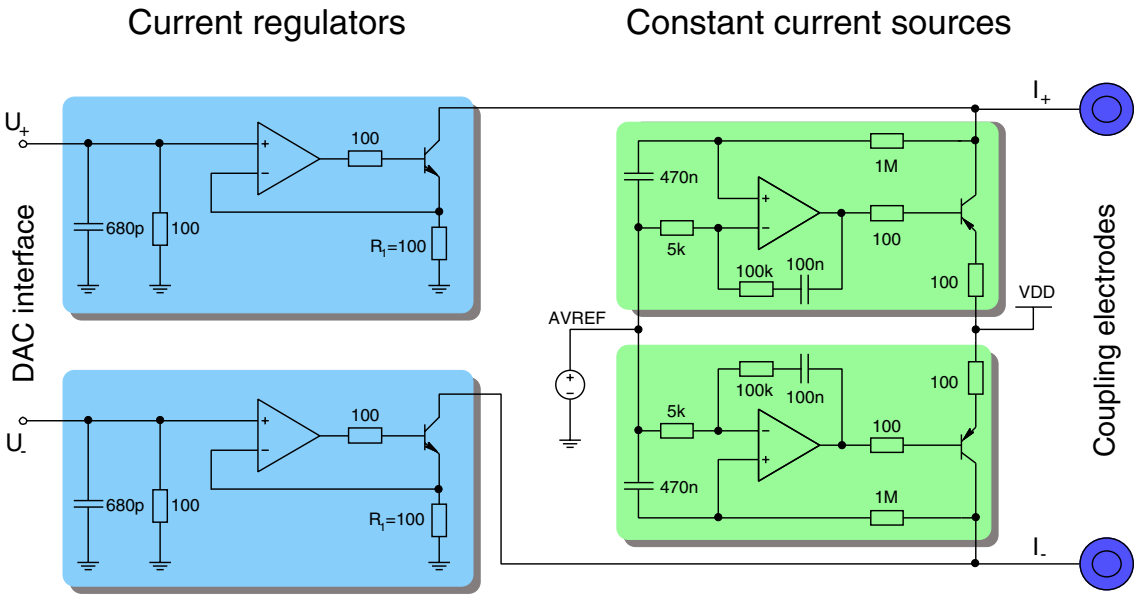

Figure 6.5: Architecture of the differential current amplifier: Current regulator driven by the DAC (left part) and constant current sources (right part).

accordingly for two consecutive bits. The frequency of the carrier sinus wave is selected by the control unit. The entire signal processing has been implemented digitally.

The signal generated in the digital transmitter unit is fed through a 12-bit digital-to-analog converter (DAC) with a differential output. The two differential signals drive the differential current output stage.

The analog output stage is shown in Fig. 6.5. It is capable of driving a load-independent differential current with a maximal amplitude of ± 1 mA. The current regulator stage filters the DAC signal and converts to a controlled current according to the load resistor R_1. A current between 0 and 2 mA is provided. The constant current source supplies a load-independent current of 1 mA. The feedback with the active filter and reference to $AVREF = 1.65$ V are required for current stabilization by compensating the oscillating output voltage level. In conclusion, the two branches each generate an alternating current of opposite polarity. The two electrode contacts provide a differential current, which means that one of the two electrode contacts supplies while the other one sinks. The coupling of the signal currents into the human tissue is performed by two exchangeable electrodes attached to the skin.

6.2.2 Receiver Unit

The simplified block diagram of the receiver unit is shown in Fig. 6.6. Passive networks filter the signals of the two detector electrodes to reduce the input noise. In order to gain the signal, a differential amplifier with constant gain amplifies and converts the signal to a single-end output. After band-pass filtering, the signal is amplified with a variable gain factor. This automatic gain control stage (AGC) is tuned by the digital receiver according to a convolution value. The amplified signal is converted by an analog-to-digital converter (ADC) and demodulated in the digital receiver unit.

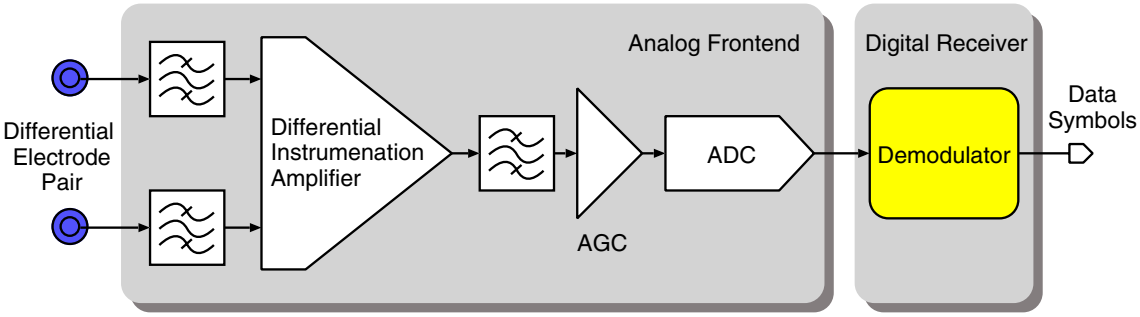

Figure 6.6: Simplified block diagram of the receiver unit with analog front-end (amplifier, band filter, automatic gain-control and ADC) and digital receiver.

Figure 6.7 shows the entire analog filtering and amplification, built of three distinct stages. A passive RC network at the front-end of the receiver suppresses out-of-band noise as well as DC offset, which occurs mainly due to the electrode-skin contact. The band selection is designed between 1 kHz and 10 MHz. The large values of the resistors and capacitances were accepted in order to conserve the high impedance input of the first stage. In a final mixed-signal integration, the large components could be omitted by including the filters within the components of the operation amplifiers.

Since only the AC part of the signal is needed for data demodulation, the first active stage has to provide a maximal common mode rejection ratio. The most suitable active amplifier structure is the instrumentation amplifier due to its differential signal branches. In the first stage, a total gain of 26 dB is sufficient with respect to the noise figure of the following filter stages. The passive components realize a pass-band between 10 kHz and 1 MHz.

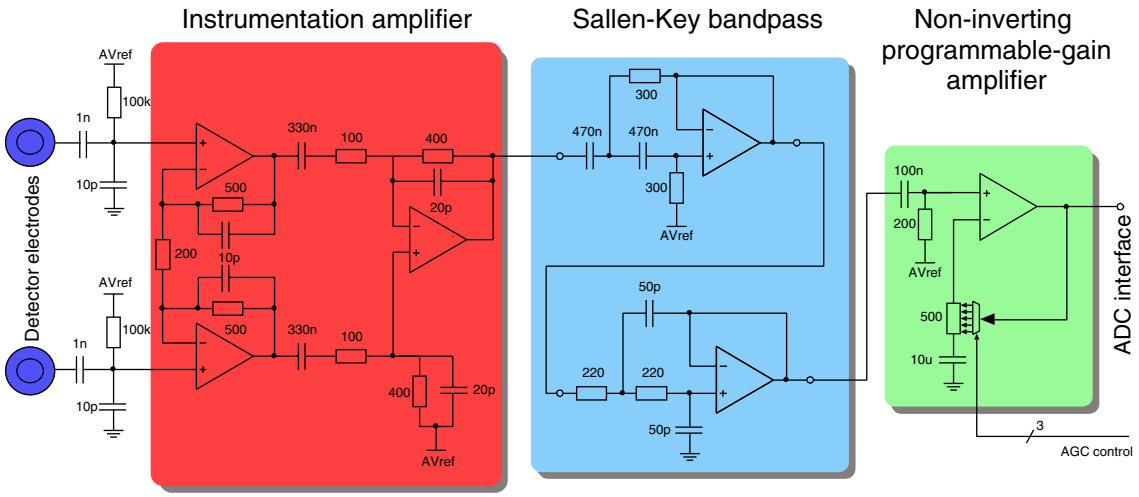

Figure 6.7: Receiver amplifier stages: Instrumentation amplifier structure (left part), second order Sallen-Key filters (middle part top: high pass; bottom: low pass) and non-inverting adaptive-gain amplifier (right part).

The second stage contains an active bandpass filter with a gain of 1. A Sallen-Key filter structure was chosen, implementing a high-pass and a subsequent low-pass filter, both second order. This bandpass strengthens the band selection and results in a total cut-off of 80 dB per decade.

The third stage features a non-inverting amplifier with programmable gain up to 46 dB. Its purpose is the final analog signal amplification to make optimal use of the ADC resolution. The programmable gain amplifier is controlled by the digital receiver. Eventually, the signal is sampled by a 14-bit analog-to-digital converter at a sampling rate of 8 MHz.

Figure 6.8 shows a simplified block diagram of the demodulator featuring the signal demodulation and the symbol detection.

In the convolution unit, the carrier phase of the input signal is sensed by filtering with an ideal sinus wave. During the convolution of the *Sync* bits (previously defined as the initial words of every transmitted frame), the carrier synchronization unit calculates the phase misalignment between the ADC signal and the local sinus-generation unit (SGU). The SGU is preset to adjust the carrier phase to the signal phase.

For demodulation, the input signal is multiplied with the in-phase and quadrature-phase signals of the digital sinus-generation unit (SGU). Both resulting signals are low-pass filtered, yielding the complex symbol for QPSK

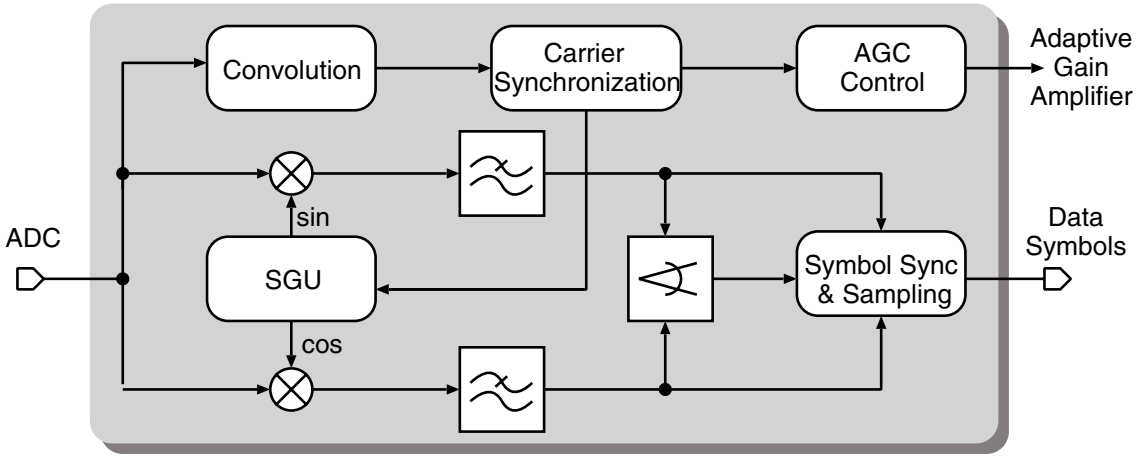

Figure 6.8: Simplified bock diagram of the demodulator including down conversion, phase estimation, carrier and symbol synchronization as well as sampling detection units.

configurations, or the bit signal for BPSK configurations. The angle detection unit calculates the phase-offset of the symbol and provides a correction value to the sampling unit.

The data symbol and the bit sampling are eventually a simple detection of the demodulated symbol; for BPSK demodulation a sign decision while in QPSK demodulation the complex value demapping is performed.

In order to generate the control value for the analog adaptive gain amplifier stage (AGC), the convolution value is low-pass filtered and compared with the optimal level stored in the configuration unit.

While the hardware complexity for carrier synchronization and AGC control is the same for QPSK and BPSK, the hardware overhead of the QPSK symbol synchronization is close to a factor of two. However, the bit rate is doubled using the QPSK mode.

6.3 Implementation Results

This section presents the implementation results of the intra-body communication prototype optimized to use the human body as the transmission medium of electrical currents. The key design parameters of the transceiver prototype are listed in Table 6.2.

The entire transceiver unit is shown in Fig. 6.9. It includes a transmitter unit and a receiver unit for bidirectional communication on a board with the size of a credit card. The presented prototype allows the parameterization of the dedicated carrier frequencies and the two modulation types. The digital unit with data interface, modulator and demodulator uses 1200 slices of the XILINX SPARTAN IIE FPGA for BPSK modulation, and 10% more for QPSK. The analog part is built with discrete elements.

In order to deal with a typical attenuation of 60 dB for signals through the human thorax, the receiver system provides analog filtering in the frequency window from 10 kHz to 1 MHz and an adaptive receiver gain between 26 dB and 72 dB. A more advanced and adaptive channel equalization could further enhance the signal detection.

Table 6.2: Key parameters of the intra-body transceiver demonstrator.

Parameter	Value
Peak current output	± 1 mA
Carrier frequency range	10 kHz - 1 MHz
Frequency accuracy	8 kHz
System clock frequency	8 MHz
Converters (DA, AD)	12-bit, 14-bit
Receiver gain	26 dB - 72 dB
Complexity	BPSK: 1200 slices, QPSK: 1310 slices
Maximal data rate	64 kbit/s
Supply	3.3 V battery
Power consumption	Overall: 726 mW
	Digital units & AD-DA converter: 490 mW
	Analog front-end: 60 mW
	Data interface (optical): 160 mW

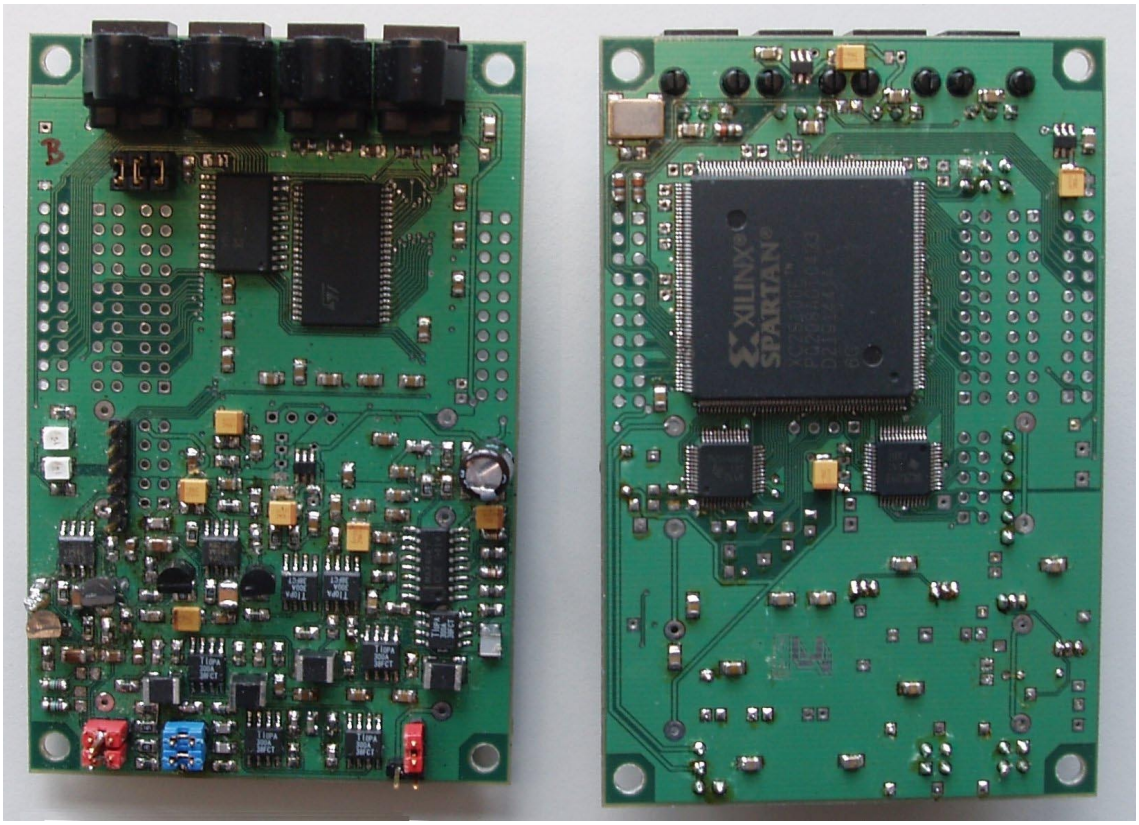

Figure 6.9: Intra-body communication transceiver PCB: 4 layers, 62.7 cm^2. Top layer (left): opto coupler, PROM, SRAM, and analog front-end; bottom layer (right): Oscillator, FPGA, DAC, and ADC.

Feasibility tests on the upper arm with the prototype in QPSK mode have achieved a data communication rate of up to 64 kbit/s. The carrier frequency has been chosen at 256 kHz and a bit error rate (BER) of less than 10^{-4} has been measured. Combining multiple frequency-separated channel allows transmission speeds for all envisioned target applications.

In view of future integration, all digital parts of the transmitter and receiver units have been implemented into an ASIC. The layout is shown in Fig. 6.10. The implementation occupies a standard cell area of 1.4 mm^2 plus four dedicated on-chip RAM units of 0.8 mm^2, resulting in an entire core area of 3.56 mm^2 in a UMC 0.25 µm process. The realized implementation consists of 26.9 kGE for the QPSK and 25.7 kGE for the BPSK transceiver units counting the processing units only.

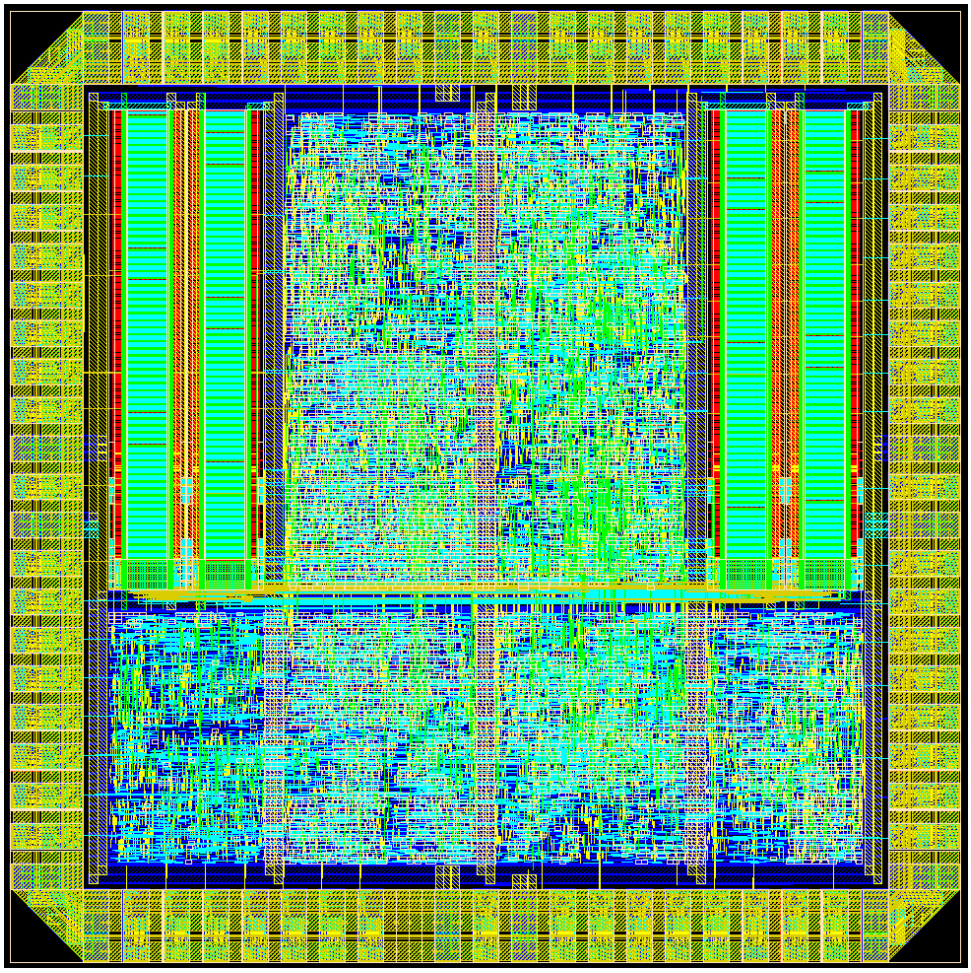

Figure 6.10: Layout of the ULTRACOM transceiver: BPSK and QPSK digital processing units for intra-body communication implemented as an ASIC in UMC 0.25 µm with a core area of 3.56 mm^2.

Table 6.3: Key parameters of the ULTRACOM ASIC.

Parameter	Value
Process	UMC 0.25 µm (5 metal, 1 poly)
Clock	1 clock domain @ maximal 100 MHz
Supply voltage	Core: 2.5 V, I/O: 2.5 V - 3.3 V
Pads	I/O pads: 67, power pads: 16
Core area	3.56 mm^2 (on-chip RAMs: 0.8 mm^2)
Complexity	QPSK: 26.9 kGE, BPSK: 25.7 kGE
Power consumption	35 mW @ 8 MHz (estimate)

For the first time, a transceiver system deploying galvanic coupling and digital PSK modulation has been implemented for intra-body communication. The novel approach has been demonstrated. *In vivo* tests have proven the feasibility of the transmitter and receiver concept. The presented solution is attractive for biomedical applications with long-term monitoring of patients, where power is tight and miniaturization a must.

Chapter 7

Wireless Implant Communication

As shown in the previous chapters, galvanic coupling enables data transmission between sensor units for low frequency intra-body communication.

In this chapter, that approach is extended to implantable miniaturized devices. A communication system for wireless data transmission in muscle tissue is developed. The prototype offers four concurrent channels with a throughput of 4.8 kbit/s. The main focus is the future implantability of such a miniaturized system for medical long-term surveillance of patients. In order to achieve this goal, small circuit size, low power consumption, and electrical safety have to be carefully considered.

7.1 Implantable Monitoring Devices

Future monitoring devices for biomedical application will offer the possibility to observe a patient's long-term condition via implanted devices. Galvanic coupled units have been tested in tissue [LMHH98]. Recent studies have focused on intra-body communication, with implanted miniaturized pills operating as transmitter and receiver by deploying coils [SHC05] and volume conduction (galvanic coupling) [SMW+04, SMW+06, YLSS06].

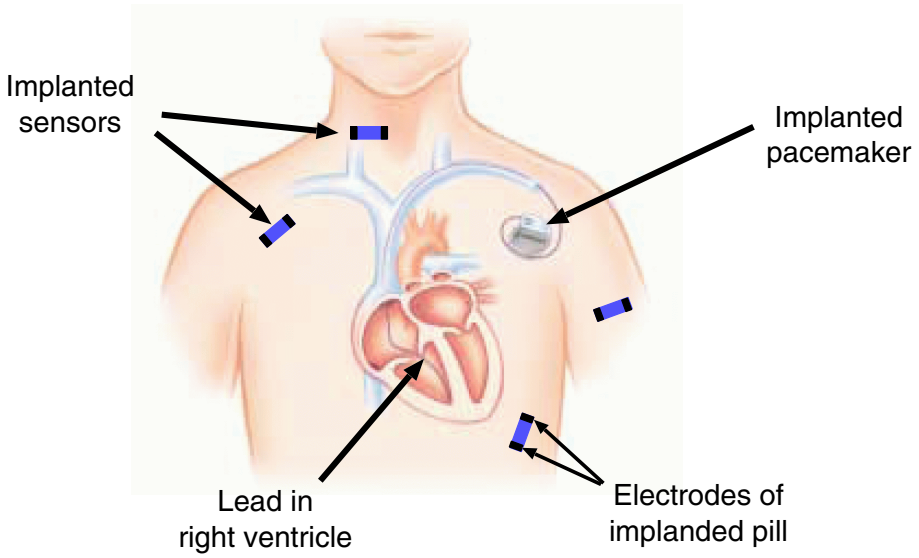

Figure 7.1: Distributed implanted sensors: Miniaturized sensor pills communicate with each other. The implantable cardioverter defibrillator and its lead could serve as a particular sensor of the network.

This work proposes the technology of galvanic coupled implantable pills as shown in Fig. 7.1. Instead of skin-mounted electrodes, the differential electrodes that build the two ends of the pills are used to couple the alternating current into the human tissue. Since muscle tissue is more conductive compared to skin tissue, it can be assumed that lower communication losses will result. The frequency range between 100 kHz and 500 kHz has been investigated according to previous feasibility measurements [HK06]. A constant broad frequency bandwidth allows implementation of a frequency division multiple access (FDMA) system.

Since this communication system is planned for use in a biomedical application, it must be safe for the patient. No interference with the patient's body functions is allowed, e.g., its nervous system. Therefore, the emission of signals with a frequency below 10 kHz is not allowed, since body signals are located in that frequency range. Special care has been taken with respect to low-power design. The system should be able to run over a long time period without recharging. In this project, the developed prototype aims at a reliable, low-power data link between four transmitter units and one receiver unit. A data rate of 4.8 kbit/s allows the sensors to transmit real-time data for monitoring human vital parameters, e.g., temperature, SpO_2, ECG. The system architecture has been developed in view of a future single system-on-chip design.

7.2 Galvanic Coupling with Implants

The measurement system described in Chapter 4 has been reused for the feasibility measurements of the setup for implants. The principle and the investigated frequency range are unchanged; the setup couples a sinusoidal output current up to 1 mA in a frequency range of 10 kHz to 1 MHz.

For the experiments on the galvanic coupled implants, the measurement setup was modified to enable connection to the electrodes of the implantable pill instead of the on-body electrodes. For the initial experiments, an oversized pill model with connectors on both ends has been realized. As shown in Fig. 7.2, two versions of electrode pairs have been investigated; long electrodes of cylindrical copper (length 1 cm and diameter 4 mm) and short electrodes with only the circular surface to provide contacts (4 mm). For better comparison with earlier on-skin electrode measurements [WOF+06b], the distance between the electrode contacts was chosen as 5 cm. The electrode cables are shielded. The shields are connected to the reference potential on the measurement system units.

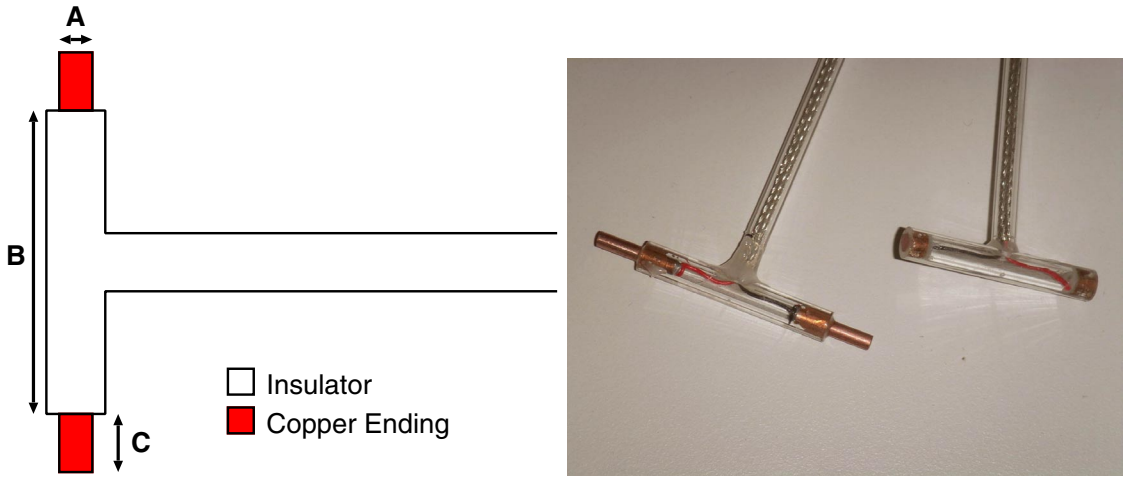

Figure 7.2: Image of the two pill models on the right-hand side, construction details on the left hand side. The two versions used had the dimensions: A = 0.4 cm, B = 5.0 cm, C = 1.0 cm for the longer electrodes and C = 0.0 cm for the short electrodes.

7.3 Simulation

Simulations of the pill-pill communication have been performed using the *Comsol Multiphysics* (formerly *FEMLab*) finite-element simulation platform. The dimensions of the simulated components are much smaller than the wavelength of the induced EM waves. Therefore, quasi-static simulations were used.

The numerical model sown in Fig. 7.3 reflects the measurement setup regarding dimensions and the dielectric parameters of the liquid. The pills were modeled as two copper elements placed on a dielectric rod. A current flow was used as excitation. The boundaries of the model are electrically insulating. Different distances (5, 10, 15 and 20 cm) between the two pills were computed. Simulations for two long (C = 1 cm) and two short (C = 0 cm) electrode pills were performed separately. The muscle tissue parameters given in Gabriel *et al.* [GLG96b] were used for the simulations at discrete frequencies. The attenuation was calculated via integration of the potential over the corresponding surfaces.

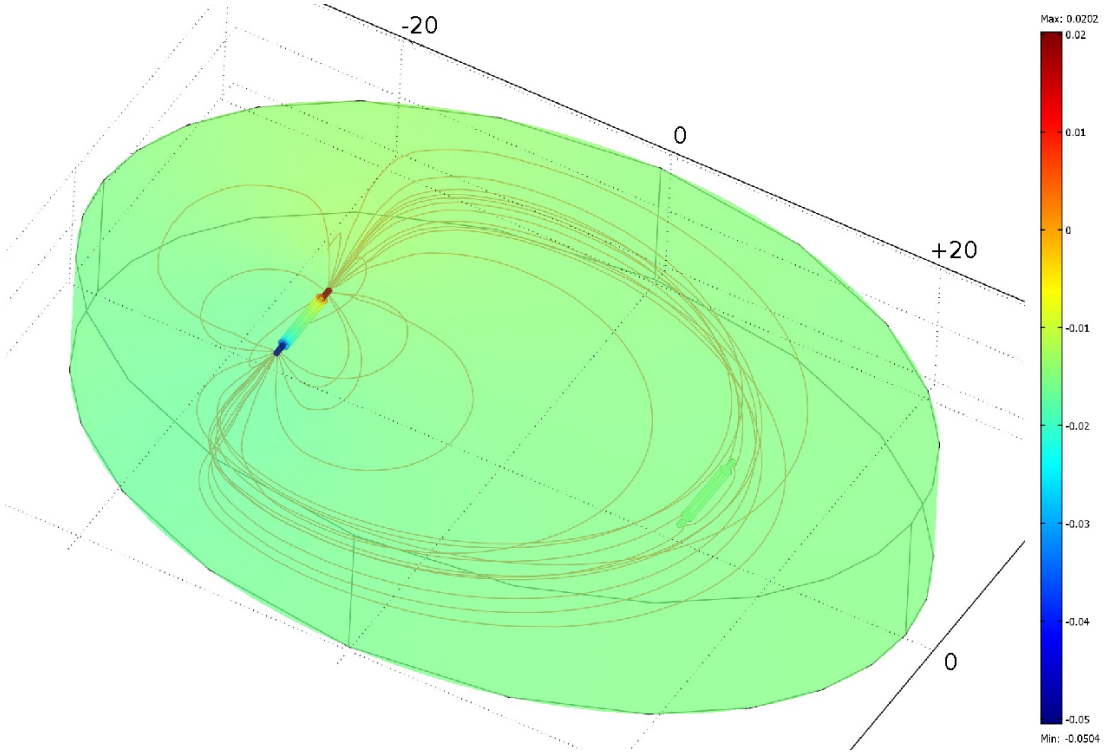

Figure 7.3: Numerical model of the measurement phantom including the distribution of the electric potential for the configuration of the long transmitter and receiver pills.

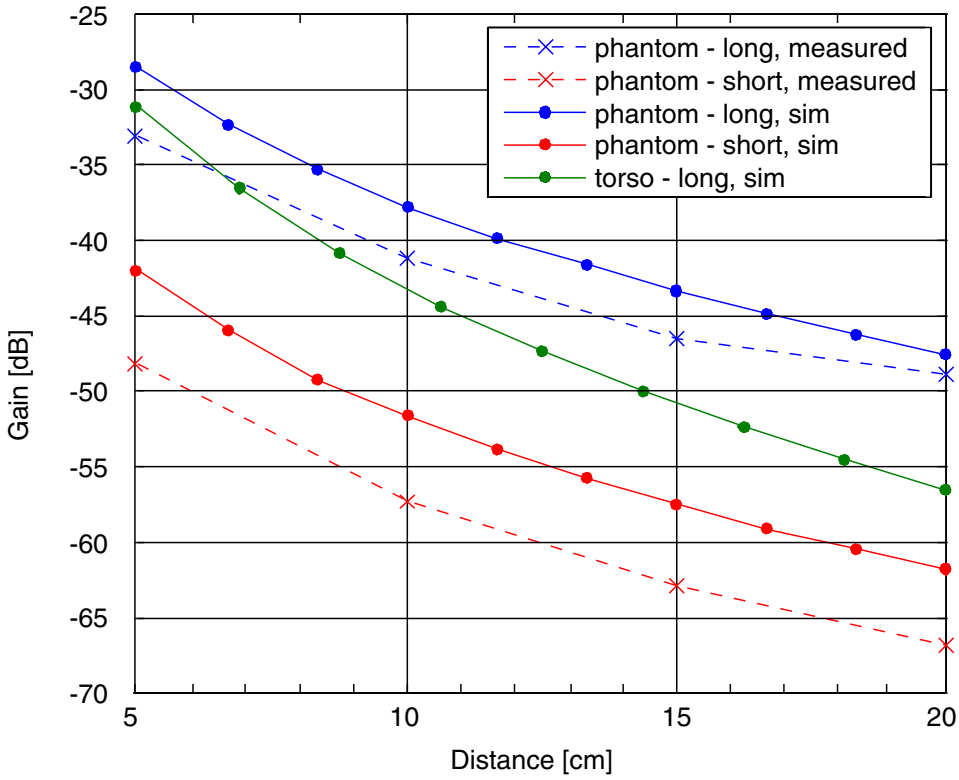

Figure 7.4: Comparison of simulated results and typical measurements of the attenuation for galvanic coupling of the two pill types at 300 kHz. In addition the simulated attenuation in a simplified torso model is shown.

Figure 7.4 shows the numerical simulations and measurements of the two electrode configurations performed at 300 kHz. In addition the attenuation of a homogeneous elliptical cylinder having the same dielectric parameters representing a simplified torso model is shown. The dimensions of the elliptical cylinder are approximate values based on the measurements taken from adults of age between 31 and 60 years [TU]. The attenuation of the torso model suggests a higher attenuation within the body compared to the experimental phantom. This requires further investigated by using an anatomical model representing the different organs and tissues.

7.4 Measurements

It has not been possible to implant the test electrodes into a human body to conduct measurements for this study. Instead, feasibility measurements have been performed in simulation liquid with a dedicated measurement setup.

7.4.1 Measurement Phantom

An elliptical phantom of the size 60 × 40 × 10.5 cm was used, as shown in Fig. 7.5. The phantom was filled with *MSL27*, a liquid which has the same electromagnetic properties as muscle tissue at 27 MHz. No liquid was available for the lower frequency range. The pill models were inserted 5 cm deep into the liquid and attached to isolated holders. Measurements were conducted with increasing distance between the transmitter and the receiver, starting at 5 cm and ending at 45 cm in steps of 5 cm. The tests were performed inside an anechoic chamber, such that environmental noise was kept to a minimum level.

7.4.2 Measurement Results

The firmware of the transmitter was configured to generate sinusoidal waves at the following frequencies: 100, 200, 250, 300, 400, and 500 kHz.

The measurement results for optimally aligned electrodes look promising,

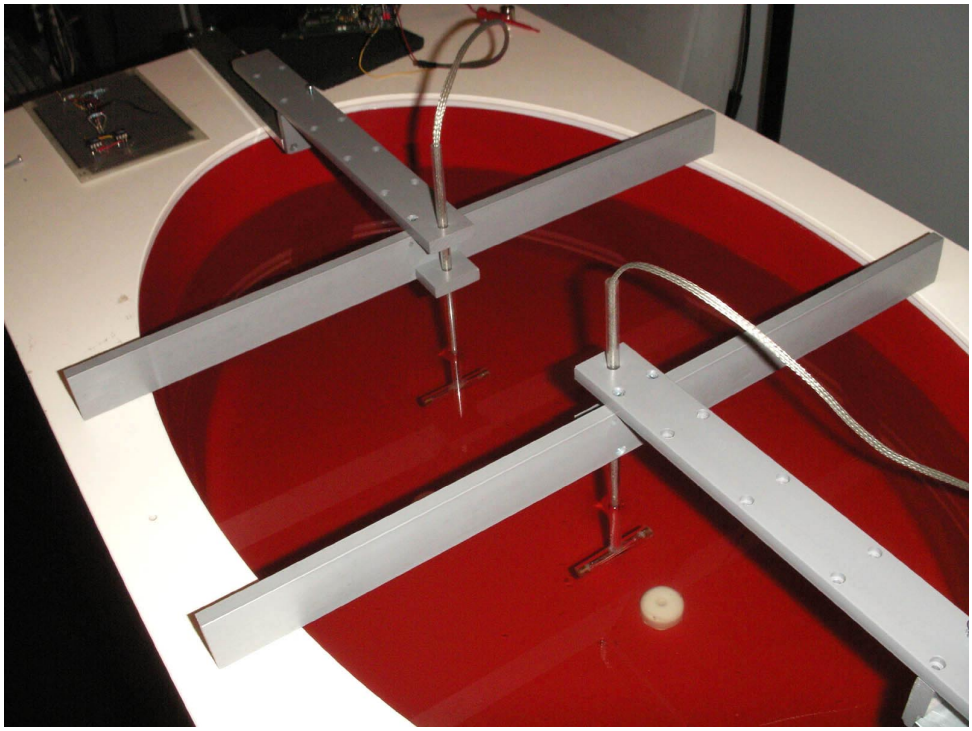

Figure 7.5: Image of the measurement setup with the long electrodes inserted into the measurement phantom.

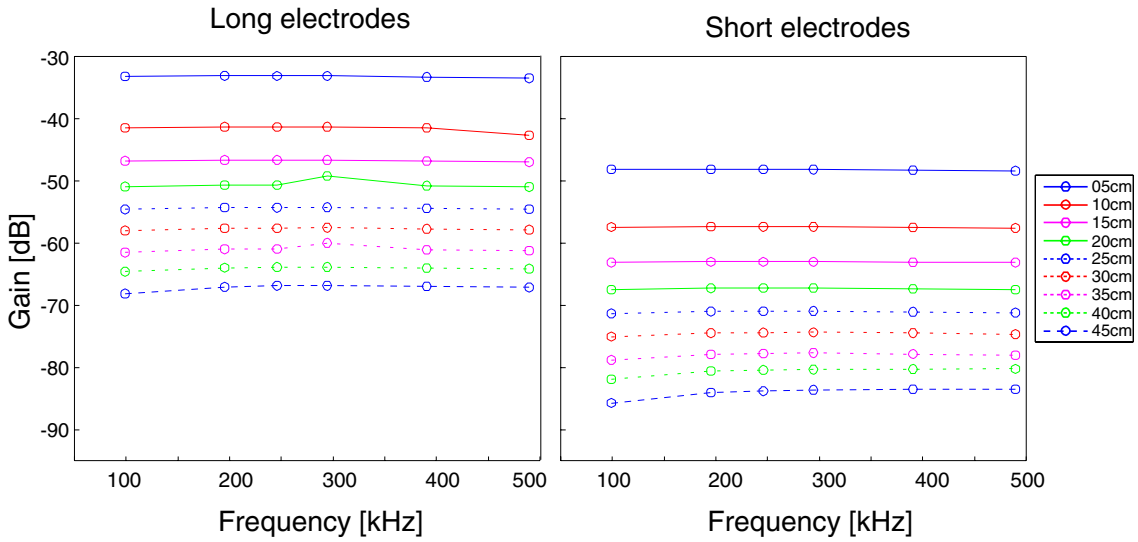

Figure 7.6: Measured gain of the galvanic coupled electrodes with long and short electrodes.

as shown in Fig. 7.6. The main difference between the long electrodes and the short electrodes is a 15 dB lower attenuation; the other properties of the transmission characteristics are very similar.

Additional measurements have been conducted to determine the worst-case condition of the transmission method. Table 7.1 gives the combination of transmitter and receiver rotations. The rotations by 0° or 90° were chosen to simulate unfavorable alignment. These measurements were conducted with the long electrodes. The results are summarized in Tab. 7.1. When only the transmitter electrode is rotated, a signal loss of about 15 dB is caused, while a rotation of only the receiver electrode did not allow detection of useful signals.

Table 7.1: Pill orientation measurements: Transmitter and receiver pill angles and resulting attenuation.

Transmitter angle	Receiver angle	Attenuation [dB]
0°	0°	47
90°	0°	62
0°	90°	n/a
90°	90°	49

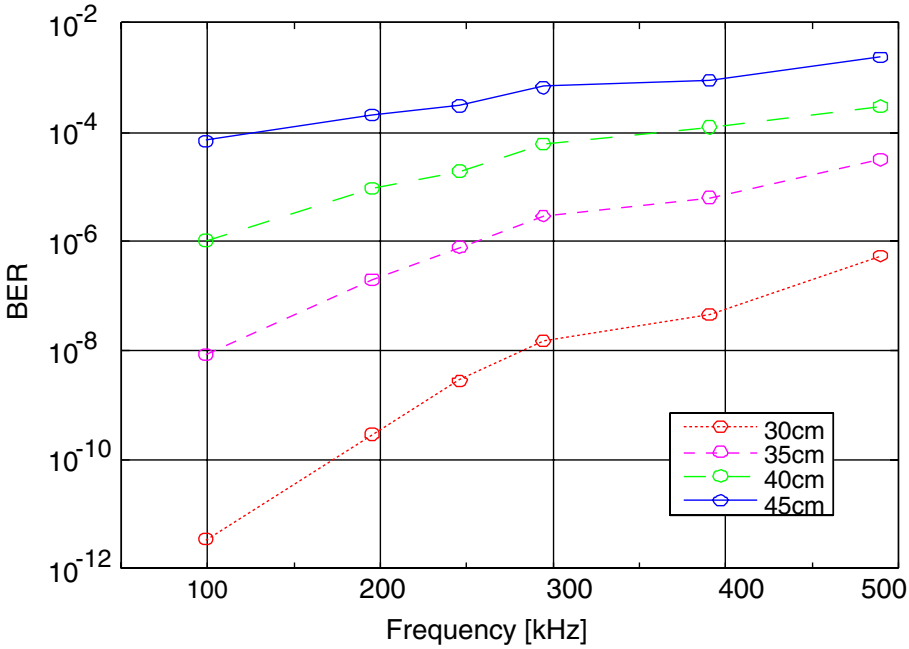

Figure 7.7: BER estimations for galvanic coupling with the long electrodes.

Finally, the bit error rate (BER) has been estimated, based on recorded data, and calculated according to

$$BER = \frac{1}{2}\text{erfc}\left(\sqrt{\frac{E_b}{N_0}}\right), \qquad E_b = \frac{A\sqrt{T_b}}{\sqrt{2}}$$

where E_b is the signal energy per bit, A is the signal Amplitude, T_b is the duration of one bit and N_0 the mean noise power spectral density of the received signal.

Figure 7.7 shows that the BER is estimated below 10^{-4} up to 35 cm measurement distance for all frequencies. It must be considered that the calculation of the BER depends on the chosen modulation scheme and the duration of one symbol. Therefore, the BER plot for BPSK presented here can only be used as a rough estimation.

The discrepancies between simulated and measured results shown in Fig. 7.4 on page 103 can be explained by the liquid in which the measurements have been performed. This liquid simulates the electrical properties of muscle tissue at 27 MHz.

7.5 System Design

For reasons of simplicity, the system approach considers a unidirectional communication system with four transmitters and a central receiver. A frequency division multiple access (FDMA) system has been realized. This choice offers more freedom for transmitter separation compared to time division multiple access (TDMA). The latter has not been chosen due to the fact that slot negotiation and synchronization would require bidirectional communication and additional effort in synchronization. The carrier frequencies of the four channels in this application are located at 100, 150, 200, and 250 kHz.

For demonstration purposes, the electrical decoupling of the sensor from power nets is realized with opto couplers and battery powering. The transmitter and the receiver units use 3.3 V supply voltages from a battery.

7.5.1 Digital Communication Methods

Differential binary phase shift keying (DBPSK) modulation has been chosen. It incorporates differential encoding, including an error correction code and consecutively binary phase-shift modulation.

Differential Encoding and Error Correction Code

The transmission is independent of the absolute carrier phase; the information is encoded in the phase difference between two consecutive symbols. Hence the orientation of the implants does not affect the transmission. Therefore, much more freedom is offered to the surgeon for placing the units in the body.

The encoding process is illustrated in Tab. 7.2. Every binary ‘0’ data bit flips the state of the last encoded bit; every ‘1’ leaves it unchanged, and the same value is encoded again. Thus, the information is encoded in the phase shift of the carrier wave rather than the phase itself.

In addition, a hamming code for detection and correction of one faulty received bit per data byte has been realized. Per data byte, four additional hamming bits have to be included into the data stream. Therefore, a transfer rate of 7.2 kbit/s is required to achieve the desired data throughput of 4.8 kbit/s.

Table 7.2: Generation of differentially encoded data: The encoded sequence is initialized by 1

Data sequence	Init	1	0	0	1	0	0	1	1
Encoded sequence	1	1	0	1	1	0	1	1	1
Transmitted phase	0	0	π	0	0	π	0	0	0

Modulation Scheme

Following the differential encoding, binary phase shift keying (BPSK) modulation was chosen due to the high immunity to amplitude variations. Furthermore, BPSK offers low complexity for modulation and demodulation. The carrier frequency of the corresponding transmitter unit is modulated with the encoded information sequence. In DBPSK, the transmission of an encoded '1' results in no phase shift, while a '0' shifts the phase by 180 degrees.

Pulse Shaping

The signal-to-noise ratio of each channel can be improved by shaping the modulated signal by a window function.

Ideally, the *sinc* function

$$A_{sincpulse} = sinc(x) = \frac{sin(\pi \cdot x)}{\pi \cdot x} \quad \text{for} \quad -\infty \leq x \leq \infty \tag{7.1}$$

transforms to a rectangle in Fourier space. Due to hardware limitations, the filter length of the pulse shaping window is limited. With a sampling rate of 1 MHz and a bit rate of 7.2 kbit/s, one bit pulse contains 140 samples. The *sinc* window length shall match the number of samples per bit. Therefore, the *sinc* function is cut at $x = -1..1$. The spectrum of *sinc* shaped BPSK is not ideally rectangularly shaped, but possesses side lobes. Regarding a signal bandwidth of 50 kHz per channel, the spectrum of the pulse shaped signal at $f_{center} \pm 25$ kHz is more than 20 dB lower than the unshaped BPSK spectrum as shown in Fig. 7.8. Therefore, the pulse shaping will result in a significant improvement of the signal-to-noise ratio if multiple transmitters are active simultaneously.

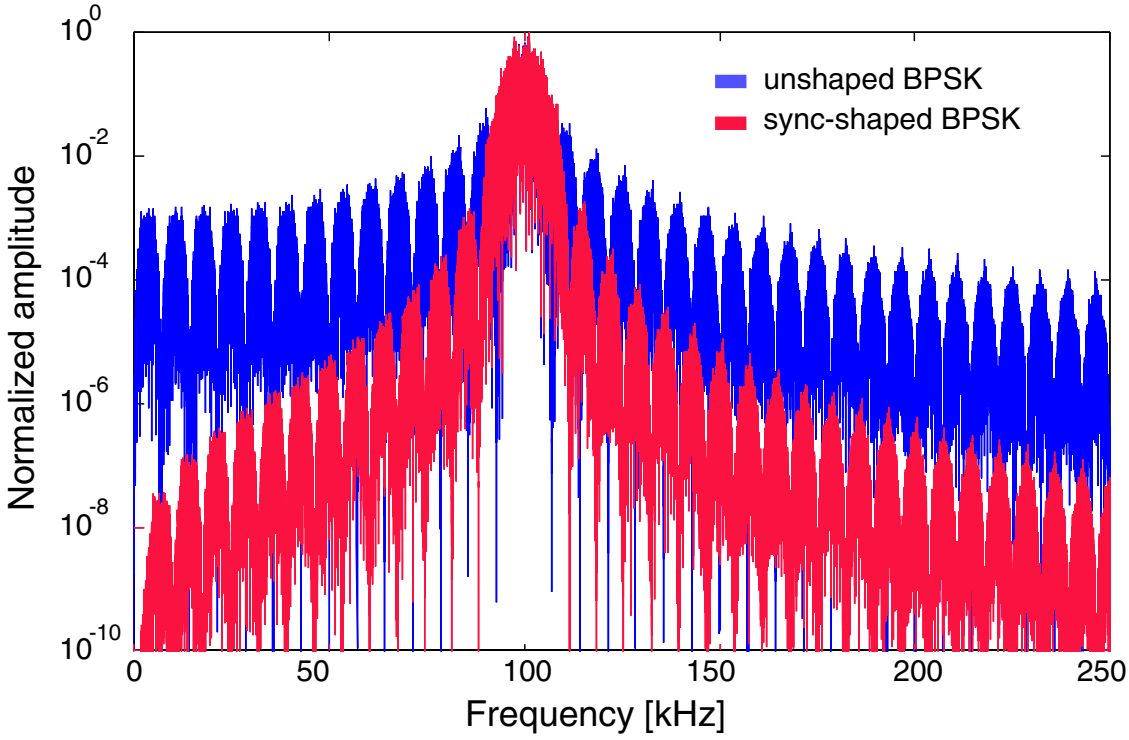

Figure 7.8: Normalized spectrum of the BPSK modulated signal with and without pulse shaping using a center frequency of 100 kHz, a bit rate of 7.2 kbit/s and a sample rate of 1 MHz.

7.5.2 Functional Blocks of the Transmitter

The transmitter is composed of a minimal number of operational units, as shown in Fig. 7.9. A CPLD contains all digital signal processing units of the transmitter. It is perfectly suitable for the transmitter complexity, and it will be replaced by a future ASIC integration.

As shown in Fig. 7.9, a serial interface serves to configure the digital unit and provides data for the transmission. The highest carrier frequency of 250 kHz defines the system clock of 1 MHz, providing four times oversampling. The digital part implemented in the CPLD feeds data through an 8 bit digital-to-analog converter (DAC) to the analog output driver. A parallel input DAC is used, since a serial input would require an eight times higher system clock frequency for the data transmission, resulting in a higher power dissipation. In order to save energy while no data is sent, the entire analog part can be shut down.

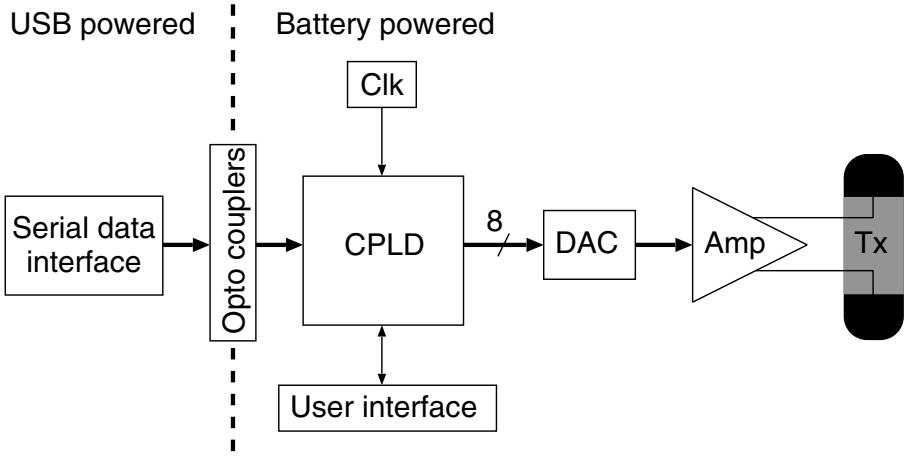

Figure 7.9: Block diagram of the transmitter: Serial data is DBPSK modulated and differentially coupled to the pill electrodes by a current amplifier.

The analog part is presented in Fig. 7.10. The two symmetrical branches include the current regulators and the constant current sources. The architecture is a simplified version of the design presented in Chapter 6 (Fig. 6.5 on page 91). The signal filtering in the current regulators is omitted and the discrete elements are adapted.

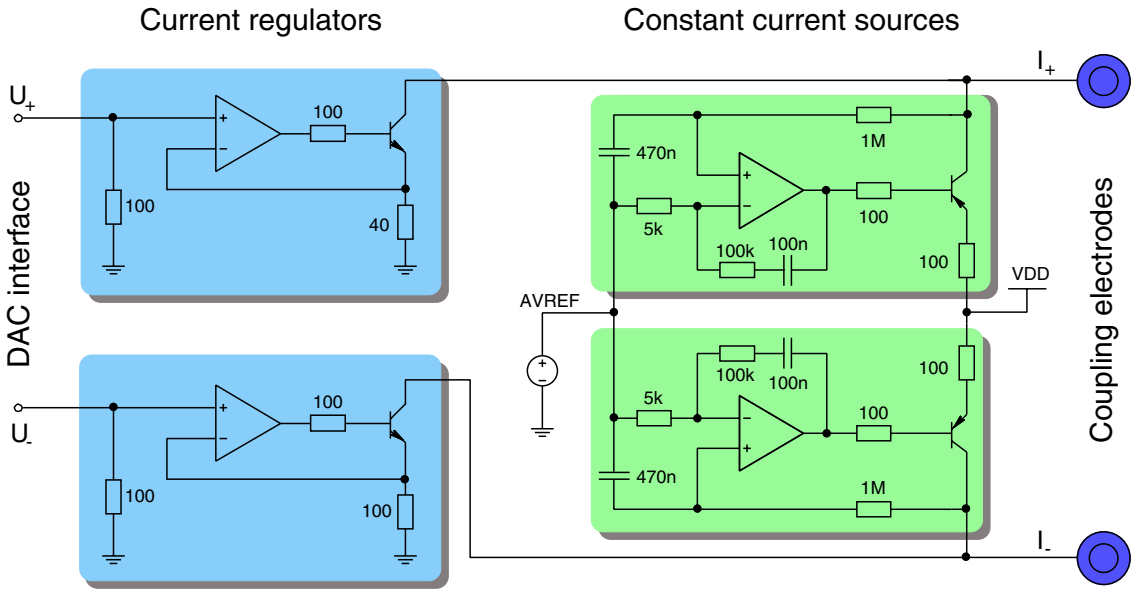

Figure 7.10: Schematic of the differential current amplifier: Current regulators driven by the DAC (left part) and constant current sources (right part).

7.5.3 Functional Blocks of the Receiver

Figure 7.11 shows the main functional blocks of the receiver with the analog input amplifier and filter, ADC, and the FPGA, providing the digital demodulation and interfaces. The input amplifier of the receiver must amplify very weak signals to a level resolvable by the following 14-bit ADC. The amplitude of the input signal between the receiver electrodes ranges from about 5 mV at 5 cm down to about 5 µV at 45 cm distance. The primary goal for the design of the amplifier is minimal noise; the secondary goal is low power consumption.

The amplifier is built in three stages as presented in Fig. 7.12. The analog design is based on the structure of the initial design in Chapter 6 (Fig. 6.7 on page 93). Each of the amplifier sections is designed to amplify the incoming signal by a factor of 10. The instrumentation amplifier of the first stage is simplified by omitting the passive input filters.

The bandpass filter in the second stage has been implemented as a Sallen-Key structure. The discrete elements are redimensioned for much smaller capacitors. The values of the filter elements can be calculated according to

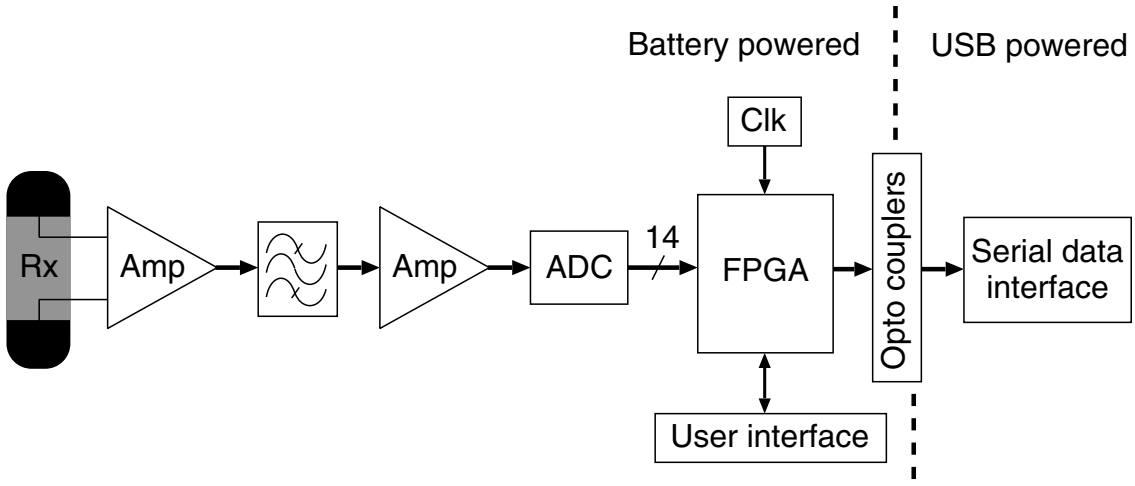

Figure 7.11: Block diagram of the receiver: Received signals are bandpass filtered, amplified, analog-digital converted, digitally demodulated, and decoded for serial data transmission.

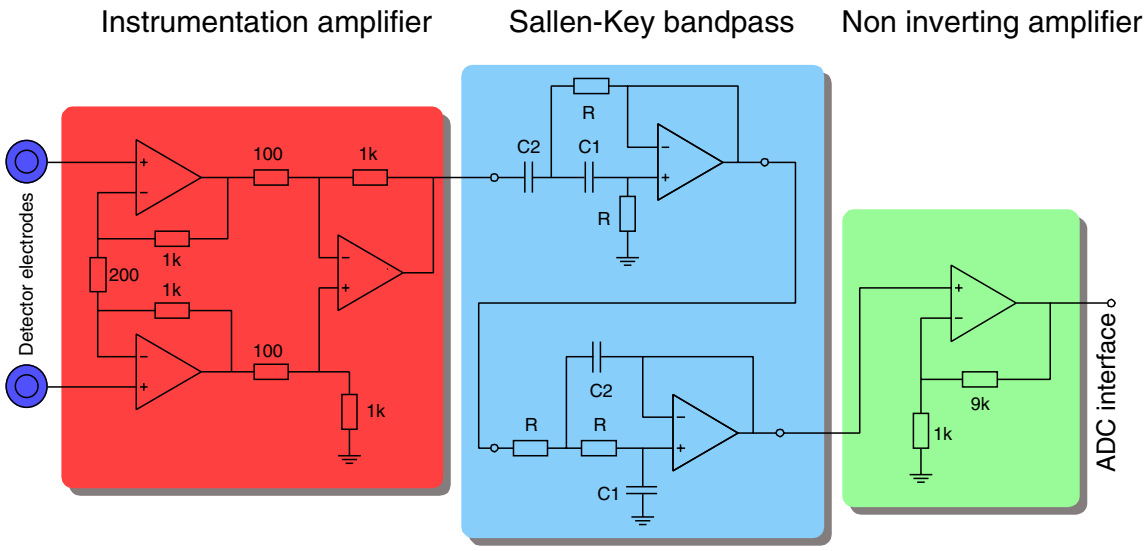

Figure 7.12: Simplified input amplifier stages for implant communication: Instrumentation amplifier structure (left part), second order Sallen-Key filters (middle part top: high pass; bottom: low pass) and final non-inverting amplifier (right part).

the following formulas

$$C1 = 2 \cdot C2 \tag{7.2}$$

$$R = \frac{\sqrt{2}}{4 \cdot \pi \cdot f_c \cdot C2} \tag{7.3}$$

where f_c is the 3 dB cutoff frequency and the ratio of *C1* and *C2* is chosen 1:2. The cutoff frequencies are 75 kHz for the high pass and 350 kHz for the low pass filters.

The third stage contains a non-inverting amplifier. The gain is fixed to 10, which reduces the hardware complexity but loses the configurability of the gain stage. All stages have a total amplification of 60 dB.

The digital part of the receiver is implemented in the FPGA. As shown in Fig. 7.11, the FPGA receives the digitally converted signal, transmits the demodulated data to the serial interface, and provides a user interface. DBPSK demodulation is implemented for up to four transmitted signals concurrently. The FPGA's built-in digital clock managers, multipliers, and data storage structures offer convenient features for the data decoding. The FPGA-based prototype allows easy migration of the architecture into a system-on-chip (SoC).

7.6 Implementation Results

The developed sensor network consists of four transmitter boards and one receiver board (Fig.7.13). The key parameters of the two units are given in Tab. 7.3.

The current output of the transmitter unit drives 1 mA up to a load of 1 kΩ. This is by far sufficient considering the coupling measurements of muscle tissue. The modulated signals are in the frequency range between 100 kHz and 250 kHz. Based on the measurements, a constant channel attenuation can be expected for all four channel bands. The data is differentially encoded and BPSK modulated. The implemented receiver is capable of demodulating all four channels concurrently. Thus, a bit rate of 4.8 kbit is provided for all four transmitters.

The total transmitter unit has a power consumption of only 16.5 mW, the receiver dissipates 400 mW. The high power consumption of the receiver unit is caused by the power dissipation of 270 mW by the ADC device.

The size of the transmitter board is 16 cm^2 while the receiver occupies 29.5 cm^2. Further miniaturization is feasible through integration of the transmitter units as mixed-signal ASIC to achieve the implantable size of a pill.

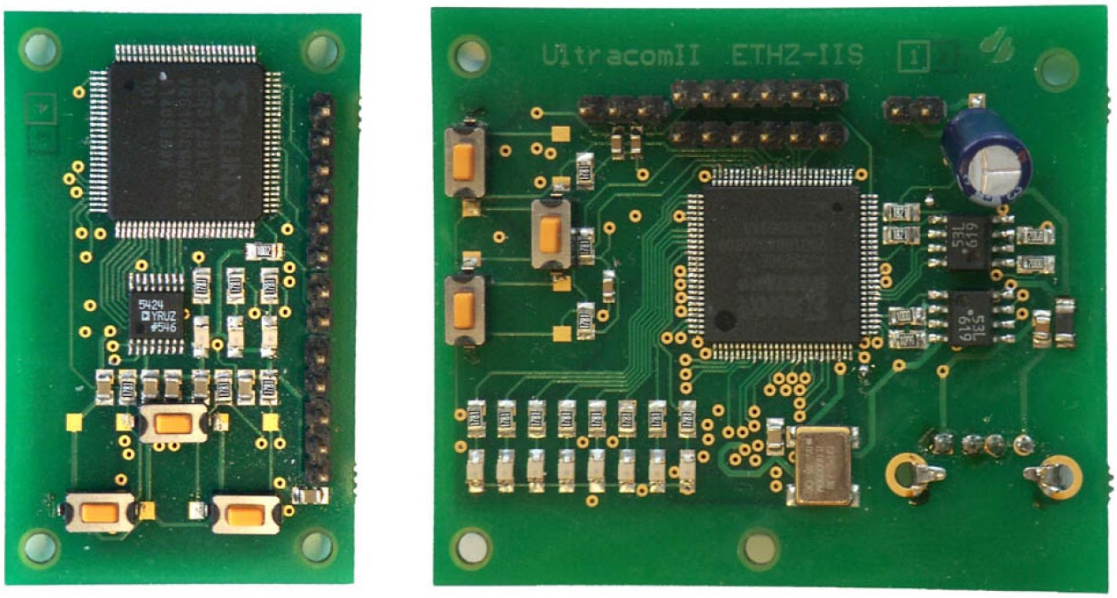

Figure 7.13: Transmitter and receiver PCB: 4 layers, 16 cm^2 respectively 29.5 cm^2.

Table 7.3: Implantable transmitter and receiver demonstrator system.

Parameter	Value
Carrier frequencies	100, 150, 200, 250 kHz
Bite rate	4.8 kbit (per transmitter)
Induced peak current	± 1 mA
Board size	Transmitter:16 cm^2
	Receiver: 29.5 cm^2
Digital complexity	Transmitters: 85 - 91 CPLD macro cells
	Receiver: 2446 FPGA slices
	(18×18 Multipliers: 12, 32-bit RAM blocks: 28)
Power consumption	Transmitter: 16.5 mW (analog 10 mW)
	Receiver: 400 mW (analog 33 mW)

The receiver is able to demodulate the data of a single transmitter up to a distance of 45 cm between the transmitter and receiver electrodes. A 30 dB higher channel attenuation of one transmitter compared to the three other transmitters has still allowed to detect its signal in simulations. Therefore, a distance variations between the transmitters and the receiver of 35 cm will be feasible.

In conclusion, transmission through galvanic coupled pills has been tested successfully in muscle-tissue-simulating liquid. The transmitted sinusoidal signal is detectable at distances up to 45 cm and given different electrode orientations. The attenuation depends on the transmission distance and the length of the conductive part of the electrodes. The longer electrodes performed better than the shorter electrodes.

The low system clock frequency and the low logic complexity allow for an efficient low-power design suitable for implant communication in biomedical monitoring applications, e.g., temperature, SpO_2, and ECG sensors.

Chapter 8

ECG Application with SPIHT Compression

Monitoring applications of human vital functions typically gather large amounts of sensor data which might limit data transmission and storage capacities. Therefore, compression is a reasonable method for data reduction.

Recently, wavelet encoders have become very successful in image processing. Together with subsequent encoders they are used in the newest image compression standards such as JPEG2000 including *Embedded Block Coding with Optimal Truncation (EBCOT)*. The *Set Partitioning In Hierarchical Trees (SPIHT)* algorithm belongs to the next-generation encoders for wavelet-transformed images. SPIHT utilizes inherent redundancy among wavelet coefficients. Such algorithms have been recommended for biomedical data compression, in particular for electrocardiogram (ECG) data [IHP01].

This chapter presents the first VLSI implementation of a modified SPIHT algorithm (MSPIHT). Visually near-lossless compression is obtained for ECG data at compression ratios up to 20:1. The basics of ECG data recoding are introduced in Sec. 8.1. Section. 8.2 gives a brief introduction to wavelet-based algorithms for data compression like SPIHT. The architecture of the modified SPIHT implementation is described in Sec. 8.3, and the resulting VLSI implementation is presented in Sec. 8.4.

8.1 ECG Background and Application

Electrocardiograms (ECG) record the electrical activity generated by the heart. An ECG was originally observed on the human body surface by Waller in 1889 [Wal89]. Einthoven [Ein03] enhanced the measurement technology to what is partially still in use today.

The action potential initiated by the sinu-atrial node causes the heart to perform its function of pumping blood through the circulatory system. As a result of the action potentials, a certain sequence of electrical events occurs. The electrical stimulation of the heart is transmitted through the body and can be observed on the surface of the skin. By placing electrodes to the wrists, ankles, and on the thorax, potential differences can be sensed.

Figure 8.1 shows a typical ECG trace of a regular heartbeat, consisting of a P wave, QRS-complex wave, and T wave. These waves repeat periodically

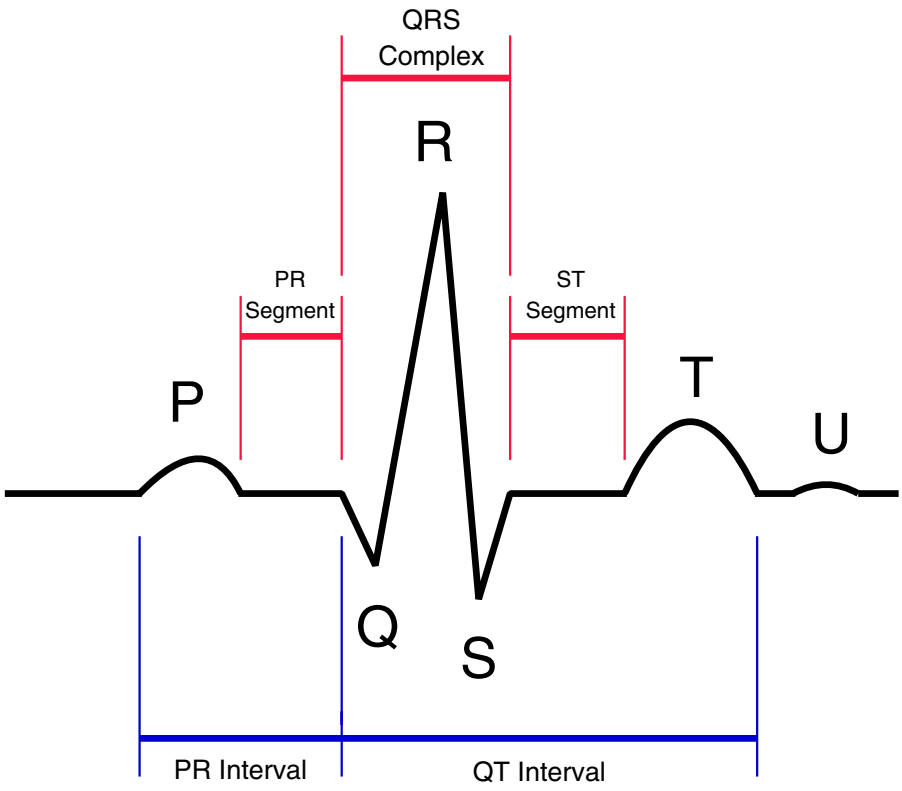

Figure 8.1: Schematic representation of normal ECG trace centered by the QRS complex.

with every heartbeat. An average adult's heart beats about 70-90 times per minute[1] and gives rise to typical between 1 mV and 3 mV peak excursion.

The P wave is the electrical signature of the current that causes atrial contraction. Both the left and right atria contract simultaneously. The relation of the P wave to the QRS complex determines the presence of a heart block. Irregular or absent P waves may indicate arrhythmia. The shape of the P waves may indicate atrial problems.

The QRS complex corresponds to the current that causes the contraction of the left and right ventricles. This current is much stronger than that of the atria. In addition, a greater amount of muscle mass is involved, thus resulting in a greater ECG deflection. The duration of the QRS complex is normally less than or equal to 0.1 seconds. The Q wave, when present, represents the small horizontal (left to right) current as the action potential travels through the interventricular septum. Very wide and deep Q waves do not have a septal origin but indicate a myocardial infarction. The R and S waves indicate contractions of the myocardium itself.

The T wave represents the repolarization of the ventricles. The atrial repolarization wave may be obscured by the QRS complex generally rendering it inobservable. In most cases, the T wave is positive; inverted (also described as negative) T waves can be a sign of disease. The ST segment connects the QRS complex and the T wave.

The U wave is not always observable. Typically, it is quite small and follows the T wave. It is thought to represent repolarization of the papillary muscles or purkinje fibers.

Sufficient details of the ECG trace are a must for correct diagnosis of cardiac arrhythmia and conduction disorders.

[1] If a typical individual lives about 75 years, his or her heart will have cycled over 3.1536 billion times, pumping a total of 0.2107 billion liters of blood.

8.2 Data Compression Algorithms

Data compression offers benefits to many applications in signal and image processing. Especially in picture and video applications, data compression has been very successful, e.g., JPEG, MPEG, JPEG2000. Within the last few years, dedicated compression schemes have also been applied to biomedical signals.

In the particular case of ECG compression, wavelet-based compression has shown superior results in compression performance and complexity leading to very good visual quality [TSY05].

8.2.1 Wavelet-based Data Compression

Figure 8.2 shows a simplified block diagram of a wavelet-based compression for the compression of an image.

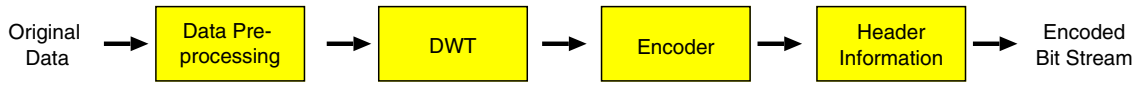

Figure 8.2: Block diagram: Wavelet-based data compression.

The compression consists of four steps:

- Data pre-procession constructs an image with the original data.
- The image is transformed with the discrete wavelet-transform (DWT). The DWT is iteratively applied to the image. Depending on the chosen filter coefficients, the transformation can be lossless or lossy.
- The subsequent encoder compresses the DWT-transformed image. The reduction of the data size is based on first extracting the most significant information of the DWT-transformed image, and discarding the less significant data according to the compression ratio.
- The header information gives the configuration parameters of the compression.

The reverse process of image decompression is shown in Fig. 8.3.

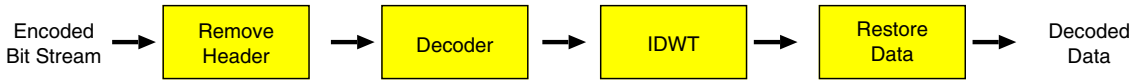

Figure 8.3: Block diagram: Wavelet-based data decompression.

The decompression consists again of four steps:

- The header information instructs the decoder how to reconstruct the data.
- The decoder extracts the encoded data by restoring a truncated DWT-transformed image.
- The inverse discrete wavelet transform (IDWT) reverses the wavelet-transformation.
- From the resulting image, the decoded data is retrieved.

The SPIHT algorithm is one specific encoding algorithm especially suited for ECG signals.

8.2.2 ECG Data Compression using SPIHT

SPIHT is an abbreviation for Set Partitioning In Hierarchical Trees, an encoder algorithm invented by William Pearlman and Amir Said [SP96]. The algorithm is applied to wavelet-transformed images and it has its roots in the Embedded Zerotree Wavelet (EZW) algorithm invented by Shapiro [Sha93]. SPIHT was intended for image compression. A modified version of the SPIHT algorithm (MSPIHT) was introduced in [RFM02] focusing on optimization for FPGA implementation. In [LKP00], the algorithm was further modified for one-dimensional signals and applied to the compression of ECG data. Sharifahmadian [Sha06] adapted SPIHT to multi-channel ECG data. Experiments on selected records from the MIT-BIH arrhythmia database[2] revealed that the proposed codec is significantly more efficient than previous ECG compression schemes [TSY05, RMN05].

[2]Since 1975, the laboratories at MIT and Boston's Beth Israel Hospital (now the Beth Israel Deaconess Medical Center) have collaborated on research in arrhythmia analysis and combined their data into an arrhythmia database http://www.physionet.org/physiobank/database/mitdb

The SPIHT algorithm was devised for two-dimensional image compression. Therefore, one-dimensional ECG data requires preprocessing. The main idea is to cut and align ECG data in order to transform the data into a two-dimensional data set which can be treated as an image.

The process of building a two-dimensional data set of 512×512 pixels can be divided into two steps:

- QRS peak detection
- cutting and alignment of the ECG signal with respect to the QRS complex

These two steps help to enhance the compression performance, since the algorithm works more efficiently with increased line similarity.

The aim of QRS detection is to recognize the QRS-complexes in the ECG data signal. Friesen *et al.* [FJY+90] have presented a comparison of nine QRS detection algorithms, based on the amplitude, the first and second derivatives, and digital filtering. There have been several further investigations on QRS detection algorithms [CP91, RSN97, LT06].

For the QRS detection in this application, two algorithms are compared and implemented. Figure 8.4 shows the principle of the threshold and the derivate methods.

- *Threshold method:* Whenever the ECG signal exceeds a threshold, a subsequent peak is detected. To avoid false detections of the QRS complex, every time a peak is found, a new threshold is calculated. One problem with this method is its sensitivity to glitches or segments

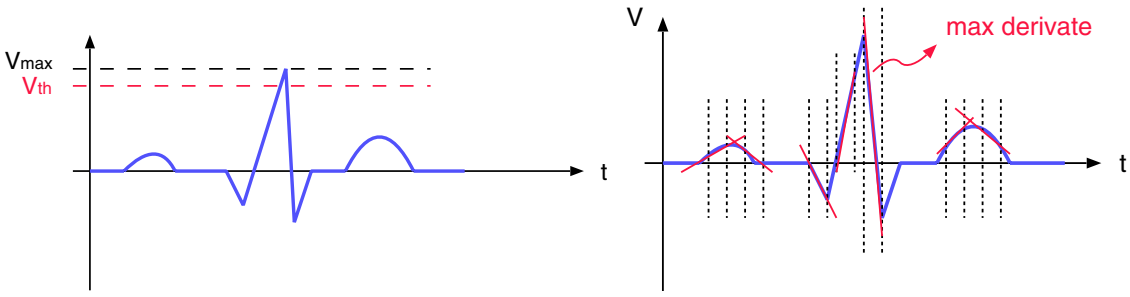

Figure 8.4: Illustration of the two QRS detection methods: Threshold method (left) and derivate method (right).

that are higher than the QRS peak.

- *Derivate method:* The ECG signal is cut into slices and the slope is calculated for every slice as shown in Fig. 8.4. A very steep negative slope identifies the QRS complex.

The QRS detection and the cut & align methods have been verified with simulations. The resulting images are shown in Fig. 8.5. In these ECG samples, the threshold method aligns the traces at the P wave, while the derivate method aligns the traces at the QRS peaks. As the length of the ECG traces may vary, every line of the constructed image is filled with zeros to form 512 samples per line. Therefore, 512 ECG traces are aligned, one below the other, to form an image of 512 × 512 pixels.

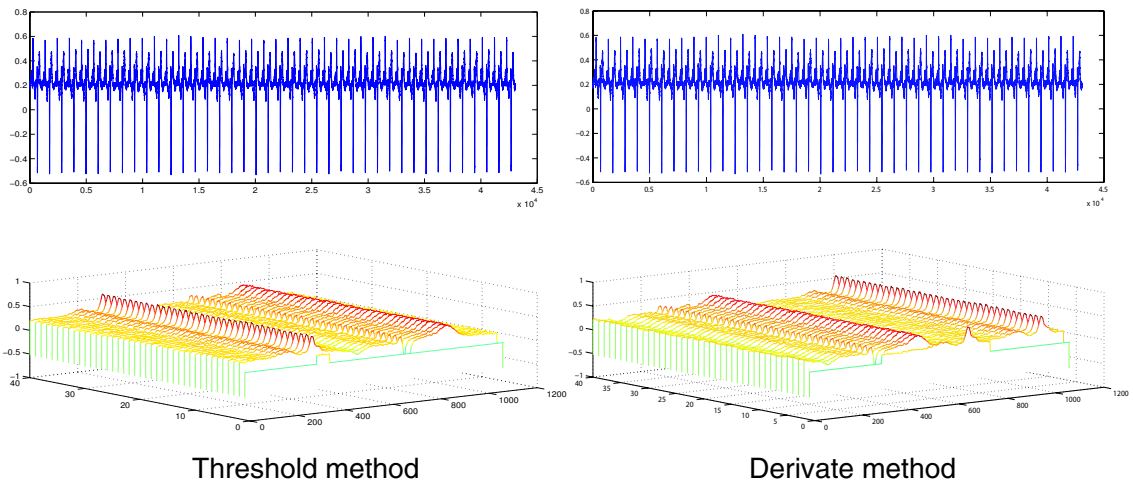

Figure 8.5: Simulation results of the threshold (left) and the derivate (right) methods: ECG signal (top) and cut & aligned ECG data (bottom).

The signal processing has been implemented as shown in Fig. 8.6. DWT and SPIHT encoder are realized in an ASIC, while the remaining units are evaluated in an FPGA.

- Cut & align: The continuous ECG data consists of one-dimensional signal traces representing one heart beat each. After detecting the QRS complex, the data stream is cut and the traces are aligned according to peaks (with zero padding of short heart beats) to form the two-dimensional data set (Fig. 8.7a).
- Segmentation into blocks of M × M pixels
- Discrete wavelet transform (DWT): Wavelet transformation is applied iteratively. The result is a transformed image in pyramidal form as shown in Fig. 8.7b for 3 decomposition levels after 3 wavelet transformations. The approach by Daubechies [DS98] was implemented with bi-orthogonal 2.2 wavelets (bior 2.2).
- MSPIHT encoding of the wavelet-transformed image into an embedded bit stream (Fig. 8.7c).
- Generation of header information.

For reconstruction of the ECG signal, the following parameters have to be attached as a header at the end of the encoding process:

- wavelet decomposition level
- size N of the N × N image
- beat length information (N values)
- size M for segmentation into blocks of M × M pixels

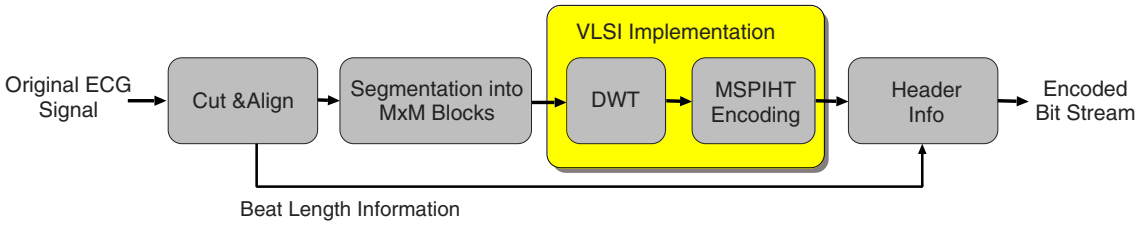

Figure 8.6: Block diagram of a WT-based ECG compression method using the SPIHT algorithm.

8.2.3 SPIHT Algorithm

Since most of the energy in the wavelet-transformed images of cut & aligned ECG signals is concentrated in the low frequency coefficients, the SPIHT algorithm is especially well suited.

The SPIHT algorithm is based on three concepts:

1. The wavelet-transformed image (Fig. 8.8a) contains spatial children-parent relationships among the coefficients as shown in Fig. 8.8b. This structure can be represented by a hierarchical tree called a spatial orientation tree (Fig. 8.8c).

2. The spatial orientation tree is descended for the significance detection of every wavelet-transformed image coefficient.

3. Similarity between coefficients caused by their parent-child relationship allows insignificant coefficients to be flagged and the significant coefficients to be transmitted first.

Compression is realized in two ways: First, because the transformed image elements are partially ordered by magnitude, the leading '0' bits and the first '1' of any coefficient do not need to be transmitted, since they can be reconstructed. Secondly, the SPIHT algorithm produces a bit stream in such a way that the encoding can be stopped at any time while still allowing the

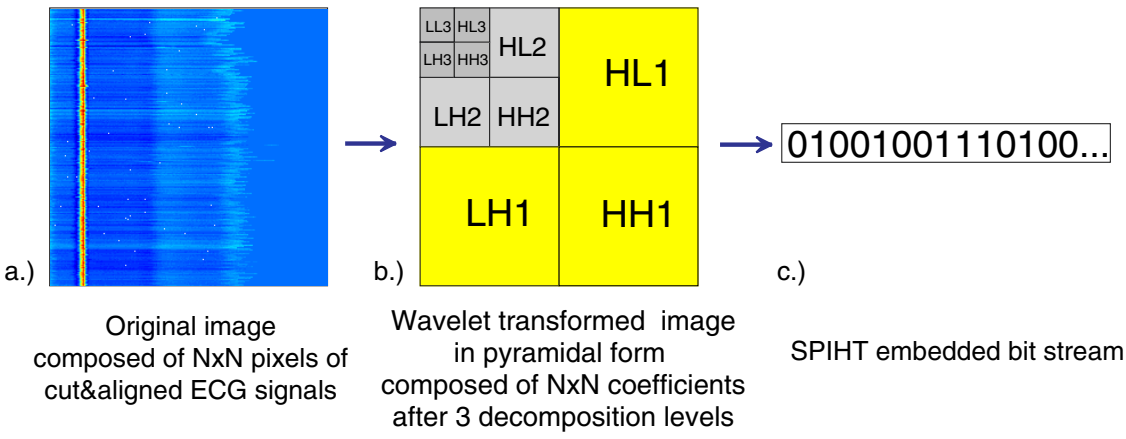

Figure 8.7: Overview of data representations after image composition, wavelet transformation and SPIHT encoding.

reconstruction of the image. If the transformed image is fully encoded and decoded, the reconstruction is lossless.

Spatial Orientation Tree

The *spatial orientation tree* is chosen to represent the transformed image. Each node of the tree corresponds to a coefficient $c_{(i,j)}$, where (i, j) indicate the coordinates of that coefficient. Its direct descendants represent the same spatial orientation in the next wavelet level, which provides a more detailed resolution. Therefore, a node has either no direct descendants (the leaves) or four, which form a group of 2×2 adjacent coordinates. The only exception is the LL-band of the highest wavelet level, in which the coordinates are marked with a star. Nodes at the same level match the coefficients at the same decomposition level of the wavelet transformed image.

The sorting algorithm partitions the coordinates (i, j) of the wavelet trans-

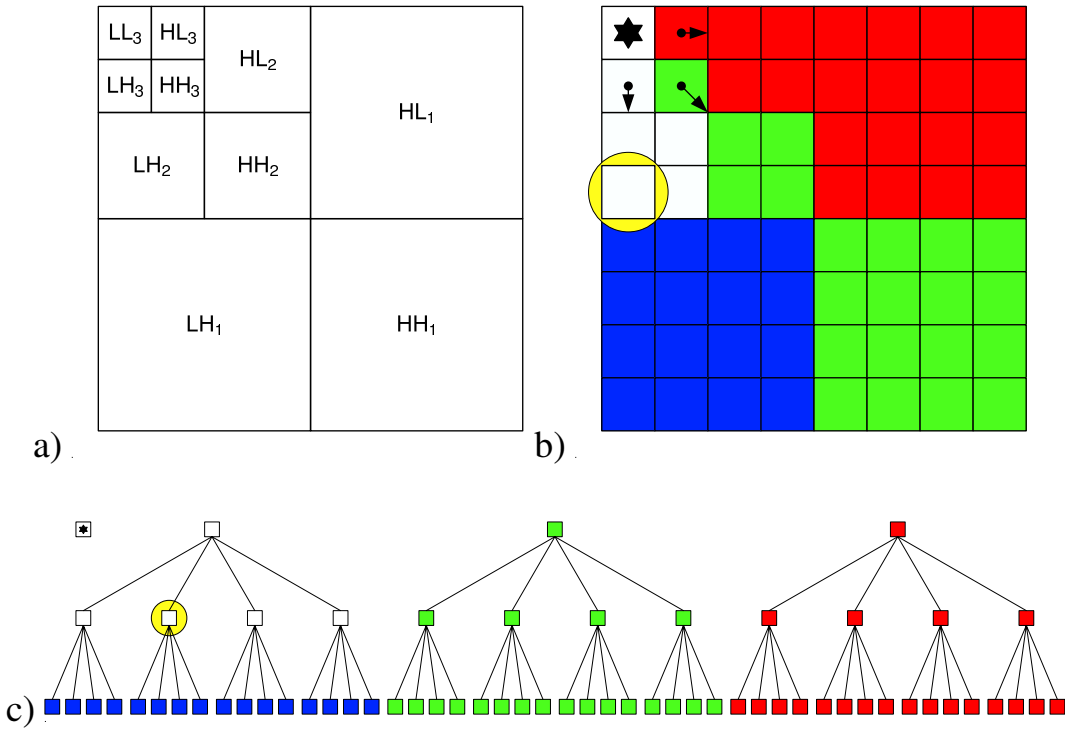

Figure 8.8: Building the spatial orientation tree: (a) pyramidal form created by the wavelet transformation, (b) relationship between descendants, (c) transformed image represented as tree.

formed image coefficients into subsets $\mathcal{T}$. The function

$$S_k(\mathcal{T}) = \begin{cases} 1, & \max_{(i,j)\in\mathcal{T}}\{|c_{(i,j)}|\} \geq 2^k \\ 0, & \text{else} \end{cases} \tag{8.1}$$

is used to indicate the significance of the subset $\mathcal{T}$ of coordinates, where 2^k determines the threshold. The wavelet-transformed image is layered into bit planes in so far as the k-th bits of all wavelet coefficients constitute a bit plane. Therefore, the significance detection is a process that operates bit plane by bit plane, starting from the most significant plane.

If $S_k(\mathcal{T}) = 1$, the subset $\mathcal{T}$ is divided into new subsets. This procedure is continued until every coefficient is identified as significant or insignificant.

Similarities between Coefficients

If a coefficient in a given wavelet level is insignificant, it is very likely that the coefficients in the lower levels at the same spatial location are also insignificant. With the tree structure based on the pyramidal form of the wavelet transform, those two characteristics can be exploited.

The following sets of coordinates are used in the algorithm:

- $\mathcal{H}$ is the set of coordinates of the tree roots, which are the nodes in the highest wavelet level
- $O(i,j) = \{(2i,2j),(2i,2j+1),(2i+1,2j),(2i+1,2j+1)\}$ is the set of coordinates of the children of node (i,j)
- $\mathcal{D}(i,j)$ is the set of all descendants of node (i,j)
- $\mathcal{L}(i,j) = \mathcal{D}(i,j)\backslash O(i,j)$ is the set of descendants excluding the children of node (i,j)

To store the significance information, three ordered lists are used. In the *list of insignificant coordinates* (*LIC*) and the *list of significant coordinates* (*LSC*), each entry is comprised of the coordinates (i,j) of a coefficient. The entries in the *list of insignificant sets* (*LIS*) also contain the coordinates (i,j), but in contrast to the entries of *LIC* and *LSC*, they represent the roots of subsets. Additionally, the entries in the *LIS* include the flag D or L, which states whether they represent the set $\mathcal{D}(i,j)$ or $\mathcal{L}(i,j)$.

Execution of the SPIHT Algorithm

Initialization:

1. The wavelet-transformed image is searched for the largest magnitude which defines the bit plane k with the highest significance (to get rid of leading '0').
2. The lists are initialized: The empty set is assigned to the *LSC*, since no coefficient is yet significant. The tree roots $\mathcal{H}$ are added to the *LIC* and those with descendants to the *LIS*.

Sorting Pass

1. Coefficients of coordinates in the *LIC* are tested for significance according to Eq. (8.1) and correspondingly moved to the *LSC* list.
2. Subtrees defined by the entries in the *LIS* are searched for significant coefficients. Those found to be significant, including their siblings and ancestors but not the roots, are added either to *LSC* or *LIC*.
3. New subtrees are defined in which significant coefficients were found.

Refinement Pass

1. Only the coordinates of the k-th bit plane which are significant are transmitted.
2. If it was not the least significant bit plane, k is decremented by one and the algorithm begins with another sorting pass.

8.2.4 Modified SPIHT Algorithm (MSPIHT)

In [RFM02, Fey02] the MSPIHT algorithm optimized for an efficient FPGA implementation was presented. The main modifications from the original SPIHT algorithm concern the memory structure and the refinement pass. The SPIHT algorithm, designed mainly for SW implementation, uses dynamic structures, such as linked lists. On the contrary, the MSPIHT algorithm uses static bitmaps which represent the significant information.

Algorithm 1 Modified SPIHT Algorithm part one.

Initialization

output $k = \lfloor \log_2(\max_{\{(i,j)|0 \le i,j<N\}} |c_{(i,j)}|) \rfloor$
foreach $0 \le i, j \le N-1$ **do**
    $LSC(i,j) = 0$
    $LIC(i,j) = \begin{cases} 1, & \text{if } (i,j) \in \mathcal{H} \\ 0, & \text{else} \end{cases}$
foreach $0 \le i, j \le \frac{N}{2} - 1$ **do**
    $LIS(i,j) = \begin{cases} D, & \text{if } (i,j) \in \mathcal{H} \text{ and } O(i,j) \neq \emptyset \\ 0, & \text{else} \end{cases}$

Refinement And Sorting Phase For List *LIC*

for $i = 0$ **to** $N-1$ **do**
    for $j = 0$ **to** $N-1$ **do**
        if $LSC(i,j) = 1$ **then**
            output the k-th bit of $|c_{(i,j)}|$
        end if
        if $LIC(i,j) = 1$ **then**
            output $S_k(i,j)$
            if $S_k(i,j) = 1$ **then**
                $LSC(i,j) = 1$
                $LIC(i,j) = 0$
                output the sign of $c_{(i,j)}$
            end if
        end if
    end for
end for

Algorithm 2 Modified SPIHT Algorithm part two.

Sorting Phase For List LIS
for $i = 0$ **to** $\frac{N}{2} - 1$ **do**
  for $j = 0$ **to** $\frac{N}{2} - 1$ **do**
    if $LIS(i, j) = D$ **then**
      output $S_k(\mathcal{D}(i, j))$
      if $S_k(\mathcal{D}(i, j)) = 1$ **then**
        foreach $(e, f) \in O(i, j)$ **do**
          output $S_k(e, f)$
          if $S_k(e, f) = 1$ **then**
            $LSC(e, f) = 1$
            output the sign of $c_{(e,f)}$
          else
            $LIC(e, f) = 1$
          end if
        if $\mathcal{L}(i, j) \neq \emptyset$ **then**
          $LIS(i, j) = L$
        else
          $LIS(i, j) = 0$
        end if
      end if
    end if
    if $LIS(i, j) = L$ **then**
      output $S_k(\mathcal{L}(i, j))$
      if $S_k(\mathcal{L}(i, j)) = 1$ **then**
        foreach $(e, f) \in O(i, j)$ **do**
          $LIS(e, f) = D$
          $LIS(i, j) = 0$
      end if
    end if
  end for
end for
if $k = 0$ **then**
  return
else
  decrement k by 1
  goto step 7
end if

The second modification concerns the refinement pass. The original SPIHT algorithm transmits only the elements not added to the *LSC* in the current sorting pass. In the MSPIHT algorithm, the information regarding which elements were added last to the *LSC* is not available. Therefore, the refinement pass is executed before the sorting pass. No extra memory is needed and no additional computation has to be executed.

Both changes are included in the pseudo code listing of Algorithm 1.

8.3 MSPIHT Architecture

Figure 8.9 shows the major functional blocks and the interface to external devices. The aligned ECG data is received from the *Data source* by the *Data-In* unit and stored in the memory *Image 0* or *Image 1*, which are used as a ping-pong buffer. Once an image is complete, the image compression process is started while new ECG data is written to the other memory. The compressed data is output to the *Data sink*. The third memory *Lists* is used to store the lists of the MSPIHT algorithm. Due to chip area constraints, on-chip memory is limited. Memory access and intermediate data storage is the bottleneck of the design and is shared among all blocks through the *Arbiter*.

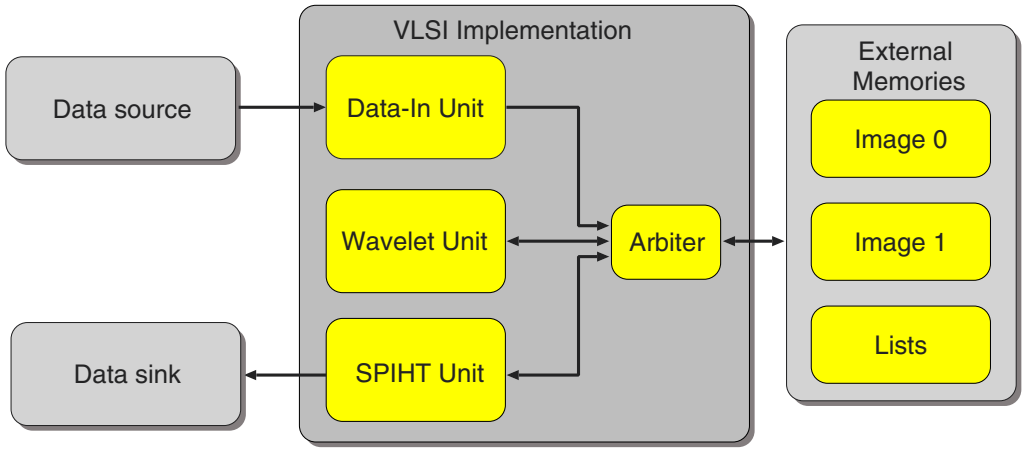

Figure 8.9: System overview consisting of the SoC with Arbiter, Data-In, Wavelet, and SPIHT units. Three external memory blocks are used to store images and lists.

8.3.1 Memory Considerations

List Storage in the SPIHT Algorithm

The SPIHT algorithm stores its ordering information in the three lists *LIC*, *LSC* and *LIS*.

LIC and *LSC* can contain at most all image coefficients. With an image of size $N \times N$ (N assumed as a power of 2 in the range of 4 to 9 and of $log_2 N$ bits) and since the two lists are mutually exclusive ($LIC \cap LSC = \emptyset$), the total memory consumption of the two lists *LIC* and *LSC* is

$$M_{LIC+LSC} = N^2 \cdot 2 \cdot \log_2 N \qquad [\text{bits}]. \tag{8.2}$$

LIS contains at most all lowest-level parents, i.e. all 2nd-lowest-level coordinates. Therefore, *LIS* holds at most $\left(\frac{N}{2}\right)^2 - \left(\frac{N}{4}\right)^2 = \frac{3}{16}N^2$ entries. Beside the coordinates (i, j), the entries in *LIS* also contain the flag bit indicating *D* or *L*. Since the coordinate range is also limited to $\frac{N}{2}$, the total memory needed for *LIS* is

$$M_{LIS} = \frac{3}{16}N^2 \cdot \left(2 \cdot \log_2 \frac{N}{2} + 1\right) \qquad [\text{bits}]. \tag{8.3}$$

List Storage in the Modified SPIHT Algorithm

The bitmap structures of the MSPIHT algorithm only need to hold the significance, but not the ordering information.

LIC and *LSC* can contain N^2 entries each. For each coefficient $(i, j) \in LIC$ or $(i, j) \in LSC$ or $(i, j) \notin LIC \cup LSC$ holds. Thus, both bitmaps use 1 bit per entry to represent whether the coefficient is entered in the bitmap or not. Therefore, *LIC* and *LSC* require

$$M_{LIC+LSC} = 2 \cdot N^2 \qquad [\text{bits}]. \tag{8.4}$$

The bitmap for *LIS* has to cover all coefficients that are not leaves. Hence, the bitmap is of size $\frac{N}{2} \times \frac{N}{2}$. Two bits per entry are provided to represent the flags *D*, *L* and neither. Therefore,

$$M_{LIS} = 2 \cdot \frac{N^2}{4} \qquad [\text{bits}] \tag{8.5}$$

are sufficient to store *LIS*.

Table 8.1: Memory requirements: Image size versus memory needed for the two SPIHT versions.

Image size [bits × bits]	SPIHT lists [bits]	MSPIHT lists [bits]	SPIHT total [bits]	MSPIHT total [bits]
16×16	2'384	640	10'576	8'832
32×32	11'968	2'560	44'736	35'328
64×64	57'600	10'240	188'672	141'312
128×128	269'312	40'960	793'600	565'248
256×256	1'232'896	163'840	3'330'048	2'260'992
512×512	5'554'176	655'360	13'942'784	9'043'968

Image Memories for SPIHT and MSPIHT

For an image of size $N \times N$ and bit depth d, the two ping-pong buffers require

$$M_{image} = N^2 \cdot 2 \cdot d \qquad [\text{bits}] \tag{8.6}$$

From equations (8.2), (8.3) and (8.6), respectively (8.4), (8.5) and (8.6), the total memory requirements can be calculated for SPIHT and MSPIHT. With a bit-depth of $d = 16$ bits, the memory demands are presented in Tab. 8.1. With the maximal given die area of $3.52\,\text{mm}^2$, only image sizes up to size 32×32 could be implemented completely on chip.

8.3.2 MSPIHT Unit

With lower memory requirements, the MSPIHT algorithm was chosen for implementation. In Fig. 8.10 the block diagram of the MSPIHT realization is shown.

- *FSM blocks:* The main finite state machine (FSM) controls the procedure of the algorithm. This includes the start and end of the algorithm, scheduling of the initialization, refinement, and sorting phases, as well as control of the iteration loop counter.

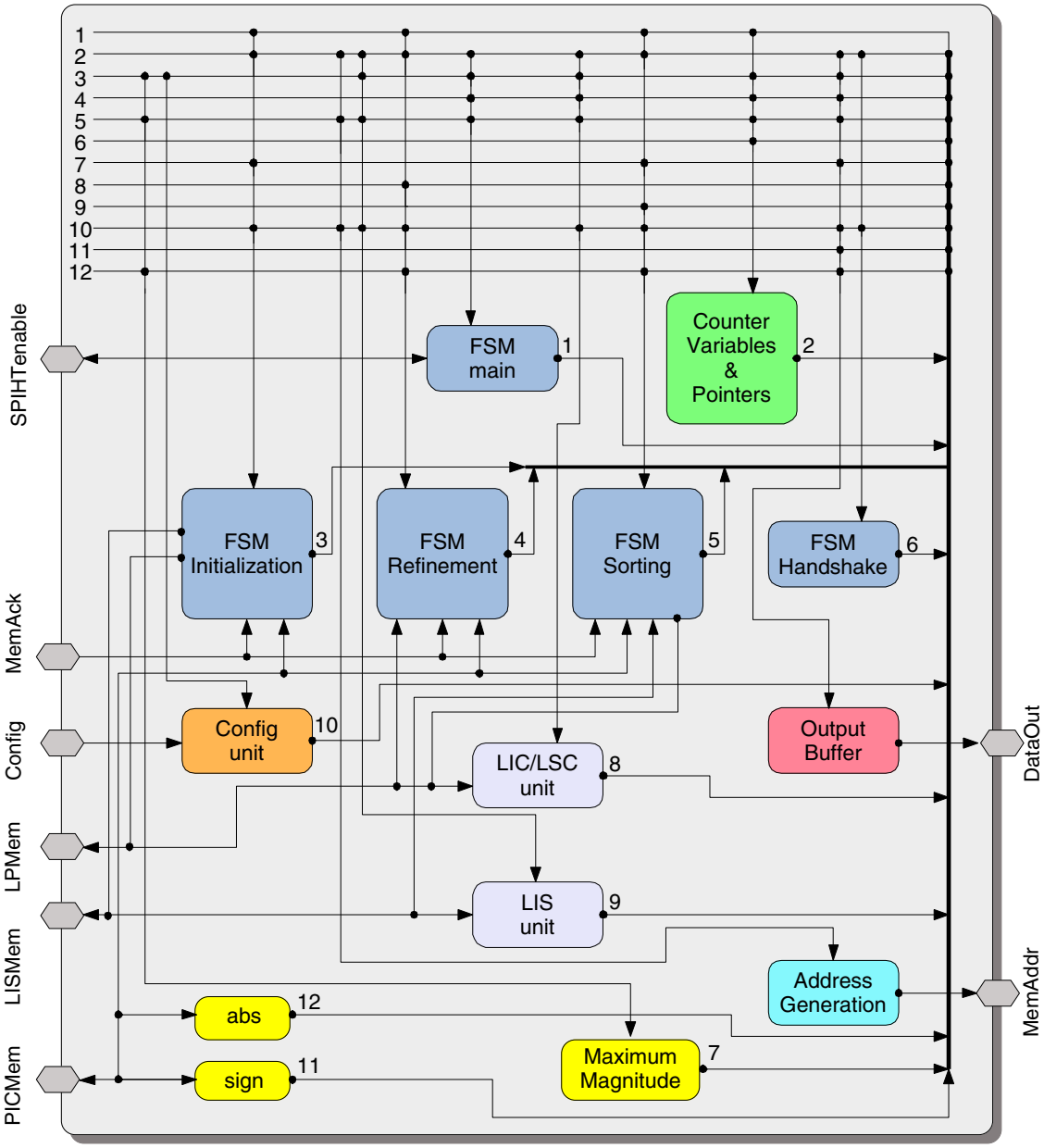

Figure 8.10: Block diagram of SPIHT implementation. All blocks are interconnected through the interconnection matrix shown on top. Output signals of the blocks are marked by the number of the row of the interconnection matrix to which they connect.

Each major phase of the algorithm is controlled by its own FSM, namely *initialization*, *refinement*, and *sorting*. The *handshake* FSM is used to control the output of the coded data bits.

- *Counter Variables & Pointers* and *Address Generation:* These two blocks provide hardware resources used by multiple FSM's.
- *Config unit:* Three registers store the three configuration variables: image size, wavelet level, and number of bits to be transmitted per image.
- *Output Buffer:* A ring buffer to facilitate the output of the coded bits.
- *LIS* and *LIC/LSC units:* Each unit contains two 16 bit buffers to store a 16 bit word read from the external memory and the modified 16 bit word to be written back. This allows a significant reduction of memory write operations which need only to be executed if the word was modified.
- *Abs, Sign* and *Maximum Magnitude:* These blocks implement the basic functions needed for the algorithm: Calculation of absolute values of coefficients, extraction of the sign, and selection of the largest coefficient of a set.

8.4 Prototype System Realization

The prototype consists of the three major units

- Analog front-end: ECG signal acquisition
- Digital unit board: FPGA and SRAM for signal processing including cut & align and data storage units
- VLSI implementation of the MSPIHT algorithm

8.4.1 Analog Front-End

The ECG signal can be sensed by electrodes on the skin surface. The ECG measurements involve the detection of very weak signals. The electrical po-

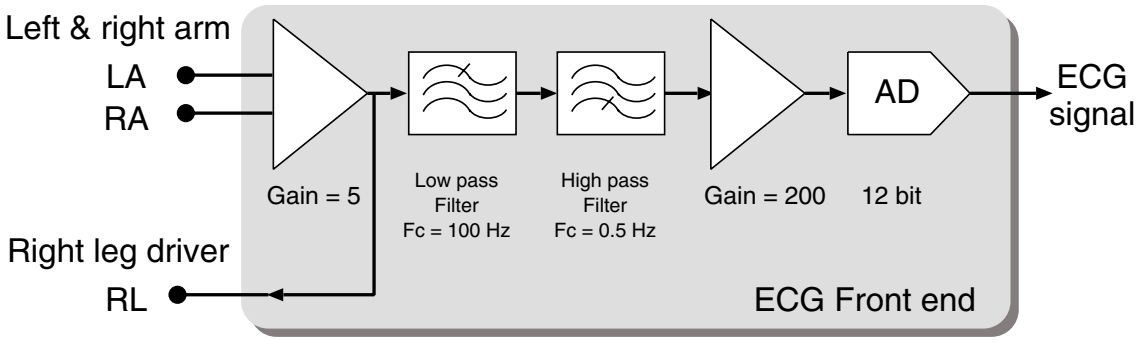

Figure 8.11: ECG front-end: ECG detection electrodes *LA* and *RA* and right leg driver *RL*.

tential is typically between 1 mV and 3 mV. Therefore, low-noise amplifiers are required to increase the signal strength.

The front-end prototype, designed to acquire the ECG data from a subject, uses the *Right Leg Driven* method in order to eliminate the common-mode interference. An ECG front-end structure is shown in Fig. 8.11. The two electrodes *LA* and *RA* are placed near the shoulders, and the third electrode *RL* is placed on the right leg. The two signals from the left arm *LA* and from the right arm *RA* are amplified by the differential amplifier. The right leg channel *RL* is fed back to the body so that the noise is canceled.

For the recorded ECG signal spectrum, a signal bandwidth of 100 Hz is required. A high-pass ($f_0 = 0.5\,Hz$) filter and a low-pass ($f_0 = 100\,Hz$) filter are implemented to reduce out of band noise. An instrumentation amplifier is realized with three low noise amplifiers (LNA) and a total gain of 1000.

Measurements have shown that an acceptable ECG waveform is obtained using the *Right Leg Driven* method.

Table 8.2: Analog ECG front-end design parameters.

Parameter	Implementation
Method	Right Leg Driven (3 ECG electrode contacts)
Gain	1000 (instrumentation amplifier with gain 5)
Bandwidth	0.5 Hz - 100 Hz
ADC	12 bit, 200 Hz sampling rate

8.4.2 VLSI Implementation

The VLSI implementation of the MSPIHT algorithm processes images of up to 512×512 pixels. The presented implementation allows between 1 and 9 decomposition levels.

The DWT unit operates with the on-chip RAM, where a single line of 512 pixels are stored. Simple biorthogonal 5/3 (bior 2.2) wavelets were implemented, since they lead to good results for a broad range of applications (ECG and images). As the wavelet-filter coefficients are powers of 2, they are very suitable for efficient hardware realizations.

The embedded bit stream allows truncation at any position. The coefficients of the transformed image are transmitted in order of their information significance, which is correlated with the magnitude of the coefficient. Furthermore, the ordering information which has to be transmitted to the decoder

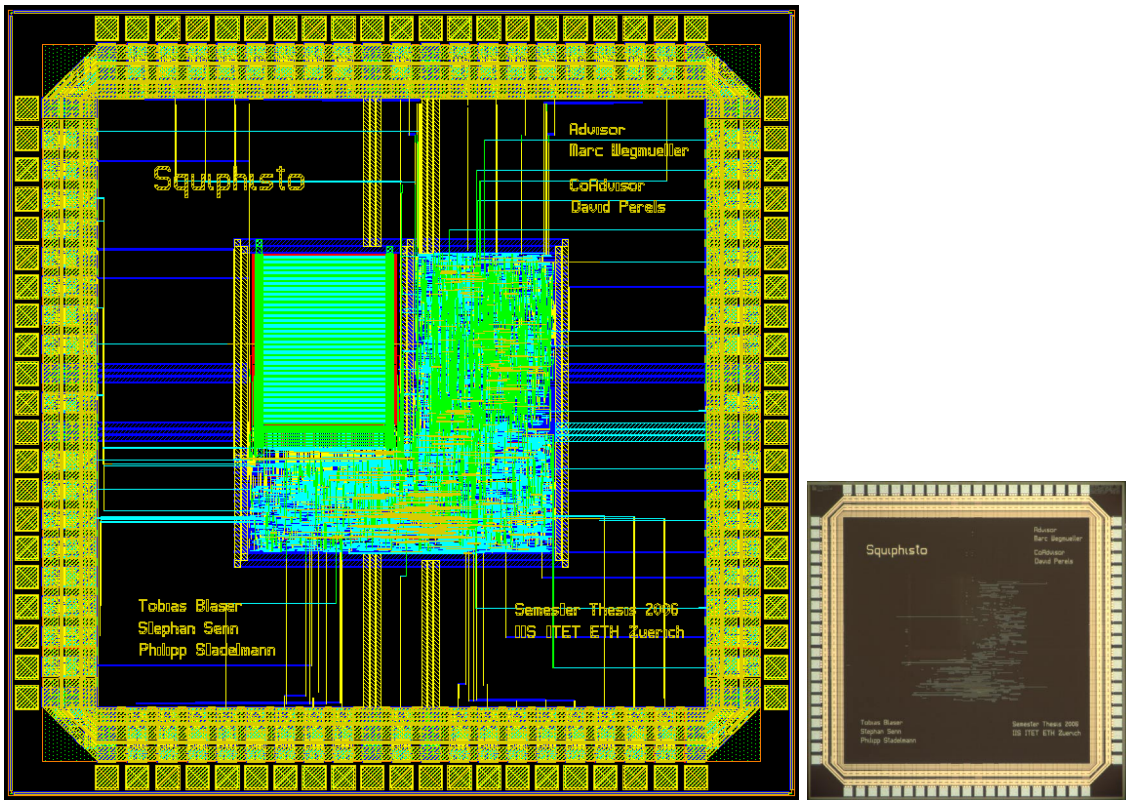

Figure 8.12: ASIC layout and image of the VLSI SPIHT implementation in UMC 0.25 µm.

Table 8.3: Overview of implementation results.

Parameter	Implementation
Process	UMC 0.25 µm (5 metal, 1 poly)
Clock	1 clock domain @ maximal 75 MHz
Core area	about 0.877 mm^2
Complexity	31 kGE (MSPIHT: 7.3 kGE, DWT: 20 kGE)
I/O pads	68
Power pads	16
Supply voltage core	2.5 V
Supply voltage I/O	2.5 .. 3.3 V
Power consumption	57.75 mW @ 75 MHz, 77µW @ 100 kHz
Testability	16 scan chains
Test coverage	97.7% with 1069 scan test patterns
Internal memory	8 kbit
External memory	3×4 Mbit
Original image	max. 512×512 times 11 bit

is minimized. Above all, the embedded bit stream produced by the encoder makes progressive image transmission possible.

The ASIC (Fig. 8.12) was implemented in UMC 0.25 µm (5 metal, 1 poly layer) CMOS process (see Tab. 8.3). The system occupies 0.877 mm^2 silicon area. The ASIC runs typically 0.35 s to process a 512×512 image at the maximal clock frequency of 75 MHz. For real-time processing of ECG data with an average heart beat of 100 beats/min, a 100 kHz clock frequency is sufficient for low-power applications.

8.5 Results

Performance evaluation was done with 8 bit gray-scale images of 512×512 pixels and ECG data of 11 bit resolution, resulting in 512 samples per beat. Full decomposition level of the DWT is not necessary; with more than 5 wavelet-levels satisfying results are achieved.

Experimental results have shown that the compression efficiency of the MSPIHT algorithm decreases with smaller image blocks. Compression ratios are reduced by a factor of three for blocks of 32×32 pixels compared to one single block of 512×512 pixels.

MSPIHT compression ratios of up to 20:1 for ECG signals lead to acceptable results for visual inspection (see example in Fig. 8.13). Further compression may lead to false diagnosis through visual inspection due to vanishing details.

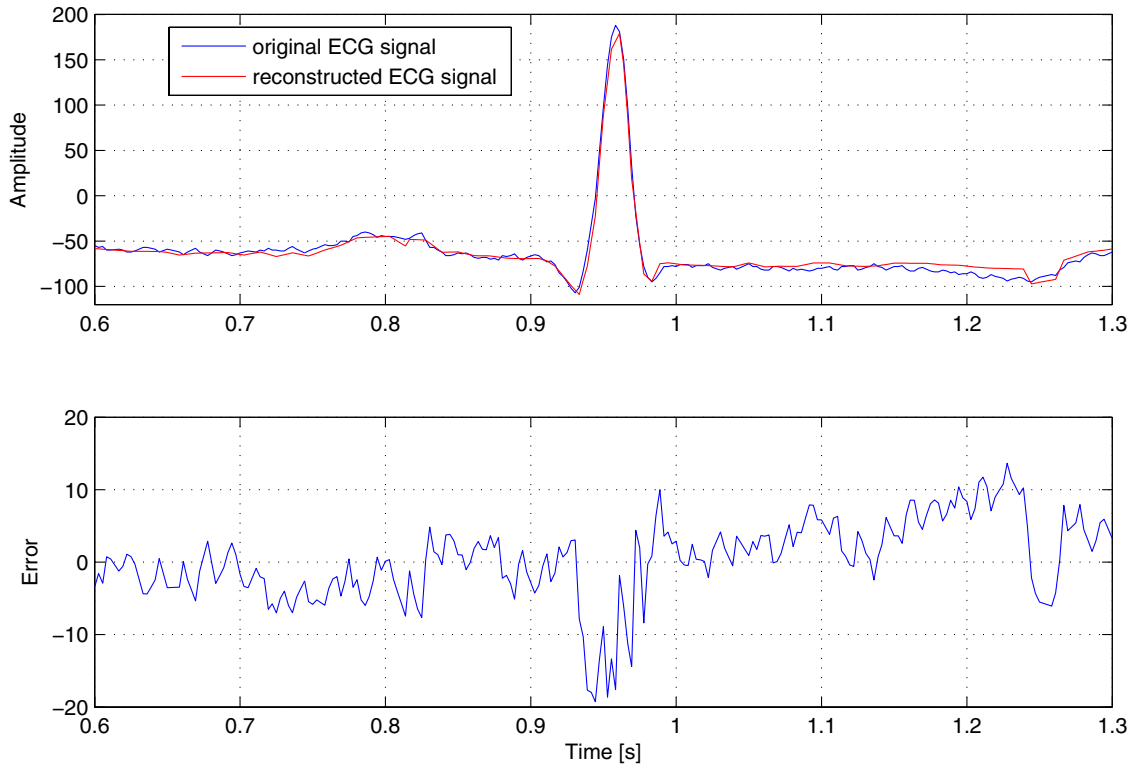

Figure 8.13: Decoded 20:1 compressed ECG signal, based on a 5 wavelet-level transformed image compared to its original.

Chapter 9

Summary and Conclusions

Novel communication technologies for data exchange between biomedical on-body and implanted sensors are emerging. Intra-body communication utilizes the human body as part of the transmission system; the body becomes the transmission medium for electrical signals. Among the body transmission principles, the method of galvanic coupling is the most promising principle for interconnecting future biomedical sensors. Alternating currents are coupled into the human tissue by two electrodes and detected at other body locations as a potential difference by a second pair of electrodes. The induced current frequencies have been kept below 1 MHz, and the peak current is limited to 1 mA.

Viability of Intra-Body Communication

This thesis has shown that it is no longer science fiction to transmit data by means of electrical currents through human tissue. The induced currents are absolutely harmless for human beings.

The clinical trial among 20 subjects confirmed the feasibility of the new technology to transmit electrical signals through the human body. Even among subjects with a wide range of body parameters, stable transmissions have been obtained in particular on the thorax. Nevertheless, the measurements have shown large differences in attenuation at different body locations. Especially the thorax showed excellent transmission characteristics,

with typical attenuation between 50 dB and 60 dB, while the extremities and joints limited the transmission over larger distances among the majority of the subjects. Axillary joints increased the attenuation up to 8 dB. Improvements have been seen during body activity. The lower attenuation has been explained by the change of the skin layer condition due to transpiration.

The channel variability is related to the body mass parameters and the actual condition of the human tissue layers. Thus, the total body water content and the influence of wet skin during transpiration have been identified as the most significant parameters that positively affect the transmission characteristics. The ideal subject for signal transmission in the frequency range of 100 kHz to 500 kHz features a high muscle mass above 45% and a high inter-cellular body water value above 60%. A small skin fold thickness influences the communication positively.

Intra-body communication units allow data transfers between on-body and implantable sensor devices. The reduction to simple transmission schemes like phase-shift-keying and a system architecture focusing on low-power and a future mixed-signal integration have enabled the realization of the intra-body transceivers. A maximal data rate of 64 kbit/s has been achieved with a carrier frequency of 256 kHz and signal modulation by QPSK.

The power consumption of the final intra-body communication transmitter is less than 20 mW, when realized with discrete low-power devices and a low-power CPLD for the integration of the digital units. The analog output driver dissipates 11 mW. Further improvements can be expected with a fully integrated mixed-signal ASIC. The power consumption of the digital units processing at a system frequency below 1 MHz is thereby expected to drop below 1 mW. Eventually, this will enable long-term sensor devices operated by miniaturized low-cost batteries, comparable to state-of-the-art hearing aids.

The presented prototypes and ASIC integrations for on-body and implanted intra-body transmission show the first intra-body transceiver implementations using digital modulation schemes for biomedical sensor applications. On the thorax, various locations are applicable among the entire group of subjects. On the extremities only short-range transmission is reliable. Therefore, the relay functionality of the transceiver is required to transmit sensor data in short-distance transmission steps beyond the areas of large attenuation.

The upper bound of the network size is given by the channel capacity. Thus

far, a test system has been implemented with four transmitters and one receiver. Additional channels of different carrier frequencies can be defined, limited only by the available transmission bandwidth. Furthermore, additional transmission links can be assigned by time-division multiplexing. However, this extension will reduce the data rate of each data link operating on the same carrier frequency accordingly.

Further research might investigate carrier frequencies above 1 MHz. However, the higher the frequency, the more transmitted power is radiated through the air. Thus, the influence of the human body decreases and the signal transmission no longer benefits from the human body proximity. Eventually, transmissions at RF frequencies will be purely wireless transmissions through air. As an additional drawback, the power consumption will increase with higher frequencies.

Future Applications

Based on the body proximity and the usage of human tissue as a transmission medium, biomedical applications have been the initial field of interest. Applications are feasible using on-body or implanted devices. The proposed intra-body communication technology offers substantially increased freedom and flexibility during monitoring of the long-term and risk patients, e.g., long-term ECG or pulse oximetry monitoring. The achieved transmission possibilities enable the envisioned biomedical sensor applications. Applications with higher data rate requirements are not feasible. But, solutions are provided by data reduction or compression.

In addition to data recording and transmission by monitoring sensors, signal application and the control of biological and pharmacological processes will be enabled by body transmission technology. Therefore, intra-body communication shall be used for local medication and biological cell stimulation by smart implants.

Indeed, the technology provides benefits to many applications involving body proximity. The list of future devices is long. In monitoring and identification applications, intra-body communication increases the comfort and possibilities for the users. Human-operated tools equipped with an identification interface allow the authentication of the user. Furthermore, the technology can be integrated into consumer electronics, e.g., wireless headsets.

Concluding Remarks

The presented intra-body communication transceivers have achieved the highest data transmission rates deploying galvanic coupling. In the future, the novel transmission technology will mature toward an advanced body transmission communication technology.

The limits of intra-body communication are mainly given by the regulative limitations and the signal transmission feasibilities. Derived solutions for improved signal transmission through complex tissue structures like joints and organs and more reliable data transmission by data encoding will enhance future intra-body communication devices. Many processes in the human tissue have not yet been fully explained by means of the numerical models. Enlarged simulation models of more detailed body structures could provide more detailed explanations of the involved cell structures and resulting current distributions.

Alternative technologies like Bluetooth, Zig-bee, or recently emerging Ultra-Wide-Band (UWB) wireless transceiver systems have the drawback of higher power consumption and frequencies in the GHz range. These systems have not initially targeted applications in close body proximity and the exposure reactions of human tissue have not exhaustively been investigated; the body is considered as a lossy medium. By contrast, intra-body communication utilizes the dielectric body parameters and benefits by the presence of human tissue in respect of the low-frequency low-power transmission.

Particularly in medical health care environments, the trend is toward an increasing number of technical facilities, sensor units, and monitoring devices. Intra-body communications has a high potential to advance to a valuable candidate for novel communication technology in clinical body-transmission-based surveillance systems with respect to growing sensor network complexity and the increasing long-term monitoring.

Acronyms

AC ..... Alternating Current
ALU..... Arithmetic Logic Unit
ASIC..... Application Specific Integrated Circuit
ATM..... Automated Teller Machine
BER..... Bit Error Rate
BIA..... Bioelectrical Impedance Analysis
BPSK..... Binary Phase Shift Keying
CDMA..... Code Division Multiple Access
CPLD..... Complex Programmable Logic Device
CMOS..... Complementary Metal-Oxide Semiconductor
DBPSK..... Differential Binary Phase Shift Keying
DC..... Direct Current
DWT..... Discrete Wavelet Transform
ECG..... Electrocardiography
ECW..... Extra-Cellular Water
EEG..... Electroencephalography
EEPROM... Electrically Erasable Read Only Memory
EIT..... Electrical Impedance Tomography
EMG..... Electromyography
EOG..... Electrooculography
FES..... Functional Electrical Stimulation
FDMA..... Frequency Division Multiple Access
FDTD..... Finite-Difference Time-Domain method

FFT ..... Fast Fourier Transformation
FFM..... Fat Free Mass
FIFO ..... First-In First-Out
FPGA ..... Field-Programmable Gate Array
IC..... Integrated Circuit
ICW..... Intra-Cellular Water
IrDA ..... Infrared Data Association
IWT..... Inverse Wavelet Transform
JTAG..... Joint Test Action Group
LFSR..... Linear Feedback Shift Register
LNA..... Low Noise Amplifier
LSB ..... Least Significant Bit
LUT..... Look-Up-Table
MSB..... Most Significant Bit
PAN..... Personal Area Network
PCI..... Peripheral Component Interconnect
PSK..... Phase Shift Keying
QAM..... Quadrature Amplitude Modulation
QPSK ..... Quadrature Phase Shift Keying
RAM..... Random Access Memory
RFID..... Radio Frequency Identification
ROM..... Read Only Memory
RTL..... Register Transfer Level
SNR..... Signal-to-Noise Ratio
SoC ..... System on Chip
SPIHT..... Set Partitioning In Hierarchical Trees
TDMA ..... Time Division Multiple Access
TBW..... Total Body Water
USB..... Universal Serial Bus
VLSI..... Very Large Scale Integration
WBS..... Wide Band Signaling
WLAN ..... Wireless Local Area Network
WT..... Wavelet Transform

Bibliography

[BB84] D.C. Barber and B.H. Brown, *Applied potiential tomography*, Journal of Physics E: Scientific Instruments **17** (1984), 723–733.

[Ber01] Berufsgenossenschaftliche Vorschrift für Sicherheit und Gesundheit bei der Arbeit (BGV B11 VBG 25), *Unfallverhütungsvorschrift*, 2001.

[Bro06] Joseph D. Bronzino, *The biomedical engineering handbook: Biomedical engineering fundamentals*, 3 ed., CRC Press Taylor & Fancis Group, LCC, 2006.

[Bun94] Schweizerischer Bundesrat, *Verordnung über elektrische Starkstromanlagen, Starkstromverordnung, SR-No.734.2*, 1994.

[C9506] IEEE C95.1-2005, *IEEE Standard for Safety Levels with Respect to Human Exposure to Radio Frequency Electromagnetic Fields, 3 kHz to 300 GHz*, The Institute of Electrical and Electronics Engineers Inc., New York (2006).

[CC41] Kenneth S. Cole and Robert H. Cole, *Dispersion and absorption in dielectrics, I. Alternating current characteristics*, J. Chem. Phys. (1941), 341–351.

[CP91] Arnon Cohen and Mladen Poluta, *Optimal qrs detection algorithms*, Proceedings 6th Mediterranean Electrotechnical Conference, vol. 1, 1991, pp. 782–785.

[DS98] Ingrid Daubechies and Wim Sweldens, *Factoring wavelet transforms into lifting steps*, J. Fourier Anal. Appl. **4** (1998), no. 3, 247–269.

[Ein03] W. Einthoven, *Die galvanometrische registrirung des menschlichen elektrokardiogramms, zugleich eine beurteilung der anwendung des capillar-elektrometers in der physiologie*, Pflugers Arch. ges. Physiol (1903), no. 99, 472.

[Eur96] European Committee for Electrotechnical Standardization, *Human Exposure to Electromagnetic Fields: High-Frequency (10 kHz to 300 GHz), Brussels, Belgium*, CENELEC ENV 50166-2 (1996).

[Eur99] European Council Recommendation, *Human Exposure to Electromagnetic Fields: High Frequency (0 Hz to 300 GHz), Brussels, Belgium*, 1999/519/EC (1999), 59–70.

[Fed85] Federal Communications Commission (FCC), *Guidelines for Human Exposure to Radiofrequency Radiation*, Federal Register 38653 **100** (1985), no. 543, 79–144.

[Fey02] G. Fey, *Set partitioning in hierarchical trees: A FPGA-implementation*, Master thesis (in german),, Martin-Luther-University Halle, Germany, 2002.

[FI04] Katsuyuki Fujii and Koichi Ito, *Evaluation of the received signal level in relation to the size and carrier frequency of the wearable device using human body as a transmission channel*, IEEE Antennas and Propagation Society International Symposium, vol. 1, 2004, pp. 105–108.

[FIT02] Katsuyaki Fujii, Koichi Ito, and Shigeru Tajima, *Signal propagation of wearable computing using human body as transmission channel*, Proceedings of the International Symposium on Antennas and Propagation ISAP-02, 2002, pp. 512–515.

[FIT03] Katsuyuki Fujii, Koichi Ito, and Shigeru Tajima, *A study on the receiving signal level in relation with the location of electrodes for wearable devices using human body as a transmission channel*, Proceedings of the International Symposium on Antennas and Propagation ISAP-03, 2003, pp. 1071–1074.

[FJY+90] G.M. Friesen, T.C. Jannett, M.A. Jadallah S.L. Yates, S.R. Quint, and H.T. Nagle, *A comparison of the noise sensitivity of nine qrs detection algorithms*, IEEE Transaction on Biomedical Engineering **37** (1990), 85–98.

[FS89] K.R. Foster and H.P. Schwan, *Dielectric properties of tissues and biological materials: A critical review*, Critical reviews in biomedical Engineering (1989), no. 1, 25–104.

[FS94] Masaaki Fukumoto and Yasuhito Suenaga, *Fingering: a full-time wearable interface*, CHI '94: Conference companion on Human factors in computing systems (New York, NY, USA), ACM Press, 1994, pp. 81–82.

[FSS03] Masaaki Fukomoto, Mitsuru Shinagawa, and Toshiaki Sugimura, *A broad-band intrabody communication system with electro-optic probe*, First International Conference on Appliance Design, 2003, pp. 108–109.

[FT97] Masaaki Fukumoto and Yoshinobu Tonomura, *Body coupled fingering: Wireless wearable keyboard*, CHI'97 (1997), 147–154.

[GLG96a] S. Gabriel, R. W. Lau, and C. Gabriel, *The dielectric properties of biological tissues: I. Literature survey*, Phys. Med. Bio. **41** (1996), no. 11, 2231–2249.

[GLG96b] S. Gabriel, R. W. Lau, and C. Gabriel, *The dielectric properties of biological tissues: II. Measurements in the frequency range 10 Hz to 20 GHz*, Phys. Med. Bio. **41** (1996), no. 11, 2251–2269.

[GLG96c] S. Gabriel, R. W. Lau, and C. Gabriel, *The dielectric properties of biological tissues: III. Parametric models for the dielectric spectrum of tissues*, Phys. Med. Bio. **41** (1996), no. 11, 2271–2293.

[Gra97] Matthew Gray, *Physical limits of intrabody signalling*, Bachelors thesis, MIT, 1997.

[HJ78] R.P. Henderson and J.G. Webster J.G., *An impedance camera for spatially specific measurements of the thorax*, IEEE Transaction on Biomedical Engineering **25** (1978), 250–254.

[HK06] Martin Hediger and Thomas Kaufmann, *Wireless implant communications*, Diploma thesis, IIS/ETH Zurich, 2006.

[HMS69] Earl C. Hoffer, Clifton K. Meador, and David C. Simpson, *Correlation of wholebody impedance with total body volume*, Journal of Applied Physiology **27** (1969), 531–534.

[HNT+03] K. Hachisuka, A. Nakata, T. Takeda, Y. Terauchi, K. Shiba, K. Sasaki, H. Hosaka, and K. Itao, *Development and performance analysis of an intra-body communication device*, 12th International Conference on Transducers, Solid-State Sensors, Actuators and Microsystems, vol. 2, 2003, pp. 1722–1725.

[HSI+97] Takashi Handa, Shuichi Shoji, Shinichi Ike, Sunao Takeda, and Tetsushi Sekiguchi, *A very low-power consumption wireless ECG monitoring system using body as a signal transmission medium*, Proceedings of the International Conference on Transducers, Solid-State Sensors and Actuators, 1997, pp. 1003–1007.

[HTK+05] Keisuke Hachisuka, Yusuke Terauchi, Yoshinori Kishi, Terunao Hirota, Ken Sasaki, Hiroshi Hosaka, and Koichi Ito, *Simplified circuit modeling and fabrication of intrabody communication devices*, 13th International Conference on Solid-State Sensors, Actuators and Microsystems, vol. 2E4-3, 2005, pp. 461–464.

[HTT+05] Keisuke Hachisuka, Teruhito Takeda, Yusuke Terauchi, Ken Sasaki, Hiroshi Hosaka1, and Kiyoshi Itao, *Intra-body data transmission for the personal area network*, Microsystem Technologies, Springer Berlin / Heidelberg **11** (2005), 1020–1027.

[IHP01] Robert S. H. Istepanian, Leontios J. Hadjileontiadis, and Stavros M. Panas, *Ecg data compression using wavelets and higher order statistics methods*, IEEE Transaction on Biomedical Engineering **5** (2001), no. 2, 108–115.

[Int94] International Standard ISO/IEC 7498-1 , *Information technology - Open Systems Interconnection - Basic Reference Model: The Basic Model*, 1994, p. 68.

[Int97] International Commission on Non-Ionizing Radiation Protection (ICNIRP), *Guidelines for limiting exposure to time-varying electric, magnetic, and electromagnetic fields (up to 300GHz)*, 1997, pp. 513–514.

[Int03] International Commission on Non-Ionizing Radiation Protection (ICNIRP), *Guidance on determining compliance of exposure to pulsed fields and complex non-sinusoidal waveforms below 100 khz with icnirp guidelines*, 2003, pp. 383–387.

[KK05] Andreas Kuhn and Thierry Keller, *A 3d transient model for transcutaneous functional electrical stimulation*, International Functional Electrical Stimulation Society Conference, Montreal, Canada,, vol. 10, 2005, pp. 385–387.

[KK06] A. Kuhn and T. Keller, *The influence of capacitive properties on nerve activation in transcutaneous electrical stimulation*, International Symposium on Computer Methods in Biomechanics and Biomedical Engineering (Antibes, France), vol. 7, 2006.

[KML01] N. Kerrouche, C.N. McLeod, and W.R.B. Lionheart, *Time series of eit chest images using singular value decomposition and fourier transform*, Physiol. Meas. **22** (2001), no. 1, 147–157.

[Kyl04] Ursula G. Kyle, *Bioelectrical impedance analysis part i: review of principles and methods*, Clinical Nutrition (2004), no. 23, 1226–1243.

[LH04] Adrian Lehner and M. Hess, *Sicherheit und effizenz der digitalen datenübermittlung über den menschlichen körper mittels der ultracom-technologie*, Studienprotokoll, Kardiologie, Schweizer herz- und Gefässzentrum Bern, Universitätsklinik (Inselspital), 2004.

[LKP00] Z. Lu, D.Y. Kim, and W.A. Pearlman, *Wavelet compression of ECG signals by the set partitioning in hierarchical trees algorithm*, IEEE Transactions on Biomedical Engineering **47** (2000), no. 7, 849–856.

[LMHH98] Derek P. Lindsey, Eric L. McKee, Maury L. Hull, and Stephen M. Howell, *A new technique for transmission of signals from implantable transducers*, IEEE Transactions on Biomedical Enginierung **45** (1998), no. 5, 614–619.

[LOW+03] Byung Il Lee, Suk Hoon Oh, Eung Je Woo, Soo Yeol Lee, Min Hyoung Cho, Ohin Kwon, June-Yub Lee Jin Keun Seo, and Woon Sik Baek, *Three-dimensional forward solver and its performance analysis for magnetic resonance electrical impedance tomography (mreit) using recessed electrodes*, Phys. Med. Biol. **48** (2003), 1971–1986.

[LT06] Huaming Li and Jindong Tan, *Body sensor network based context aware qrs detection*, 28th Annual International Conference of the IEEE Engineering in Medicine and Biology Society (EMBC06), New York, USA, 2006, pp. 3266–3269.

[NRP04] National Radiological Protection Board NRPB, *Advice on limiting exposure to electromagnetic fields (0- 300GHz)*, Report of an independent Advisory Group on Non-ionising Radiation, vol. 15, 2004, pp. 1–36.

[Nyb70] J. Nyboer, *Electrical impedance plethysmograph*, 2 ed., Springfield, IL: CC Thomas, 1970.

[Obe02] Michael Oberle, *Low power system-on-chip for biomedical application*, PhD Thesis Diss. ETH No. 14509, IIS/ETH Zurich, 2002.

[Oet79] J.D. Oetting, *A comparison for digital radio*, IEEE Transactions on Communications **27** (December 1979), no. 12, 1752–62.

[PA02] ARPNSA (Australian Radiation Protection and Nuclear Safety Agency), *Maximum exposure levels to radiofrequency fields 3 kHz to 300 GHz*, 2002.

[PDV+01] Kurt Partridge, Bradley Dahlquist, Alireza Veiseh, Annie Cain, Ann Foreman, Joseph Goldberg, and Gaetano Borriello, *Empirical measurements of intrabody communication performance under varied physical configurations*, ACM UIST (2001), 183–190.

[PH67] R. Plonsey and D. B. Heppner, *Considerations of quasi-stationarity in electrophysiological systems*, Bull Math Biophys **29** (1967), no. 4, 657–64.

[PL02] N. Polydorides and W. R. B. Lionheart, *A matlab toolkit for three-dimensional electrical impedance tomography: a contribution to the electrical impedance and diffuse optical reconstruction software project*, Measurement Science & Technology **13** (2002), no. 12, 1871–1883.

[Plu06] Jack W. Plunbett, *Plunkett's health care industry almanac 2007: Health care industry market research, statistics, trends & leading companies*, Plunkett Research, Ltd, 2006.

[PRG+97] E.R. Post, M. Reynolds, M. Gray, J. Paradiso, and N. Gershenfeld, *Intrabody buses for data and power*, First International Symposium on Wearable Computers, 1997, pp. 52 – 55.

[PSAM05] M. Paksuniemi, H. Sorvoja, A. Alasaarela, and R. Myllyla, *Wireless sensor and data transmission needs and technologies for patient monitoring in the opreating room and intensive care unit*, EMBC, Shanghai, China, 2005, pp. 5182–5185.

[Rei98] J. P. Reilly, *Applied bioelectricity: From electrical stimulation to electropathology*, 2nd ed., Springer-Verlag New York Inc., 1998.

[RFM02] Joerg Ritter, Goerschwin Fey, and Paul Molitor, *SPIHT implemented in a XC4000 device*, MWSCAS, vol. 1, 2002, pp. 239–242.

[RMN05] I.M. Rezazadeh, M.H. Moradi, and A.M. Nasrabadi, *Implementation of SPIHT and sub-band energy compression (SEC) method on two-dimensional ECG compression: A novel approach*, IEEE EMBC, Shanghai, China, 2005, pp. 3763–3766.

[RSN97] Antti Ruha, Sami Sallinen, and Seppo Nissila, *A real-time microprocessor qrs detector system with a 1-ms timing accuracy for the measurement of ambulatory hrv*, IEEE Transactions on Biomedical Engineering **44** (1997), 159–167.

[SBN+01] G. J. Saulnier, R. S. Blue, J. C. Newell, D. Isaacson, and P.M. Edic, *Electrical impedance tomography*, IEEE Signal Processing Magazine **18** (2001), no. 6, 31–43.

[Sch57] H.P. Schwan, *Electrical properties of tissue and cell suspensions*, Advances in Biological and Medical Physics (1957), 147–209.

[Sch00] Schweizerisches Bundesamt für Umwelt, Wald und Landwirtschaft BUWAL, *NISV Verordnung über den Schutz vor nichtionisierender Strahlung, SR-No. 814.710*, 2000.

[SFOK04] M. Shinagawa, M. Fukumoto, K. Ochiai, and H. Kyuragi, *A near-field-sensing transceiver for intrabody communication based on the electrooptic effect*, IEEE Transaction on Instrumentation and Measurement **53** (2004), 1533–1538.

[SGS95] A. V. Shahidi, R. Guardo, and P. Savard, *Impedance tomography - computational analysis based on finite-element models of a cylinder and a human thorax*, Annals Of Biomedical Engineering **23** (1995), no. 1, 61–69.

[Sha48] C. E. Shannon, *A mathematical theory of communication*, The Bell System Technical Journal **27** (July, October 1948), 379–423, 623–656.

[Sha93] J. M. Shapiro, *Embedded image coding using zerotrees of wavelet coefficients*, IEEE Transactions on Signal Processing **41** (1993), 3445 – 3462.

[Sha06] Ershad Sharifahmadian, *Wavelet compression of multichannel ecg data by enhanced set partitioning in hierarchical trees algorithm*, 28th Annual International Conference of the IEEE Engineering in Medicine and Biology Society (EMBC06), New York, USA, 2006, pp. 5238–5241.

[SHC05] Hohamad Sawan, Yamu Hu, and Jonathan Coulombe, *Wireless smart implants dedicated to multichannel monitoring and microstimulation*, IEEE Circuits and systems magazine (2005), 21–39.

[SMW+04] J.H. Schulman, J.P. Mobley, J. Wolfe, E. Regev, C.Y. Perron, R. Ananth, E. Matei, A. Glukhovsky, and R. Davis, *Battery powered BION FES network*, Proceedings of the 26th Annual International Conference of the IEEE Engineering in Medicine and Biology Society, 2004, pp. 4283–4286.

[SMW+06] Joseph H. Schulman, J.Phil Mobley, Jmaes Wolfe, Howard Stover, and Adrian Krag, *A 1000+ channel bionic communication system*, 28th Annual International Conference of the IEEE Engineering in Medicine and Biology Society (EMBC06), New York, USA, September 2006, pp. 4333–4335.

[SP96] A. Said and W.A. Pearlman, *A new, fast, and efficient image codec based on set partitioning in hierarchical trees*, IEEE Transaction on Circuits and Systems for Video Technology **6** (1996), no. 3, 243–250.

[Tho62] A. Thomasset, *Bio-electrical properties of tissue impedance measurements*, Lyon Med **207** (1962), 107–118.

[Tho63] A. Thomasset, *Bio-electrical properties of tissues*, Lyon Med **209** (1963), 1325–1352.

[TSY05] S. Tai, C. Sun, and W. Yan, *A 2-D ECG compression method based on wavelet transform and modified SPIHT*, IEEE Transaction on Biomedical Engineering **52** (2005), no. 6, 999–1008.

[TU] TU Delft, Section Applied Ergonomics and Design, DINED data set, *http://www.dined.nl*.

[Wal89] A.D. Waller, *One the electromotive changes connected with the beat of the mammalian heart, and the human heart in particular*, Phil. Trans. **B** (1889), no. 180, 169.

[WFOK06] Marc S. Wegmueller, Wolfgang Fichtner, Michael Oberle, and Niels Kuster, *BPSK & QPSK modulated data communication for biomedical monitoring sensor network*, IEEE EMBC, New York, USA, 2006, pp. 2071–2074.

[WHK+07] Marc S. Wegmueller, Martin Hediger, Thomas Kaufmann, Michael Oberle, Niels Kuster, and Wolfgang Fichtner, *Investigation on coupling strategies for wireless implant communication*, IEEE IMTC, Warsaw, Poland, 2007.

[WLF+05a] Marc Wegmueller, Adrian Lehner, Juerg Froehlich, Michale Oberle, Norbert Felber, Niels Kuster, Otto Hess, and Wolfgang Fichtner, *Characterization of the human body as a communication channel at low frequency*, 14th International Conference of Medical Physics (ICMP), Nuremberg, Germany, vol. 1, 2005, pp. 304–305.

[WLF+05b] Marc Wegmueller, Adrian Lehner, Juerg Froehlich, Robert Reutemann, Michale Oberle, Norbert Felber, Niels Kuster, Otto Hess, and Wolfgang Fichtner, *Measurement system for the characterization of the human body as a communication channel at low frequency*, IEEE EMBC, Shanghai, China, 2005, pp. 3502–3505.

[WOF+06a] Marc S. Wegmueller, Michael Oberle, Norbert Felber, Niels Kuster, and Wolfgang Fichtner, *Galvanical coupling for data transmission through the human body*, IEEE IMTC, Sorrento, Italy, 2006, pp. 1686–1689.

[WOF+06b] Marc S. Wegmueller, Michael Oberle, Norbert Felber, Niels Kuster, and Wolfgang Fichtner, *Galvanical coupling for data transmission through the human body*, IEEE Instrumentation and Measurement Technology Conference IMTC 2006, Sorrento, Italy, 2006, pp. 1686–1689.

[WOKF06] Marc S. Wegmueller, Michael Oberle, Niels Kuster, and Wolfgang Fichtner, *From dielectrical properties of human tissue to intra-body communications*, WC 2006, Seoul, Korea, 2006, pp. 513–517.

[WPB+06] Marc Simon Wegmueller, David Perels, Tobias Blaser, Stephan Senn, Philipp Stadelmann, Norbert Felber, and Wolfgang Fichtner, *Silicon implementation of the spiht algorithm for compression of ecg records*, 49th IEEE Midwest Symposium on Circuits and Systems (MWSCAS), 2006.

[YLSS06] Ning Yao, Heung-No Lee, R.J. Sclabassi, and Mingui Sun, *Low power digital communication in implantable devices using volume conduction of biological tissues*, IEEE EMBC'06, New York, USA, 2006, pp. 6249–6252.

[Zim80] Hubert Zimmerman, *OSI Reference Model: The ISO Model of Architecture for Open Systems Interconnection*, IEEE Transactions on Communications **28** (1980), no. 4, 425 – 432.

[Zim95] Thomas Gurthrie Zimmerman, *Personal area network (PAN)*, Master thesis, Massachusetts Institute of Technology, 1995.

[Zim96] Thomas G. Zimmerman, *Personal area networks: Near-field intrabody communication*, IBM System Journal **35** (1996), no. 3+4, 609–617.

[ZSP+95] Thomas G. Zimmerman, Joshua R. Smith, Joseph A. Paradiso, David Allport, and Neil Gershenfeld, *Applying electric field sensing to human-computer interfaces*, Proceedings of the SIGCHI conference on Human factors in computing systems, Denver, Colorado, United States, 1995, pp. 280–287.

List of Publications

1. Andreas Burg, Markus Wenk, Martin Zellweger, Marc Wegmueller, Norbert Felber, and Wolfgang Fichtner, *"VLSI Implementation of the Sphere Decoder Algorithm"*, 30th European Solid-State Circuits Conference (ESSCIRC 2004), Leuven, Belgium, Sept. 2004.

2. Marc Wegmueller, Adrian Lehner, Juerg Froehlich, Robert Reutemann, Michael Oberle, Norbert Felber, Niels Kuster, Otto Hess, and Wolfgang Fichtner, *"Measurement System for the Characterization of the Human Body as a Communication Channel at Low Frequency"*, 27th Annual International Conference of the IEEE Engineering in Medicine and Biology Society (EMBC 2005), Shanghai, China, Sept. 1-4, 2005.

3. Marc Wegmueller, Adrian Lehner, Juerg Froehlich, Michael Oberle, Norbert Felber, Niels Kuster, Otto Hess, and Wolfgang Fichtner, *"Characterization of the Human Body as a Communication Channel at Low Frequency"*, 14th International Conference of Medical Physics (ICMP 2005), Nuremberg, Germany, Sept. 14-17, 2005.

4. Marc Simon Wegmueller, Michael Oberle, Norbert Felber, Niels Kuster, and Wolfgang Fichtner, *"Galvanical Coupling for Data Transmission through the Human Body"*, IEEE Instrumentation and Measurement Technology Conference (IMTC 2006), Sorrento, Italy, April 24-27, 2006.

5. Marc Simon Wegmueller, David Perels, Tobias Blaser, Stephan Senn, Philipp Stadelmann, Norbert Felber, and Wolfgang Fichtner, *"Silicon Implementation of the SPIHT Algorithm for Compression of ECG*

Records", 49th IEEE Midwest Symposium on Circuits and Systems (MWSCAS 2006), Puerto Rico, Aug. 6-9 2006.

6. Marc Wegmueller, Michael Oberle, Norbert Felber, Niels Kuster, and Wolfgang Fichtner, *"From Dielectrical Properties of Human Tissue to Intra-Body Communications"*, World Congress on Medical Physics and Biomedical Engineering (WC 2006), Seoul, Korea, Aug. 27 - Sept. 1, 2006.

7. Marc Wegmueller, Michael Oberle, Norbert Felber, Niels Kuster, and Wolfgang Fichtner, *"Digital Data Communication through the Human Body for Biomedical Monitoring Sensor Network"*, World Congress on Medical Physics and Biomedical Engineering (WC 2006), Seoul, Korea, Aug. 27 - Sept. 1, 2006.

8. Marc Simon Wegmueller, Wolfgang Fichtner, Michael Oberle, and Niels Kuster, *"BPSK & QPSK Modulated Data Communication for Biomedical Monitoring Sensor Network"*, 28th Annual International Conference of the IEEE Engineering in Medicine and Biology Society (EMBC06), New York City, USA, Aug. 30 - Sept. 3, 2006.

9. Marc Simon Wegmueller, Martin Hediger, Thomas Kaufmann, Michael Oberle, Niels Kuster, and Wolfgang Fichtner, *"Investigation on Coupling Strategies for Wireless Implant Communications"*, IEEE Instrumentation and Measurement Technology Conference (IMTC 2007), Warsaw, Poland, May 1-3, 2007.

10. Marc Simon Wegmueller, Martin Hediger, Thomas Kaufmann, Felix Buergin, and Wolfgang Fichtner, *"Wireless Implant Communications for Biomedical Monitoring Sensor Network"*, IEEE International Symposium on Circuits and Systems (ISCAS 2007), New Orleans, USA, May 27-30, 2007.

11. Marc Simon Wegmueller, Michael Oberle, Norbert Felber, Niels Kuster, and Wolfgang Fichtner, *"Signal Transmission by Galvanic Coupling Through the Human Body"*, IEEE Transaction on Instrumentation and Measurement TIM (submitted June 2006, to appear 2008).

12. Marc Simon Wegmueller, Andreas Kuhn, Juerg Froehlich, Michael Oberle, Norbert Felber, Niels Kuster, and Wolfgang Fichtner, *"An Attempt to Model the Human Body as a Communication Channel"*, IEEE Transaction on Biomedical Engineering T-BME (submitted July 2006, to appear 2007).

13. Marc Simon Wegmueller, Sonja Huclova, Juerg Froehlich, Michael Oberle, Norbert Felber, Niels Kuster, and Wolfgang Fichtner, *"Galvanic Coupling Enabling Wireless Implant Communications"*, IEEE Transaction on Instrumentation and Measurement TIM (submitted June 2007).

14. Marc Simon Wegmueller and Wolfgang Fichtner, *"Implantable Biomedical Sensor Network with Capacitive Coupling Communications"*, IEEE Transaction on Biomedical Circuits and Systems TBioCAS (submitted 2007).

Curriculum Vitae

Marc Simon Wegmueller was born in Bern, Switzerland, in 1977. He received his Diploma degree in Electrical Engineering from the Swiss Federal Institute of Technology Zurich (ETH), Zurich, Switzerland, in 2002.

After working in the field of vital monitoring systems and ASIC integration at Miromico AG, Zurich, he joined the Integrated Systems Laboratory (IIS) at ETH Zurich as a research and teaching assistant in 2003. He was also employed by the Foundation for Research on Information Technologies in Society (IT'IS) as research assistant in the Health Supporting Systems group.

His research interests include the design of VLSI circuits and systems and digital signal processing for medical applications.